# DEVELOPMENT OF FAR-INFRARED POLARI-INTERFEROMETER FOR THE EVALUATION OF CURRENT DENSITY PROFILES AND CONFINEMENT PROPERTIES ON THE JT-60 TOKAMAK

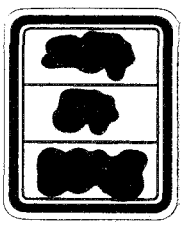

Takeshi Fukuda

# DEVELOPMENT OF FAR-INFRARED POLARI-INTERFEROMETER FOR THE EVALUATION OF CURRENT DENSITY PROFILES AND CONFINEMENT PROPERTIES ON THE JT-60 TOKAMAK

# (JT-60トカマクの電流分布と閉じ込め特性評価のための遠赤外偏光干渉計の開発)

June 1989

Takeshi Fukuda

Department of Large Tokamak Research

Japan Atomic Energy Research Institute

平成元年6月

日本原子力研究所　臨界プラズマ研究部

福田　武司

# TABLE OF CONTENTS

# CHAPTER 1. INTRODUCTION

After the intensive experimental physics research in the 1960s, outstanding performance in plasma confinement was elicited from the tokamak configuration,[1-1,2] and the major portion of the fusion research effort was devoted to the tokamak approach in the years which followed. Although extended progress has been made in untangling the physics of the tokamak discharge during the intervening decade,[1-3] the remaining parameter gap relative to the nominal goal of n (plasma density) $\cdot \tau_E$ (energy confinement time) = $10^{20}$ sec $\cdot$ $m^{-3}$ at T (plasma temperature) = 10 keV (Lawson's criteria)[1-4] was still substantial. Accordingly, recent thermonuclear fusion research is focused on the enlargement of the plasma volume, as represented by three large tokamak devices : JT-60 (Japan), JET (EC nations), and TFTR (USA), for the improvement of energy confinement time following empirical scalings, although the physical understanding of the tokamak confinement is still incomplete.

For the analysis of plasma properties in a tokamak plasma, such as the energy confinement time and particle transport, interferometric measurements have been recognized as an indispensable means of plasma diagnostics. Based upon the principle that the amount of phase shift which a traversing wave experiences inside a plasma is proportional to the electron density, the initial interferometric measurement was pursued with microwaves[1-5] and visible laser beams[1-6] in 1950s. Owing to the advent of far-infrared (FIR) lasers in 1970,[1-7] interferometric plasma diagnostics has made substantial progress, synchronized with the advance of the tokamak plasma performance, by successfully adopting FIR lasers as a scene beam for high density plasma applications.[1-8] In comparison with microwaves, the FIR wavelength mitigates the refractive effect and dissipation of the beam power due to the expanded beam diameter. It also yields a larger

phase shift and reduced sensitivity to the mechanical vibrations than visible or near-infrared wavelengths.[1-9]

Although several endeavors, such as the development of the heterodyne detection technique with a twin laser system, have also been made for the improvement of fringe resolution during the mid-1970s,[1-10] conventional interferometers reveal their intrinsic difficulties in interpreting the phase shift data with adequate resolution for the large tokamak application, which was subtle enough when applied on the medium-sized fusion experiment devices. Therefore, additional developments have to be pursued for JT-60 applications. The process of fusion research thereby proclaims that interferometers must follow the progress of plasma parameters.

This thesis work is, as a primary objective, focused on the development of a multi-wavelength (118.8-μm, 2-mm, and 0.63-μm) polari-interferometer system feasible enough for JT-60 diagnostics. Imposed requirements which conventional FIR interferometers envisage on the large tokamak applications are mainly attributed to the long distance propagation of laser beams, and namely they are :

(1) Development of a single-mode and frequency-stabilized FIR laser.

Since the difference of the optical path length between the probing and reference branch is 40 m and the total propagation distance exceeds 130 m for JT-60, high frequency stability and mode purity are essential to obtain an adequate fringe resolution. Otherwise, deterioration of fringe resolution and visibility due to the distortion of wave front as well as the loss of intensity can easily be caused. Anticipating the application of developed frequency stabilization scheme, as well as concerning the scene wavelength limitations on the polarimetric measurement and the concave lens effect, $CO_2$ laser pumped 118.8-μm methyl-alcohol laser has been chosen as an interferometer light source.

(2) Evaluation of an effective beam diameter to cope with the phase distortion effect of propagating wave front.

Since the propagating distance of the probing laser beam inside a plasma (JT-60 plasma radius $r$ = 0.93 m) is large, propagating beam diameter naturally becomes large Since the propagating distance of the probing laser beam inside a plasma is large, propagating beam diameter naturally becomes large (typically 56 mm$\phi$ for the JT-60 interferometer), and a plasma is not homogeneous over the beam diameter. When the local phase varies across the diameter of probing beam, the detector will sense an average phase shift, which implies that a significant error can possibly be introduced. Accordingly this effect sets limit to the beam diameter for a given value of the local density gradient.

(3) Development of stable and low-loss long distance propagation technique.

On another matter, mutual displacements between the FIR lasers and main structure of the interferometer produce severe deflection of the propagating beam axis, since they are inevitably placed far apart. In order to minimize the deflection, which leads to the deterioration of visibility and the fluctuation of the beam intensity at detectors, development of stable long distance propagation technique is necessary. As to the low-loss long distance transmission, attenuation index of the propagating laser beam in a humid air must be precisely evaluated for the effective dehydrating design, since the existence of vapor in the propagation volume disturbs the optimum transmission, and it literally limits the S/N ratio.

(4) Development of optical components for the effective beam power distribution including polarization components.

In addition, the large beam diameter requires the development of effective beam-splitting and polarizing

materials for the 118.8-μm radiation, since mylar films and free-standing wire grids suffer from micro-phonic effect, diffraction effect, and mechanical vibrations induced by the huge stray magnetic field penetrating through all the optical components.

(5) Improvement of the diagnostic accessibility.

Another aspect of limitation pertinent to the large tokamak application is its restricted diagnostic accessibility to obtain informations over the full plasma volume. For the improvement of diagnostic accessibility, which is sacrificed by the complexed poloidal field configuration and large structures around the torus, application of the millimeter wave circuitry is prospective. Its transmission characteristics, in principle, enables a flexible design according to the arrangement of diagnostic chords, although the transmission efficiency concerning the ohmic loss and the mode conversion loss must be precisely examined beforehand.

(6) Extension to a maintenance free and remote controlled system.

Furthermore, the interferometer system is supposed to function reliably without any maintenance complications for a long period, under the supervise of a programed communication network with a host computer system, since the residual levels of radioactivity in the vicinity of the tokamak will preclude all the maintenance personnel.

Intensive researches concerning above requirements have been pursued, aiming the establishment of a design basis of the large tokamak interferometer design.

Another objective of this thesis work is to establish a proper *physics interpretation schemes* incident to the interferometric measurement and to demonstrate the concept of*"active diagnostics"*. Interferometric plasma

diagnostics so far applied was merely to inform of plasma parameters of a discharge, being neither the active instrument of understanding physics nor controlling plasma parameters.

(i) One of the approaches is real-time feedback control of electron density, which is presumably effective for the stable plasma current rise[1-11] and additional heating of ohmic plasmas. Another approach is the evaluation of transport parameters by elucidating the mutual correlation among a divertor plasma, scrape-off layer plasma, and bulk plasma properties.

(ii) In order to understand the divertor mechanism, high density and small volume plasma interferometry in the divertor region was first undertaken with the developed FIR interferometer system. Thereby, precious informations on the physics of density clamping (a phenomenon which neutral beam heated plasma density decreases due to the apparent degradation of the particle confinement time) hitherto unknown have been obtained.

(iii) Inversion of measured line electron density data to the profile information is also an important item of the physics interpretation. Due to the insufficient diagnostic accessibility, conventional Abel inversion method is not applicable to reproduce the profile informations with adequate resolution. Therefore, the development of a magneto-hydrodynamic (MHD) equilibrium calculation code has been pursued to understand the temporal evolution of the electron density profile.

(iv) Further extension of the interferometric technique to the evaluation of current density profiles (or equivalently the poloidal magnetic field distribution) in a tokamak plasma by the Faraday rotation angle measurement[1-12] can potentially elucidate ubiquitous MHD activities and confinement mechanism. From the outset of the 1970s, various methods have been proposed[1-13,14,15] for

diagnosing or deducing the current density distribution, which are of basic and primary interest in a tokamak plasma research. A precise knowledge of the current density distribution is required to understand the energy deposition profile and transport mechanism as well as to clarify the functional relationship of the current density distribution to the electron temperature profile.

Nevertheless, over a decade, the current density distribution has not been adequately diagnosed, suffering from the resolution and persisting experimental restrictions for the physics interpretation. Therefore, thus far, the degree to which an alteration in the current density profile shape is instrumental in effecting the confinement properties and MHD modes has only been indirectly inferred from the magnetic probe measurement and x-ray emission profiles. On another matter, it has been recently demonstrated that MHD modes can be influenced by use of non-inductive lower hybrid current drive.[1-16,17] Against the potential importance of the active profile control for the improvement of confinement properties, neither the possibility of profile control itself nor the relationship between the profile shape and energy confinement time has not been yet experimentally investigated.

Although an application of Faraday rotation angle measurements on a plasma was undertaken in 1960s,[1-18] the first detection of the poloidal magnetic field in a tokamak plasma was contrived by Kunz after a decade in 1978.[1-19] Stimulated by this experiment, several developments for the improvement of resolution such as the polarization modulation technique[1-20,21] have been intensively pursued in the subsequent years. Substantial efforts to obtain an adequate resolution as well as to develop an evaluation procedure for the physics interpretation of the rotation angle have been made,[1-22] though without any significant result as to the confinement properties of a plasma. Polarimetric method is still one of the most prospective method of diagnosing current density profiles, compared to other approaches such as the laser scattering technique[1-23] and neutral-lithium-beam probe

measurements,[1-24] since it provides continuous data throughout the entire plasma discharge, and it is effective for a wide range of plasma parameters.

The temporal evolution of the current density profile and confinement properties of JT-60 plasmas heated in various methods have been investigated in this work, in order to evaluate the effectiveness of the additional plasma heating methods. A MHD equilibrium calculation code which transforms the rotation angle to the local poloidal magnetic field has been devised. Based upon the compiled results, the possibility of actively modifying the current density distribution in a large tokamak, and the effective method of improving confinement properties by an active profile control have been also surveyed via polarimetry for the first time, introducing an alternative approach to the physics interpretation of the Faraday rotation measurements. The effective modification of the current density distribution with lower hybrid waves has been successfully achieved on JT-60 to proclaim that the flattening of the current density profile, accompanied by the peaked electron temperature profile, can contribute to the improvement of energy confinement time.

In chapter 2, details on the development and performances of the FIR laser are described, and the result of developments on the JT-60 polari-interferometer system is stated in chapter 3. The result of measurements and their physics interpretation of the first interferometric divertor and edge plasma density measurement are described in chapter 4. The temporal behavior of the current density profile for the evaluation of confinement properties by the Faraday rotation angle measurement is discussed in chapter 5. In chapter 6, parameter dependence of the active modification of the current density profile is described to claim the optimum profile modification scheme for the improvement of confinement properties. The whole discussion is concluded in the final chapter 7.

## REFERENCES TO CHAPTER 1


1-1 R. S. Pease, Proc. Phys. Soc. **70B**, 11(1957).

1-2 R. Post, J. Nucl. Energy, Part C (Plasma Physics) **3**, 73(1961).

1-3 H. P. Furth, The Tokamak, Fusion (Academic Press, New York, 1981), Vol. 1, Part A, p. 123.

1-4 J. Wesson, Tokamaks (Oxford University Press, Oxford,1987).

1-5 R. F. Whitmer, Phys. Rev. **104**,572(1956).

1-6 R. A. Alpher and D. R. White, Phys. Fluids **2**,162(1959).

1-7 T. Y. Chang and T. J. Bridges, Opt. Commun. **1**, 423(1970).

1-8 D. Véron, Opt. Commun. **10**, 95(1974).

1-9 A. A. Dougal, Phys. Rev. Lett. **13**, 156(1964).

1-10 S. M. Wolfe, K. J. Button, J. Waldman, and D. R. Cohn, Appl. Opt. **15**, 2645(1976).

1-11 R. Yoshino et al. , JAERI-M 88-111(1988).

1-12 M. A. Heald and C. B. Wharton, Plasma Diagnostics with Microwaves, John Wiley & Sons, 1965.

1-13 J. Fujita and K. McCormick, Controlled Fusion and Plasma Physics (Proc. 6 th EPS Conf. Moscow, 1973), Vol. 1, p. 191.

1-14 J. Sheffield, Plasma Scattering of Electromagnetic radiation, Academic Press, New York, 1975.

1-15 S. Von Goeller, W. Stodiek, N. Sauthoff, Phys. Rev. Lett. **33**, 1201(1974).

1-16 D. van Houtte et al., Nucl. Fusion Lett. **24**,1485(1984).

1-17 F. X. Söldner et al., Proceedings of the 13 th European Conference on Controlled Fusion and Plasma Physics, Schliersee, 1986, edited by G. Briffod and M. Kaufmann (European Physical Society, Petit-Lancey, Switzerland, 1986), Vol. 2, p. 319.

1-18 I. S. Falconer and S. A. Ramsden, J. Appl. Phys. **39**, 3449(1968).
1-19 W. Kunz, Nucl. Fusion **18**, 1729(1978).
1-20 D. P. Huchinson et al. , Nucl. Fusion **21**,1535(1981).
1-21 T. Fukuda, S. Goto, T. Ishimura, and H. Ito, International Journal of Infrared and Millimeter Waves **5**, 1039(1984).
1-22 H. Soltwisch, W. Stodiek, J. Manickam, J. Schlüter, Plasma Physics and Controlled Nuclear Fusion Research (Proc. 11 th IAEA Conf. Kyoto, 1986), Vol. 1, International Atomic Energy Agency, 263(1987).
1-23 M. J. Forrest, P. G. Carolan, N. J. Peacock, Nature **271**, 718(1978).
1-24 K. McCormick, F. X. Söldner, D. Eckhartt et al., Phys. Rev. Lett. **58**, 491(1987).

# CHAPTER 2. FREQUENCY-STABILIZED CW 118.8-μm $CH_3OH$ WAVEGUIDE LASER FOR LARGE TOKAMAK DIAGNOSTICS

A frequency-stabilized single-mode cw 118.8-μm $CH_3OH$ waveguide laser was newly developed for polari-interferometry on the JT-60 tokamak. Interferometric plasma diagnostics on large fusion devices requires a mode purity of a source laser for the long-distance propagation and frequency stability to obtain an adequate feinge resolution. The accomplished performances are: $\Delta f/f < 1 \times 10^{-8}$, power stability < 0.03 %, and single $EH_{11}$ mode to yield a Gaussian-shaped profile in the far-field. Homogeneous pumping of laser media with a Ge étalon beam coupler and feedback stability control are the keys to the source far-infrared laser performances required for large tokamak diagnostics. The developed laser was totally adjustment free for more than two weeks and reliably in operation for two years on the JT-60 tokamak.

## 2. 1. INTRODUCTION

Owing to the advent of far-infrared (FIR) lasers in 1970,[1-7] interferometric plasma diagnostics has made substantial progress in high density plasma applications. Heterodyne detection of the induced phase shift with twin-laser phase-modulation technique[2-1] has been subsequently developed to obtain reliable electron density data on several medium-sized tokamaks. For an application to large fusion experiment devices, however, high frequency stability and mode purity of the source laser are additionally required in order to obtain an adequate fringe resolution, since the difference of the optical path length between the reference and probing branch becomes inevitably large and the total propagation distance also becomes large. These factors can easily cause the deterioration of fringe resolution and visibility due to the distortion of the wave front besides the

loss of intensity. In the case of the JT-60 interferometer, the total propagation distance exceeds 130 m and the difference between the reference and probing branch is 40 m. The long propagation distance and the large path length difference are due to the interferometer design requirement that the source laser must be installed outside of the torus hall, where the JT-60 tokamak is situated, to avoid the effect of mechanical vibration and stray magnetic field as well as to eliminate large interferometer structures above the floor level for reliability and compactness. The requirement imposed on FIR lasers for the high-resolution and totally adjustment-free JT-60 interferometer are (1) the frequency and power stability control and (2) mode purity, that is, the suppression of the self-beat spectra due to the optical feedback of pump $CO_2$ laser beam or the multimode oscillation of FIR lasers. The achieved performances of the newly developed cw118.8-$\mu$m $CH_3OH$ waveguide laser, which employs Ge étalons as beam couplers and the cavity length modulation technique, are described in this chapter in relation to the imposed requirements mentioned above.

As for the frequency stability required, supposing the electric field at laser output windows in the following form:

$$e_p = A_p \sin[\omega_p t+\phi_p(t)] \tag{2.1}$$

$$e_R = A_R \sin[\omega_R t+\phi_R(t)] , \tag{2.2}$$

the detected electric field for the probing beat signal can be written as

$$e_{p1} = A_p \sin[\omega_p(t- \frac{l_1}{c}) + \phi_p(t- \frac{l_1}{c}) + \phi(n_e)] \tag{2.3}$$

$$e_{R1} = A_R \sin[\omega_R(t- \frac{l_2}{c}) + \phi_R(t- \frac{l_2}{c})] , \tag{2.4}$$

and for the reference beat signal

$$e_{p2} = A_p \sin[\omega_p(t- \frac{l_3}{c}) + \phi_p(t- \frac{l_3}{c})] \tag{2.5}$$

$$e_{R2} = A_R \sin[\omega_R(t- \frac{l_4}{c}) + \phi_R(t- \frac{l_4}{c})] . \tag{2.6}$$

Here, $\omega_p$ and $\omega_R$ are the angular frequency of twin lasers, and they are supposed to be constant to exclude the

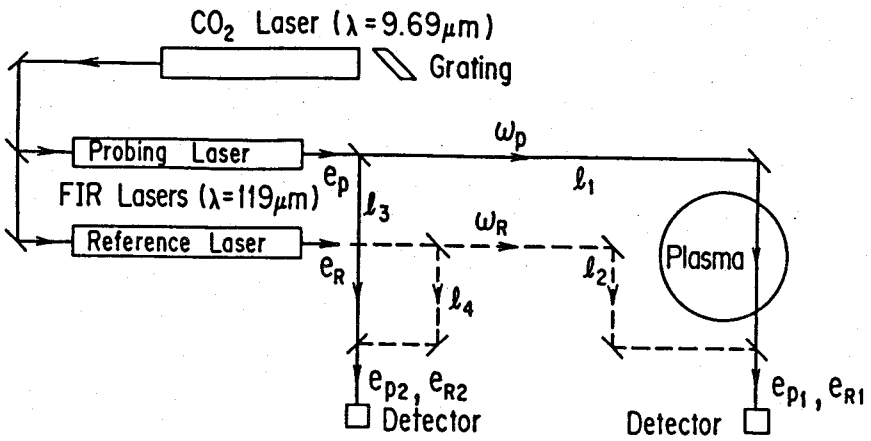


Fig. 2-1 Fundamental optical layout for the twin laser beam phase modulated interferometer.

frequency fluctuation which is assumed to be enclosed in the phase term $\phi_p(t)$ and $\phi_R(t)$. $l_1 \sim l_4$ are the propagation distances indicated in Fig. 2-1, and $\phi(n_e)$ is the phase shift which the probing laser beam experiences inside a plasma. The electron density $n_e$ is obtained from the phase difference $\Phi$ between the probing and reference beat signals, which is written as

$$\Phi = \phi_p(t-\frac{l_1}{c})-\phi_p(t-\frac{l_3}{c})-\phi_R(t-\frac{l_2}{c})-\phi_R(t-\frac{l_4}{c}). \qquad (2.7)$$

Phase detection error $\Delta\Phi$ due to the frequency fluctuation is to the first approximation, supposing $\omega_B = \omega_p - \omega_R$,

$$\Delta\Phi \approx \frac{1}{c}[(l_3-l_1)\Delta\omega_p + (l_2-l_4)\Delta\omega_R]$$
$$= \frac{1}{c}[(l_3-l_1+l_2-l_4)\Delta\omega_p + (l_2-l_4)\Delta\omega_B]. \qquad (2.8)$$

For the case of JT-60, $l_1-l_3 = 40$ m and $l_2-l_4 = 2$ m. The designed value of resolution was set to be 1/100 fringe, since high-density (over $1 \times 10^{20}$ m$^{-3}$) plasmas are anticipated on JT-60. Substituting these numbers into (2.8),

$\Delta\Phi$ is rewritten as

$$\Delta\Phi \approx \Delta\omega_p \times 10^{-7} + \Delta\omega_B \times 10^{-8}. \quad (2.9)$$

Therefore, the achievement of 1/100 fringe resolution requires a frequency stability of the probing laser less than 100 kHz ($\Delta f/f = 4 \times 10^{-8}$) and stability of the offset laser frequency less than 1 MHz.

Another factor which may deteriorate the fringe resolution for heterodyne detection is the power stability. When the probing laser power is modulated by a(t) (<<1), electric field of the probing and reference lasers are written as

$$e_p = A_p[1+a(t)] \sin\omega_p t, \quad (2.10)$$

$$e_R = A_R \sin(\omega_R t+\alpha_R). \quad (2.11)$$

Beat signal $V_s$ is expressed as

$$V_s = KA_pA_R[1+a(t)] \times \left[\frac{A_p}{A_R}\frac{\tilde{a}(t)}{1+a(t)} + \cos(\omega_B t-\alpha_R)\right]. \quad (2.12)$$

Here, K is a constant determined by the attenuation of the propagating beam intensity and sensitivity of a detector, and $\tilde{a}(t)$ is the component of a(t) which comes into the detection bandwidth. The zero cross point is shifted to the maximum value

$$\Delta t \approx \frac{1}{\omega_B}\frac{A_p}{A_R}\tilde{a}(t). \quad (2.13)$$

In terms of the fringe resolution, (2.13) is written in the form

$$\Delta F \approx \frac{1}{2\pi}\frac{A_p}{A_R}\tilde{a}(t). \quad (2.14)$$

In order to restrict the fringe resolution below 1/100, the amount of amplitude modulation must not exceed 6 %, supposing $A_p = A_r$.

Mode purity, especially the beam propagation with $TEM_{oo}$ mode in a free space, which means the oscillation with the $EH_{11}$ waveguide mode inside the cavity, is essential to achieve the optimum propagation for a total path length over 130 m and to retain the undistorted wave front inside

a plasma. The interferometer signal is produced by the averaged phase shift $\Delta\theta$ along the laser beam diameter D:

$$\cos \Delta\theta = \frac{1}{D}\int_0^D \cos\phi(x)\, dx \qquad (2.15)$$

The value of D is generally large for large fusion experiment devices (typically 56 mm$\phi$ for the JT-60 interferometer). Therefore, the mode purity of the source laser is more keenly necessitated for the large plasma interferometry.

## 2. 2. DEVELOPMENT

The pump $CO_2$ laser employed in this work is consisted of a 2.5-m-long Pyrex tube with a coaxial coolant jacket and ZnSe Brewster windows on both ends. A 2.8-m-long cavity comprizes a grating and an output coupler made of a concave germanium mirror mounted on a PZT transducer. The cavity length was chosen experimentally so that the stable single-mode oscillation with large output power can be obtained. The grating and the germanium mirror were placed outside of the laser tube together with Brewster windows to water cool against the thermal displacement and

Table 2-1. Pump $CO_2$ laser parameters

| | |
|---|---|
| Line | 9.7 μm P(36) single |
| Cavity Length | 2.8 m |
| Discharge Length | 2.5 m |
| Bore | 8.8 mm$\phi$ |
| Grating | 75 lines/mm, water-cooled |
| Output coupler | 10 m radius, 30 % transmissivity Ge |
| $CO_2$ Gas Mixture | 11 % $CO_2$, 27 % $N_2$, 62 % He |
| Operating Pressure | 2.8 x $10^3$ Pa |
| Discharge Voltage | 15 kV |
| Discharge Current | 30 mA |
| Power | 77 Watts (Maximum) |
| Efficiency | 17 % |

damages. An anode electrode and gas inlet are situated right in the center of the cavity, and the cathode electrodes and the gas outlets are placed on both ends for the stability of the discharge. With a typical discharge voltage of 15 kV and the discharge current of 30 mA, the maximum output power of 77 W was obtained. A description of the pump $CO_2$ laser parameters is summarized in Table 2-1. Addition of 1 % Xe gas into the $CO_2$ gas mixture improved the pump $CO_2$ laser power by 5 %; however, the excessive addition of Xe gas destabilized the glow discharge to lower the output power.

The frequency stability of FIR lasers are mainly determined by the pump $CO_2$ laser frequency stability. The required frequency stability of the pump $CO_2$ laser to realize 1/100 fringe resolution can be estimated by the FM conversion coefficient,[2-2,3] which is reported to be less than 0.1 to yield 1MHz. In order to achieve this value, the pump $CO_2$ laser is (i) passively stabilized with Neoceram glass rods and a spacing made by combining the aluminum and Super Invar plates at the Ge output coupler support structure. The thickness of the spacing is calculated so as to cancel out the thermal shrink of the cavity length produced by Neoceram glass rods. (ii) For active stabilization, a reference $CO_2$ laser has been employed, which consists of a 1.3-m-long, 8.8-mm$\phi$-bore discharge tube tuned to a 9.7 $\mu$m P(36) branch with the same output coupler as the pump $CO_2$ laser. The passive stabilization technique employed on the pump $CO_2$ laser was also applied on the reference $CO_2$ laser. The output power is 7 W, and the center frequency $f_o$ of the gain curve is locked in a way to keep the first derivative signal of the power tuning curve to zero with a Lancing lock-in stabilizer model 80.214. The frequency of the beat signal produced by mixing the pump and reference $CO_2$ laser beam was F-V (frequency to voltage) converted to yield the off-set frequency control. An absolute frequency stabilization scheme such as the application of the opto-galvanic effect, Lamb dip,[2-4] Stark effect,[2-5] and an absorption cell[2-6] for the achievement of $f_o$ reproducibility is not required so far as to

suppress the frequency fluctuation under 1 MHz. The frequency fluctuation of the reference $CO_2$ laser was measured to be less than 80 $kHz_{p-p}$ by the tuning characteristics of the first derivative signal, and the offset frequency deviation was found to be less than 500 $kHz_{p-p}$ by the F-V converted signal.

The FIR waveguide laser comprises 2.0-m-long Pyrex tube, Ge étalon Brewster coupler, a ZnSe Brewster window, a Au-mesh coupler, and a wedged polyethylene output window as shown in Fig. 2-2. A silicon-substrate Ag-coated total reflector of 5-m radius of curvature has been employed to compose the cavity. The FIR parameters are listed in Table 2-2. The output power of FIR laser is 34 mW. This value was raised by 10 % with an addition of the 1.3 $cm^3$ per minute flowrate He buffer gas, which may have helped the vibrational relaxation and control of the gas temperature.

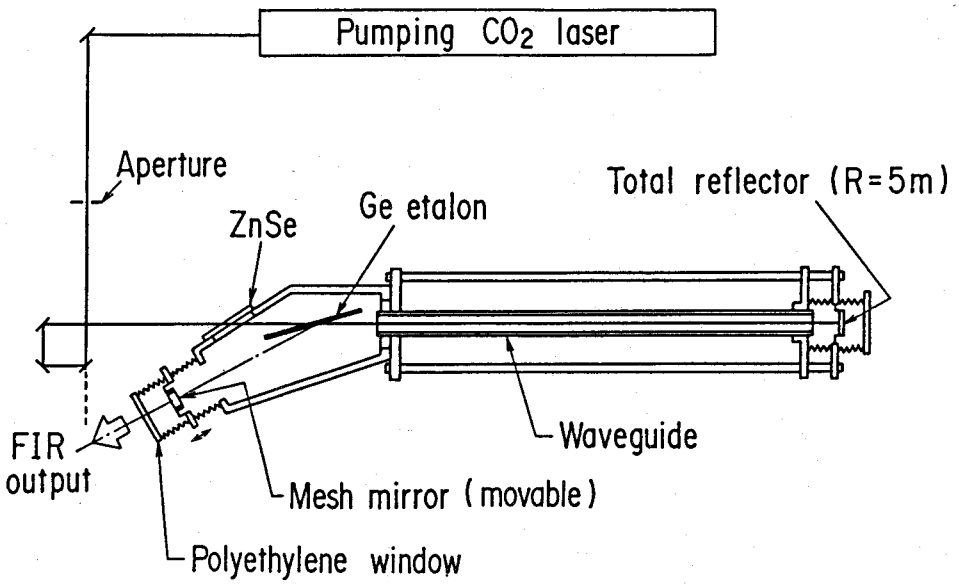


Fig. 2-2 Schematic of the Brewster-coupling CW118.8 μm $CH_3OH$ laser.

Table 2-2. FIR Laser Parameters

| | |
|---|---|
| Line | 118.8 μm single |
| Cavity Length | 2.40 m |
| Bore | 31.0 mm$^{\phi}$ |
| Input Coupler | Brewster Angle Ge etalon |
| Output Coupler | 12 % transmissivity Au-mesh (30 lines/mm) |
| Operating Pressure | 3.33 x $10^4$ Pa (280 mtorr ) |
| Transverse Mode | $EH_{11}$ single |
| Power | 34 mW ( Max. without buffer gas ) |

Mode purity is essentially governed by (i) the coupling device and (ii) the back talk of the $CO_2$ laser radiation. (i) As to the coupling device, a 1048-μm-thick étalon has been employed. It is placed at the Brewster angle for the p-polarized pump $CO_2$ laser beam and reflects the Q-branch s-polarized emission 95 % by the resonant effect.[2-7] The Ge étalon and its calculated reflectivity for the s-polarized 118.8 μm radiation is shown in Fig. 2-3(a) and (b) respectively. The Ge étalon suppresses the possibility of other unnecessary oscillations at the same time. Reflectivity of the étalon for the p-polarized radiation is less than 2 %. Therfore, the simultaneous oscillation of the 170.6 μm $CH_3OH$ line is well suppressed. Since the pump $CO_2$ laser beam does not have to be collimated into a beam into a coupling-hole, which is often seen in conventional FIR lasers, it is introduced into the FIR cavity without the beam parameter modification with optical components. The beam diameter is 15 mm$^{\phi}$ at the entrance of the 31 mm$^{\phi}$ inner diameter FIR waveguide. This is effective to realize the homogeneous pumping of the laser media. Furthermore, the pump $CO_2$ laser beam, being unfocused, damages the ZnSe window very little. In comparison with conventional FIR lasers with a hole-coupler, homogeneous pumping through the Ge étalon, which means that the pump $CO_2$ laser beam is not diffracted at the coupling-hole, yields a Gaussian-type

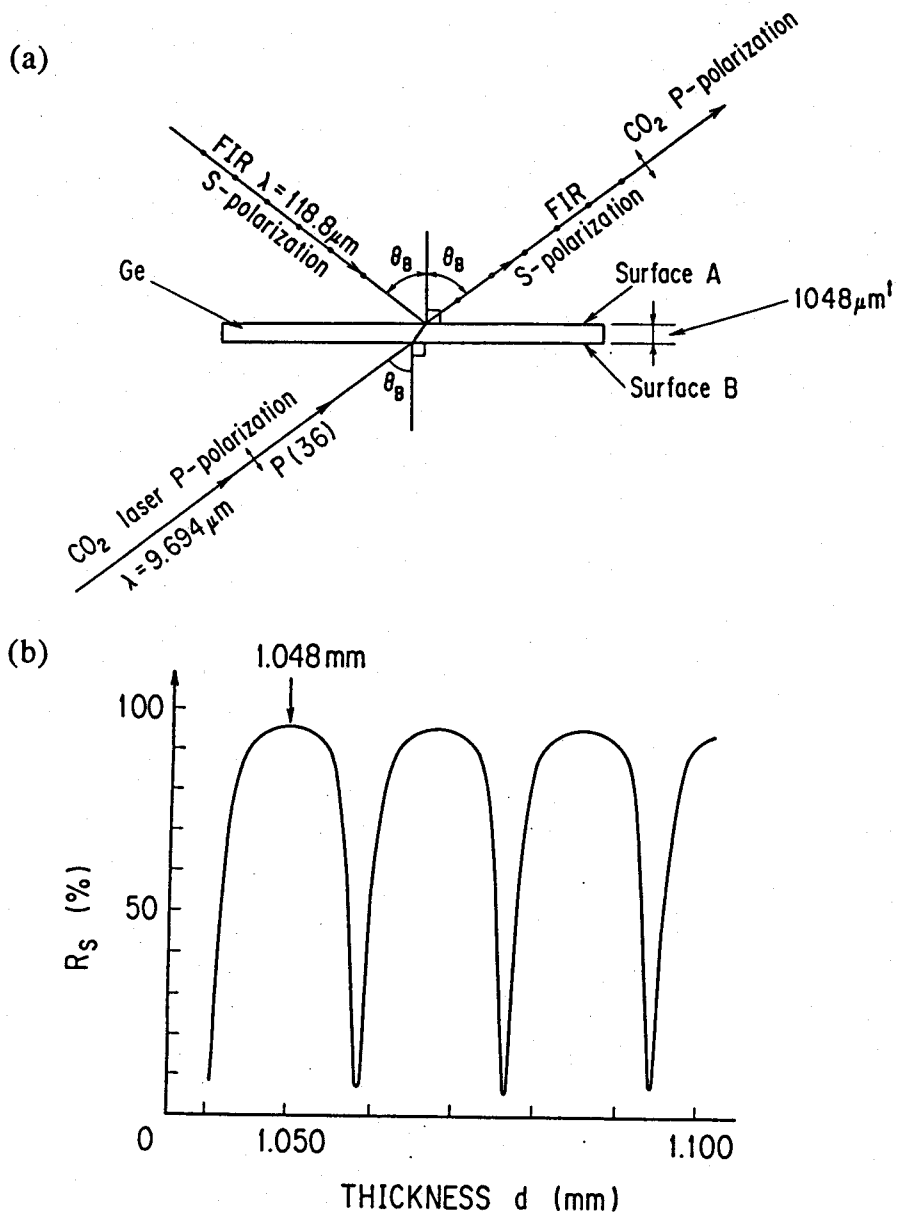


Fig. 2-3 (a) Schematic of the Ge etalon and (b) the calculated reflectivity of the Ge etalon for the s-polarized 118.8 μm laser light.

transverse mode. The capacitive mesh coupler,[2-8] on the other hand, does not necessarily produces the spatial intensity distribution suited for the low-order waveguide mode, and it suffers from the intensity loss at the mesh aperture to deteriorate the power conversion efficiency. (ii) Although the removal of optical feedback has been one of the prime issues for the mode purity and stability of optically pumped FIR lasers, a few works are reported on the suppression of self-beating oscillations.[2-9,10,11] In order to restrain the optical feedback, a 10 $mm^{\phi}$ aperture have been placed in the $CO_2$ laser beam path; the reflected $CO_2$ laser beam at the concave mirror in the FIR cavity focuses right before the aperture and diverges so that only a fraction of the beam intensity goes back into the pump $CO_2$ laser cavity. The tunable output coupler is isolated from the pumping beam to assure the elimination of the optical feedback even in a tuning operation of either pump $CO_2$ or FIR lasers.

The mesh output coupler, being off the pump $CO_2$ laser irradiation, provides the uniform output profile without any damage or deformation, and the effect of the $CH_3OH$ gas pressure ripple to the mesh output coupler was not observed. When the 12 % transmissivity Au-mesh output coupler was replaced with that of 6 % transmissivity, a multi-mode oscillation of $EH_{11}$, $EH_{12}$ and $TE_{02}$ + $EH_{22}$ was observed. The ZnSe window, Ge étalon, and the total reflector are water cooled for their thermal stability. The whole laser cavities including the pump and reference $CO_2$ laser and all the optical components are mounted on a air-cushioned honeycomb bench to reduce the fast-frequency component of the external vibration, while the low-frequency component was removed by the rigid structure of laser cavities and optical components on the honeycomb bench. The ambient atmosphere was vapor-purged with dry air up to the relative humidity of 2.5 %.

The tuning curve, the tuning characteristics of the first derivative signal, frequency drift during the free-running and power stability of the developed $CH_3OH$ laser are shown in Fig. 2-4. The smooth curvature and the periodical single peaks of the tuning curve prove a single longitudinal-mode oscillation. The frequency drift of the free-running probing laser and the stability of the offset frequency for 10 s, which is the plasma pulse duration of the JT-60 tokamak, were less than 25 and 2.5 kHz, respectively, while the power stability for 10 s was 0.03 %. These outstanding performances owe to the total suppression of the optical feed back and superior thermal and mechanical stability of the FIR cavities.

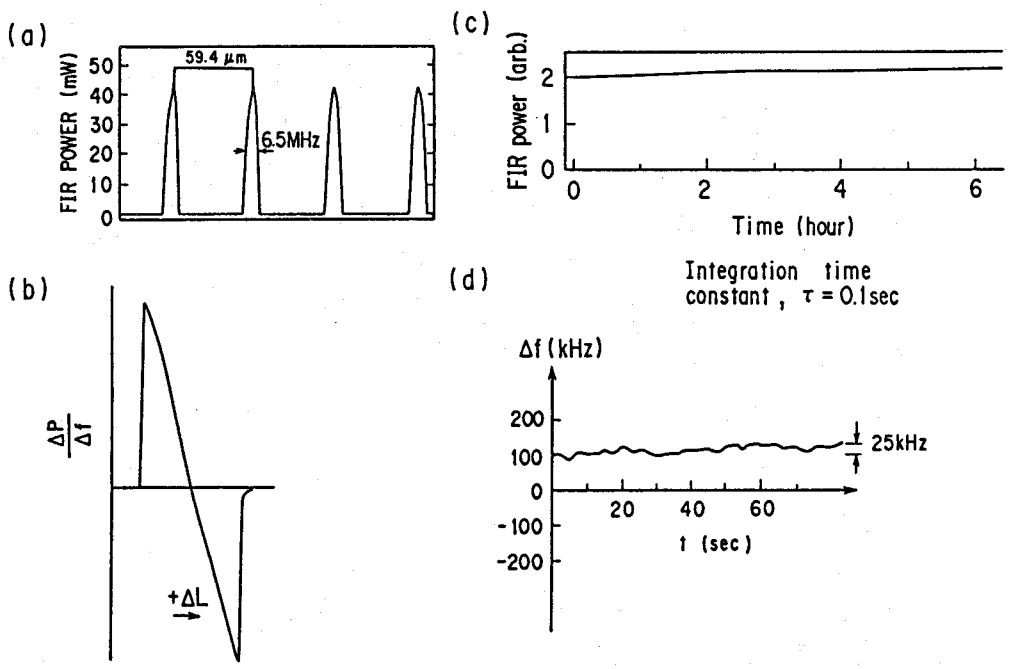


Fig. 2-4 The performances of the Brewster-coupling CW118.8 μm $CH_3OH$ laser: (a) Power tuning curve, (b) The tuning characteristics of the first derivative signal, (c) Power stability, and (d) Frequency drift during the free-running.

The effectiveness of this newly developed coupling device concerning the longitudinal-mode selectivity has been examined in an experimental arrangement shown in Fig. 2-5. A hole-coupling FIR laser cavity was prepared, which comprises the same dimension of the waveguide as the Brewster-coupling laser and a Au-coated silicon-substrate flat mirror with a 4 mm$^{\phi}$ input aperture. The tuning characteristics and output spectra of these FIR lasers have been observed. When the pump $CO_2$ laser beam was lead into both of these cavities, a multimode oscillation which originates in the pump $CO_2$ laser has induced self-beat oscillations on both types of FIR lasers as shown in Fig. 2-6(a). This multimode oscillation is induced by the optical feedback from the hole-coupling FIR laser cavity. In the case when the hole-coupling cavity is tuned so as to suppress the optical feed back, the self-beat spectra on the Brewster-coupling cavity disappeared, while on the other hand, multimode waveguide oscillations were observed on

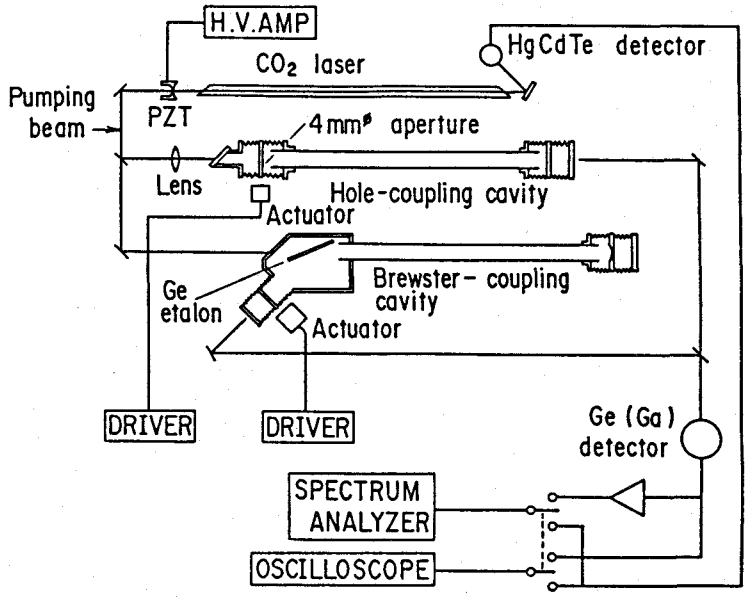


Fig. 2-5 Experimental configuration for the evaluation of the longitudinal mode selectivity concerning the self-beat oscillation and the tuning characteristics of the Brewster-coupling cavity in comparison with the hole-coupling cavity.

the hole-coupling FIR laser as shown in Fig. 2-6(b). The typical tuning characteristics of the hole-coupling laser is depicted in Fig. 2-6(c). The multiplemode oscillation with frequency shift caused by the mode-pulling effect is shown in the figure.

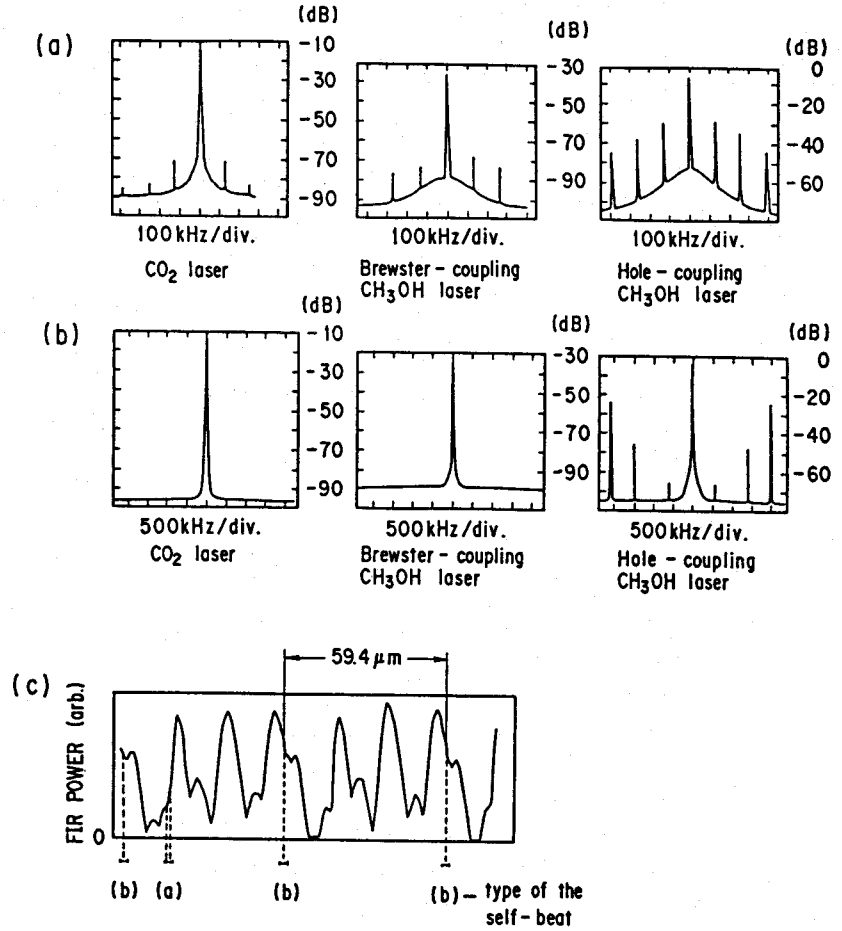


Fig. 2-6 The self-beat spectra due to (a) the back talk of the pump $CO_2$ laser beam and (b) the waveguide multi-mode oscillation. Beat levels are expressed in dB unit, representing 0 dB as the DC input level. The power tuning curve (c) corresponds to the two types of the self-beat spectra (a) and (b).

In order to reproduce the accomplished short-term stability for 10 s for every tokamak plasma pulse, which is repeated in every 10 min, FIR lasers have also been actively stabilized. The cavity length of the probing laser is AC modulated by mounting the total reflector on a PZT transducer in order to detect the first derivative signal with a lock-in amplifier. The cavity length is step controlled with a stepping motor so as to bring the modulated output power signal to zero. The reference laser cavity is tuned so that the F-V converted beat signal frequency, produced by mixing the probing and reference laser beam, is locked to 2.0 MHz ± 100 kHz with a stepping motor. The whole active frequency stabilization scheme is depicted in Fig. 2-7. The stabilization control is sequentially actuated by the command signal sent from the JT-60 central control system.[2-12] The probing laser cavity modulation and the reference laser cavity tuning with the stepping motor, which are carried out during tokamak plasma pulse intervals, are turned off 10 s before the plasma pulse to start free running of the probe laser and DC off-set frequency control with a

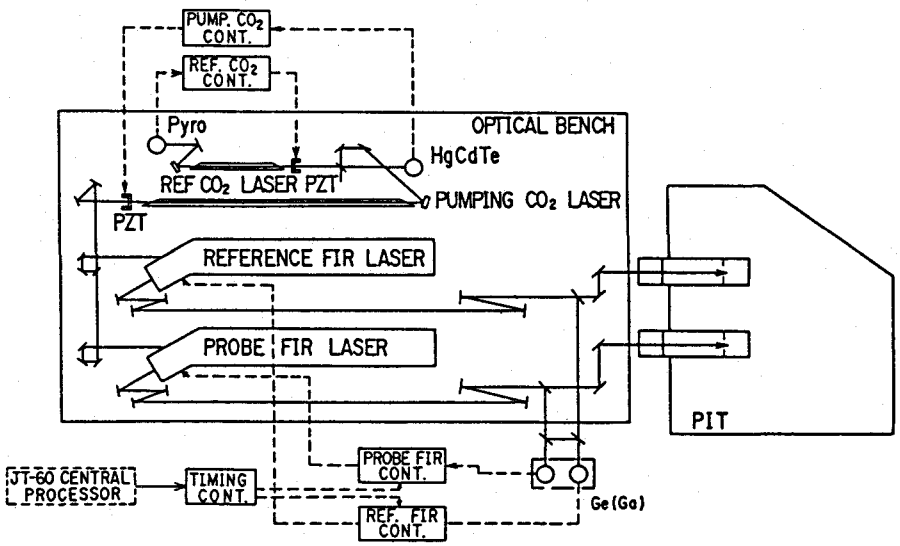


Fig. 2-7 Active frequency stabilization scheme.

PZT transducer for 30 s. Since high stability of the offset frequency have been realized, a narrow bandwidth detection circuit can be applied to yield higher S/N ratio. The deviation from the center frequency and the 2 MHz standard offset frequency under the sequential control are shown in Fig. 2-8(a) and (b), respectively. It demonstrates the effectiveness of this stability control circuit. The relationship among the FIR output power, pump $CO_2$ laser frequency, and the alcohol gas pressure is shown in Fig. 2-9. The maximum FIR output power is obtained for the pump frequency offset of -12 MHz from the gain center of the P(36) line and the alcohol gas pressure of 250 mtorr. The far-field transverse mode pattern was measured by scanning a pyroelectric detector. The Gaussian shaped

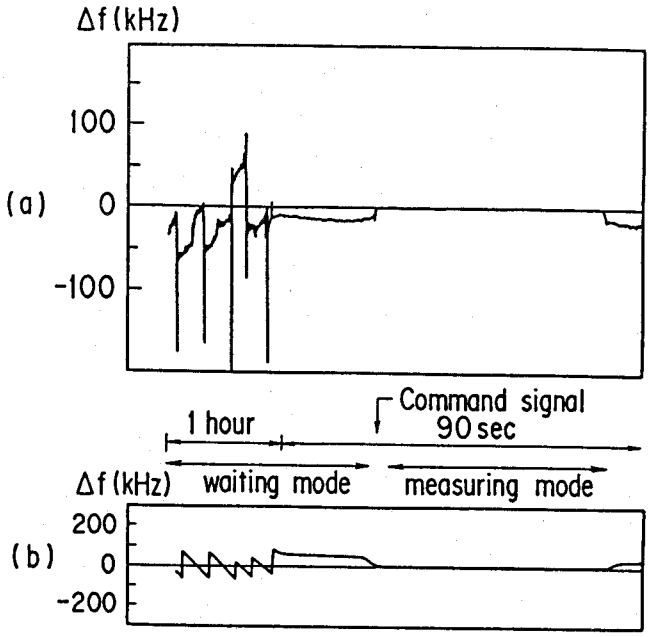


Fig. 2-8 Frequency stability of the twin $CH_3OH$ lasers under the control circuit. (a) The fluctuation of the offset frequency.
(b) The first derivative signal of the probing $CH_3OH$ laser.

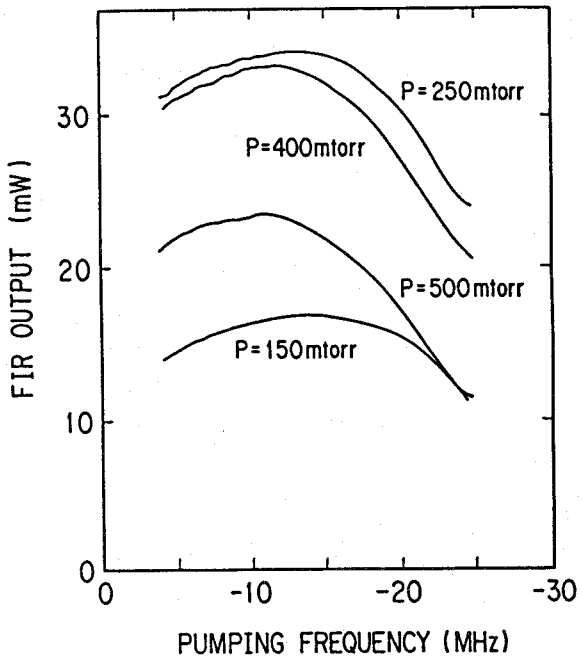


Fig. 2-9 Output power of the $CH_3OH$ laser versus the pump $CO_2$ laser frequency expressed as the off-set from the gain center of the 9.7 μm p(36) branch.

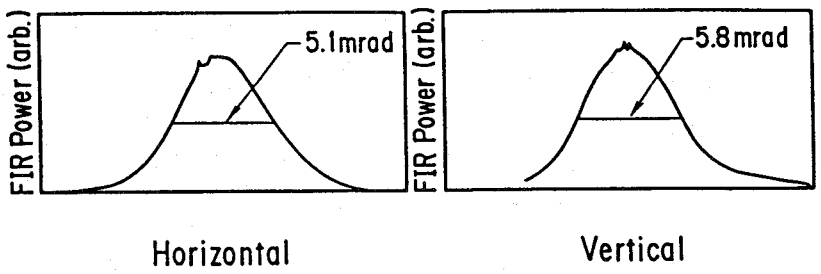


Fig. 2-10 Far-field transverse mode patterns of the Brewster-coupling $CH_3OH$ laser.

profile with a 12 mm$^{\phi}$ diameter has slight anisotropy in the spatial intensity distribution as shown in Fig. 2-10; it is somewhat elongated in the horizontal direction. The horizontal beam divergence was larger than expected from the inner diameter of the waveguide. It is supposed to be caused by the beam walk-off[2-13] effect inside the Brewster étalon. The degree of linear polarization was measured with two grid polarizers one right next to another to be found more than 99.98 %, which is enough for the polarimetric measurement.

The newly developed FIR laser system has been in operation on JT-60 for two years, yielding reliable data including the real-time electron density feedback control with fuel gas injection valves. The system is totally adjustment and maintenance-free for two weeks which is the period the $CO_2$ gas mixture holds. Ga-doped Ge detectors used for frequency stabilization and beam power monitoring are cooled down to 4.3 K by a vibration-isolated mechanical Joule-Thomson refrigerator which can be operated without any attendant complications for more than 6 months.

## 2. 3. CONCLUSION

The combination of (i) the Ge étalon Brewster-coupling cavity and (ii) the frequency stabilization scheme with the cavity length compensation (passive stabilization) and the cavity length modulation technique (active stabilization) has proven to have sufficient frequency stability and the mode purity for the large tokamak interferometry, enabling the totally adjustment-free and reliable operation.

Ge étalon as a Brewster angle beam coupler was shown to be effective to pump Q-branch s-polarized radiation with p-polarized pump laser light for the mode purity. The difficulties when a coupling hole is employed have been also demonstrated. The key items for the elimination of the multi-mode oscillation have been found to be (1) The homogeneous pumping of the laser media and (2)

The suppression of the optical feed back with (a) an aperture in the $CO_2$ laser beam path, (b) the appropriate selection of the distance between the pump $CO_2$ laser and the FIR laser cavity, (c) the reflector curvature in the FIR cavity, and (d) the reflectivity of the mesh output coupler.

The gain band-width which developed single-mode 118.8-μm $CH_3OH$ laser showed was 6.5 MHz. The obtained power conversion efficiency of the single-mode pump $CO_2$ laser to the single-mode FIR laser was 0.088 %, owing to the improved reflectivity of the excited 118.8-μm radiation by the Ge étalon beam coupler. The ratio of the FIR power fluctuation to the pump $CO_2$ laser fluctuation was 1.1. This value is consistent with the evaluation done by Lourtioz *et al* [2-14]. The conversion coefficient of the frequency fluctuation was 0.05. From the Plainchamp's experimental results, the low conversion coefficient of 0.05 implies that the offset frequency of -12 MHz is very close to the CH3OH absorption line center, where the frequency modulation of the pump $CO_2$ laser affects that of $CH_3OH$ laser very little. The fringe resolution determined by the frequency and power stability of the newly developed FIR laser (U. S. Patent Number: 4683576) is well below the overall fringe resolution of the JT-60 interferometer which is actually governed by the fringe counting circuit to be 1/100.

## REFERENCES TO CHAPTER 2


2-1 S. M. Wolfe, K. J. Button, J. Waldman and D. R. Cohn, Appl. Optics **15**, 2645(1976).

2-2 A. Godone, C. O. Weiss, and G. Kramer, IEEE J. Quantum Electron. **QE-14**, 339(1978).

2-3 P. M. Plainchamp, IEEE J. Quantum Electron. **QE-15**, 860(1979).

2-4 C. Freed and A. Javan, Appl. Phys. Lett. **17**, 53(1970).

2-5 P. Minguzzi and M. Tonelli, J. Phys. E **10**, 775(1977).

2-6 R. G. Brewer, M. J. Kelly, and A. Javan, Phys. Rev. Lett. **23**, 559(1969).

2-7 D. A. Naylor, R. T. Boreiko, and T. A. Clark, Appl. Opt. **17**,1055(1978).

2-8 D. A. Weitz, W. J. Skocpol, and M. Tinkham, Opt. Lett. **3**, 13(1978).

2-9 J. Heppner and C. O. Weiss, Appl. Phys. Lett. **33**, 590(1978).

2-10 D. K. Mansfield, A. Semet and L. C. Johnson, Appl. Phys. Lett. **37**, 688(1980).

2-11 H. P. Rüser, M. Yamanaka, R. Wattenbach and G. V. Schultz, Int. J. of IR & MM Waves **3**, 839(1982).

2-12 H. Yokomizo, H. Takeuchi, T. Fukuda, T. Sugie, T. Nishitani et al., Fusion Engineering and Design **5**,117(1987).

2-13 W. R. Leeb, Appl. Opt. **6**, 267(1975).

2-14 J. -M. Lourtioz, R. Adde, D. Bouchon and J. Pontnau, Revue de Physique Appliquèe **14**, 323(1979).

# CHAPTER 3. CW118.8-μm $CH_3OH$ LASER / 2-mm WAVE MULTI-CHANNEL POLARI-INTERFEROMETER FOR ELECTRON DENSITY AND FARADAY ROTATION ANGLE MEASUREMENTS ON JT-60

Although several experiments on the far-infrared (FIR) interferometry have been reported on the medium-sized tokamaks, conventional interferometers are no more sufficient to obtain reliable data for the large tokamak applications without the further development of a frequency-stabilized single-mode FIR laser, research on the long distance propagation technique, and investigations on the effect of enlarged beam diameter. A multi-channel cw118.8-μm $CH_3OH$ laser/2-mm wave polari-interferometer system feasible enough for JT-60 diagnostics has been newly developed. The system reliably performs the real-time feedback control of electron density with a fast direct read-out digital fringe counter, and 2-mm wave system successfully precluded restrictions concerning the diagnostic accessibility. The 2-mm wave interferometer also works effectively to yield adequate electron density resolution for the magneto-hydrodynamic (MHD) activity study and edge plasma density measurements. Application of the developed polarimeter has enabled the evaluation of current density profiles, combined with a MHD equilibrium code. In the divertor region, high resolution FIR interferometry has been successfully undertaken for the first time on the high density small volume plasma.

The items of developments and performances are reported in this chapter together with the results of Faraday rotation angle measurements, which yields direct informations on the current density profile. Evaluation schemes of the obtained results are also mentioned to describe the developed polari-interferometer system as a

complete plasma diagnostic device for the interpretation to physics quantities.

## 3. 1. INTRODUCTION

According to the enlargement of the plasma volume for the improvement of confinement properties, conventional interferometers reveal their intrinsic difficulties in interpreting the phase shift data with an adequate resolution, which was subtle enough when applied on the medium-sized fusion experiment devices. Imposed requirements which previous interferometers envisage are mainly attributed to the long-distance propagation of laser beams, and namely they are:

(a) Development of a single-mode and frequency-stabilized FIR laser.
(b) Investigations on the effect of enlarged beam diameter, especially concerning the distortion of the wave front due to the electron density gradient inside the propagating beam volume.
(c) Research on the stable and low-loss long-distance propagation technique.
(d) Development of the optical components for the effective beam power distribution and polarization separation.

The results of research and developments on these items except (a), which is already discussed in chapter 2, are reported in this chapter.

Another aspect of limitation pertinent to large tokamak applications is the restricted diagnostic accessibility to obtain informations over the full plasma volume. This condition would be forced more rigorously on the future large fusion devices, which are operated with D-T (deutrium and tritium) plasma components and equipped with a large blanket (energy conversion device). With a 2-mm wave circuitry inside the JT-60 vacuum vessel, edge

electron density, where there is no diagnostic port prepared, have been successfully measured. As for the evaluation of the electron density profile with the limited number of diagnostic chords, an equilibrium calculation combined with the results of magnetic probe measurements and the Faraday rotation angle measurement has been employed. The obtained electron density profile agreed within the accuracy of 10% of the electron density data measured by Thomson scattering.

On another matter, the whole interferometer system has to be operated and monitored remotely under the supervise of the programed communication network controlled by a host computer, and all the components are supposed to function reliably without any maintenance complications for a long period, since the residual levels of radioactivity in the vicinity of the tokamak will preclude all the maintenance personnel.

## 3. 2. DESCRIPTION OF THE JT-60 INTERFEROMETER SYSTEM

The fundamental layout of the newly developed multi-channel CW118.8-μm $CH_3OH$ laser/2-mm wave polari-interferometer to cope with the requirements mentioned above is shown in Fig. 3-1. The FIR system employs 2 MHz beat-modulated twin $CH_3OH$ lasers[3-1] with Michelson configuration similar to that described by Wolfe et al.,[3-2] providing 3 chords ($R$ = 2.53, 3.04, and 3.55 m) in the main plasma region and 2 chords in the divertor region; the first interferometric measurement in this particular region yields direct information on the particle flow along the magnetic field, and it is especially effective for the physical understanding of the electron density clamping of neutral beam heated plasmas.[3-3] The diagnostic chords are summarized in Fig. 3-2.

The FIR lasers are mounted on the air-cushioned honeycomb bench for the mechanical cavity stability, and

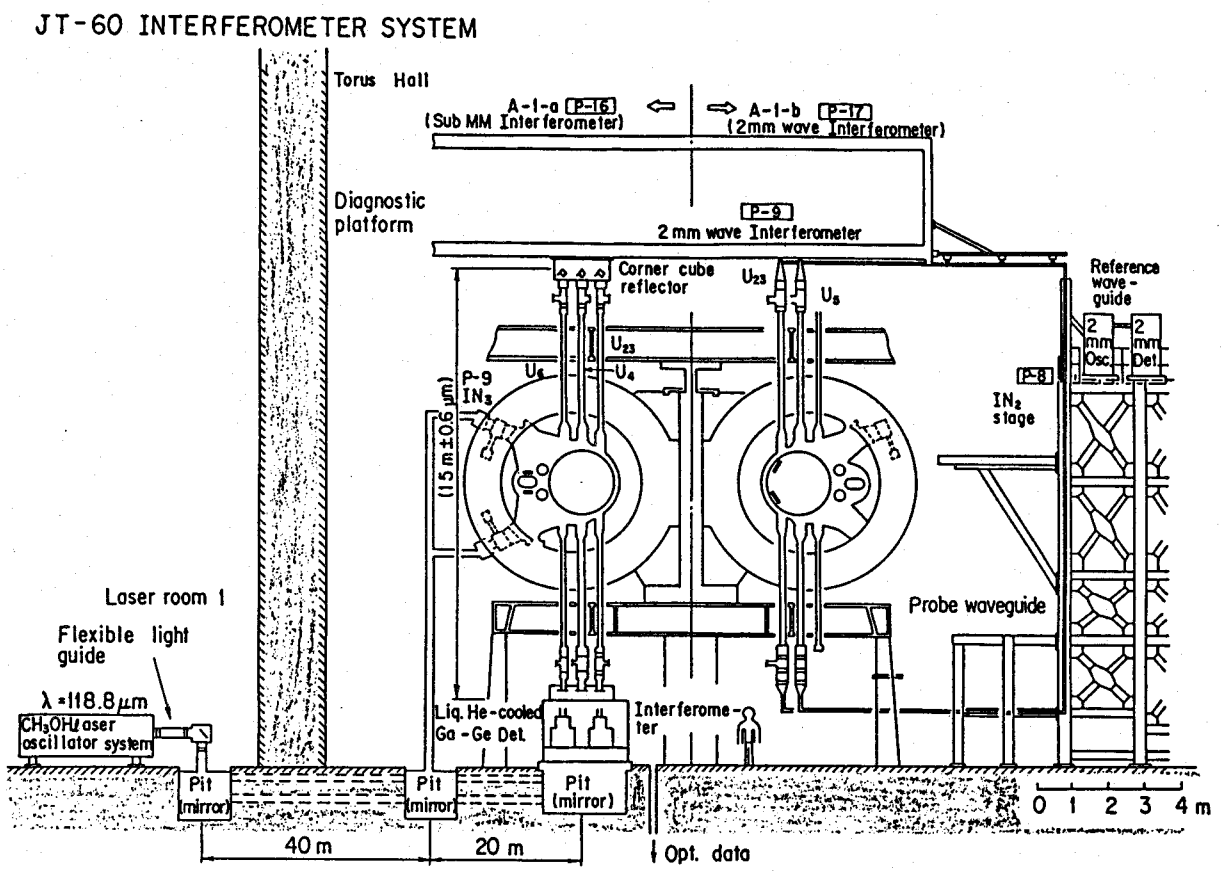


Fig. 3-1 The schematic layout of the JT-60 interferometer system

The FIR lasers are mounted on a air-cushioned bench outside of the JT-60 torus hall. The FIR beams are fed into floor buried 40/20 m-long tubes through flexible light-guides and the telescopic optics for the free space propagation. Probing FIR laser beams are combined with 0.63-mm He-Ne laser beams inside the interferometer optics. For the main plasma measurement, corner-cube reflectors are installed below the diagnostic platform right above the JT-60 torus. For the divertor region measurement, probing beams are split inside a pit. Ge(Ga) detectors are placed right next to the interferometer optics. The 2-mm wave interferometer components including the are situated on a diagnostic stage inside the torus hall heavily shielded, and the 70-m delay lines are enclosed in the IF circuit.

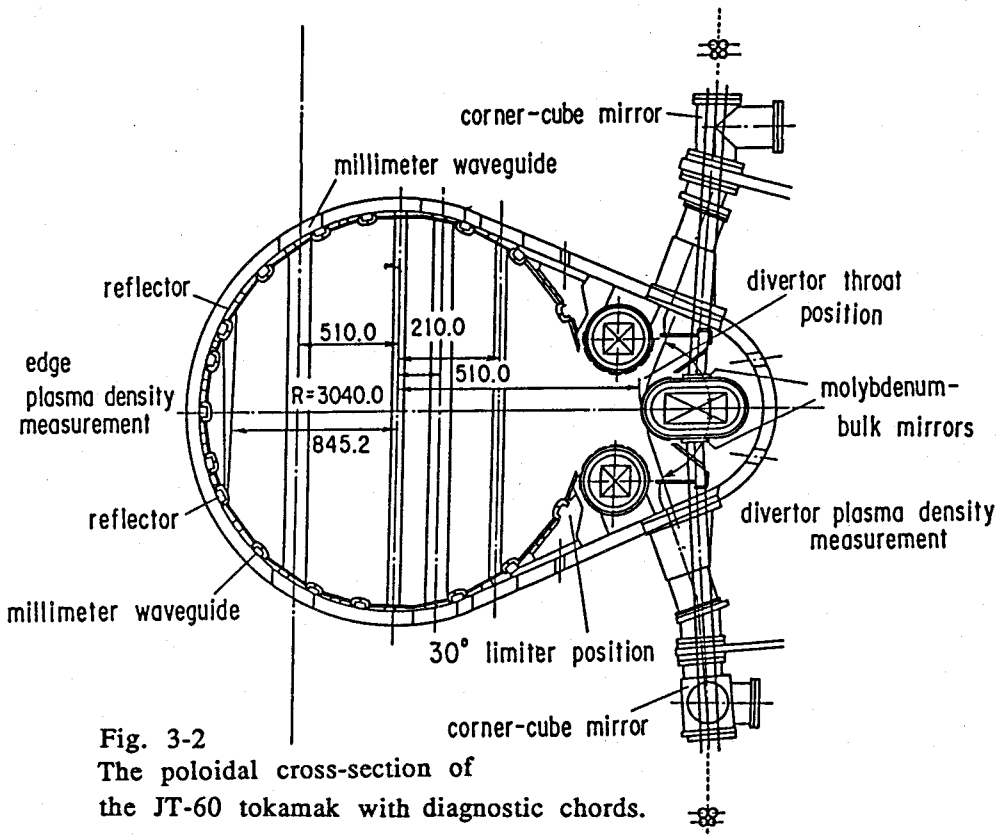


Fig. 3-2
The poloidal cross-section of
the JT-60 tokamak with diagnostic chords.

they are located outside of the JT-60 torus hall to exclude the effect of the stray magnetic field and external vibration. This layout leads to the total propagation distance of the probing beam over 130 m. The FIR beams, after being their propagation axes stabilized by the flexible light-guide and their optical parameters converted by the telescopic optics,[3-4] are lead into the floor buried 40/20 m-long 0.15 m$^{\phi}$ tubes for the free space propagation. Beam splitters are made of X-cut crystal quartz plates of which thicknesses are determined so as to provide the desired distribution ratio to each chords by the resonant effect.[2-7] Probing FIR laser beams are combined with 0.63-μm-He-Ne laser beams for the vibration compensation.[3-5] For the main plasma measurement, Zero-dur-substrate gold-coated corner-cube-reflectors (CCR) are installed inside the vacuum region and

fixed below the diagnostic platform right above the JT-60 torus to dismiss the large structures above the floor level for reliability and compactness. The TFTR and JET interferometer system[3-6,7] employs a massive frame (12 meters tall and 30 tons in weight for TFTR) which encircles the tokamak. The injection beam into the plasma and the returning beam trace a different beam path to suppress the optical feedback to FIR lasers as well as the crosstalk inside the interferometer chamber, otherwise an optical isolator has to be developed, as seen in the TFTR interferometer.

As to the divertor region measurement, CCR is fixed on the toroidal coil spacings. Probing beams are injected from the upper and lower oblique diagnostic ports to be reflected by molybdenum flat mirrors placed above and below one of the divertor coils. Molybdenum metallic mirrors are intended to resist the erosion and sputtering by the heat flux and particle bombardment from the plasma, and they are in the shadow of the divertor plates, which have a 45 mm width gap for the beam transmission. Reflected beams are directed to the CCR at the far ends of the diagnostic ports in order to compensate the displacement of beam axis due to the mechanical vibration which can be caused by the plasma discharge. After another reflection at the molybdenum mirrors, probing beams return to the interferometer optics to yield the bundled beam size of ±30 mm from the intersection point of the magnetic field lines and divertor plates. Therefore the amount of phase shift is quadruplicated to yield high S/N ratio.

Ge(Ga) (gallium doped germanium) detectors are cooled down to 4.3 K by a Joule-Thomson refrigerator which can be continuously operated over 5,000 hours without any attendant complications. Detector windows are also wedged to eliminate the backtalk.

One chord ($R$ = 3.55 m) has been prepared for the Faraday rotation measurement. The optical layout for the concomitant measurement of the Faraday rotation angle with line electron density is shown in Fig. 3-3. The current density profile is of basic and primary interest as it is recognized to be a key to the improvement of confinement and the gross MHD stability. However, it is hardly diagnosed reliably in large fusion experiment devices, where the linear polarization of the probing laser beam is considerably elliptized because of the high electron density and large toroidal induction along the long penetration distance inside the plasma. The primary reason that we have chosen 118.8-μm radiation (the same as the TFTR system) is to suppress this elliptization effect of the linearly polarized probing beam (Cotton-Mouton effect),[3-8,9] as well as to sustain the rotation angle at desirable values. The expected Faraday rotation angle and ellipticity are calculated to be 19 degrees and 0.015 (over 99.9% in terms of the degree of linear polarization) respectively. The rotation angle has been measured as an intensity ratio of the lock-in amplified 2 MHz heterodyne beat signals produced by mixing each orthogonal polarization components with the reference wave.[3-10] The lock-in detected signal is low-pass filtered to yield the frequency response of 5 kHz. All the signal processing electronincs have been designed so as to maintain linear responses in the range of interest, and calibration of the rotation angle with a half-wave etalon plate is carried out remotely for every plasma pulse with a motor-drive unit actuated by the timing signal sent from the JT-60 central control system.[2-12] The resolution of Faraday rotation angle has been confirmed to be less than 0.25°.

The lock-in detected signal is low-pass filtered to yield the frequency response of 5 kHz. X-cut crystal quartz made polarizing beam splitters were employed in order to analyze the probing beam of large diameter ($d_{1/e^2}$=75 mm$^{\phi}$ ) with adequate resolution.

DIAGNOSTIC LAYOUT

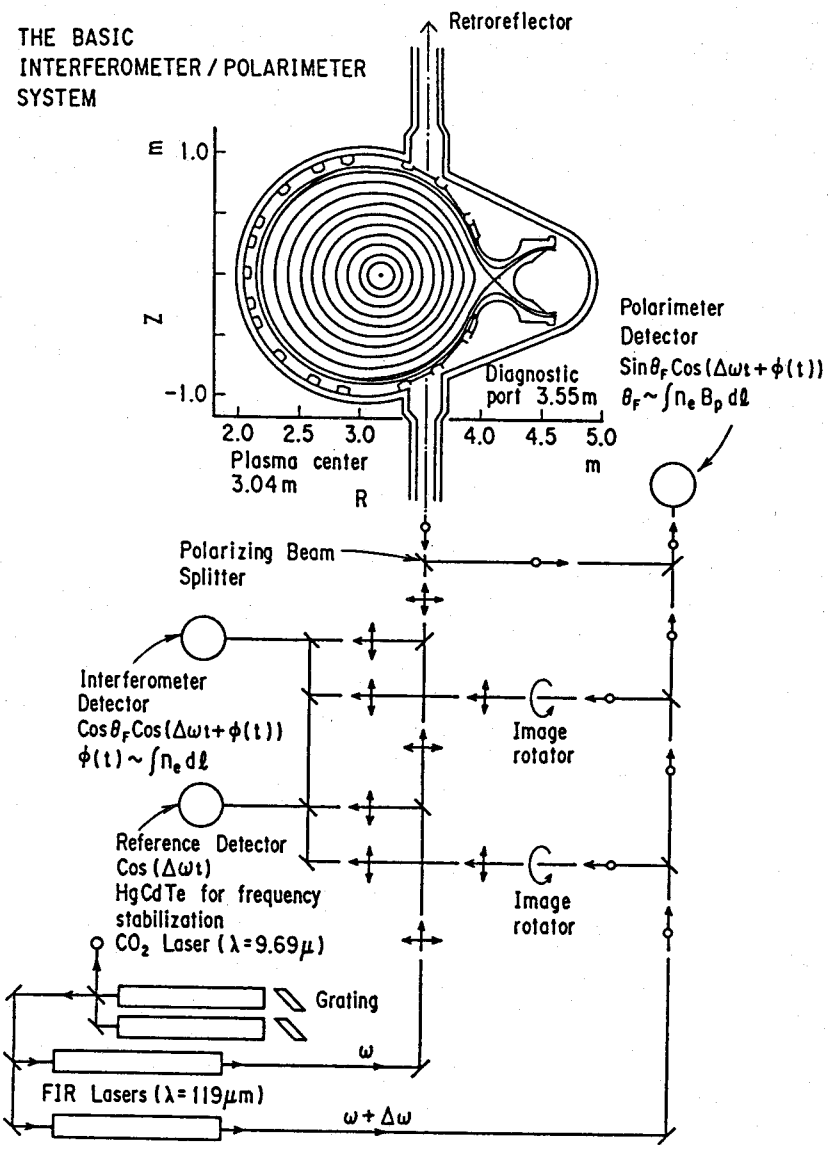


Fig. 3-3 Optics for the concomitant measurement of Faraday rotation angle with line electron density.

The 2-mm wave interferometer system employs super-heterodyne detection method[3-11] to obtain deisrable S/N ratio, and it is intended to obtain adequate resolution for the MHD activity study and edge plasma measurement, providing 2 chords in the main plasma region ($R$ = 2.19 and 3.25 m). For the measurement of the edge plasma density ($R$ = 2.19 m), where there is no diagnostic port prepared, 304 stainless steel made millimeter wave circuit was installed on the inner wall of the JT-60 vacuum vessel to yield the accurate evaluation of the electron density profile and informations on the injection of light impurities from the first wall as well as the edge localized phenomena such as MARFE.[3-12] This method is expected to be effective for the future large fusion devices of which accessibility to a plasma is severely limited. The EIO (Extended Interaction Oscillator), IF circuit and harmonic mixers are placed inside the torus hall heavily shielded, and the delay lines are enclosed in the IF circuit. In order to dismiss the degradation of resolution due to the oscillator frequency fluctuation, the length of delay line is adjusted to match the total probing circuit length of 70 m.

The 2 MHz beat signals are electro-optic converted in about 75 mm from the Ge(Ga) detectors to dismiss the intrusion of radio frequency (2 GHz) noise from the plasma heating Klystrons and stray magnetic field. The optical signal, after transmitting through the 250-m long optical fiber cable, is opto-electric converted in a shielded room to be fed to the fringe-counting circuit. The fringe counter is equipped with a 200 MHz crystal oscillator and eight 4-bit up-down counters to comprise the fractional and integer fringe-counting circuit. Both of the probing and reference beat signals are converted to pulse trains, and they are phase-locked by the 200 MHz clock pulse to be sent to the fractional and integer counting circuit respectively through the voltage comparator circuit for the signal level discrimination. For the fractional counting, the reference

beat pulse starts the 200 MHz clock pulse, and the after-coming probing beat pulse stops it. Therefore the number of 200 MHz clock pulse is directly related to the fraction of the fringe shift. In the integer part, number of probing beat pulses within two consecutive reference beat pulses and vice versa are counted. In order to eliminate the counting ambiguity, concerning the rationality between the integer and fraction counting circuit, for the case when the probing beat pulse is close to the reference beat pulse in time, we have divided the time interval of two consecutive beat pulses into three regions and added a logical operation circuit. The frequency of the reference beat signal is also counted as a number of the 200 MHz clock pulse to calibrate the offset frequency fluctuation. The counting results are stacked in a 16 bit register every 500 ns and sampled by 200 kHz and 1 kHz latch pulses. The whole FIR/2 mm wave system is controlled and monitored remotely through a CAMAC interfaced serial highway controlled by a auxiliary computer which communicates with the JT-60 central control system through optical fiber link, which yields the reliability of long-term maintenance-free operation to be capable of future D-D discharge large tokamak experiments. Another auxiliary computer directly accesses the memory and converts the counting results to line electron density every 1 ms for the real time feedback control which employs the fuel gas injection valve. Since a fringe-counting error may induce severe major disruptions, we have designed so as to stop the real time feedback control according to the system status and results of the signal level discrimination mentioned above.

## 3. 3 DEVELOPMENT

### 3. 3. 1 DETERMINATION OF THE EFFECTIVE BEAM DIAMETER

It has been said that the so-called concave lens effect of density gradient causes only two problems for the small

to medium sized tokamak; distortion of ray trajectory and diffusion of beam power.[3-4,13,14] However, the third serious problem arises in large tokamak applications, that is, a significant phase difference occurs inside of the probing beam after penetrating through a plasma. It limits the aperture or the beam diameter, and consequently limits the S/N ratio. When the local phase varies across the diameter of the probing beam, the detector will sense, to the first approximation, an average phase shift $\Delta\theta$ given by

$$\cos\Delta\theta = \frac{1}{D}\int_0^D \cos\phi \, dx \,, \tag{3.1}$$

where $\phi$ is the local phase change at position x along the beam diameter $D$ . The value of $\Delta\theta$ as a function of the maximum phase difference, $\phi_0[= \phi(D/x)]$ is shown in Fig. 3-4. This result suggests that a significant error may be introduced when the value of $\phi_0$ exceeds $\pi$. Thus, this effect sets limit to the beam diameter for a given value of the density gradient. Evaluations of beam diameters are made

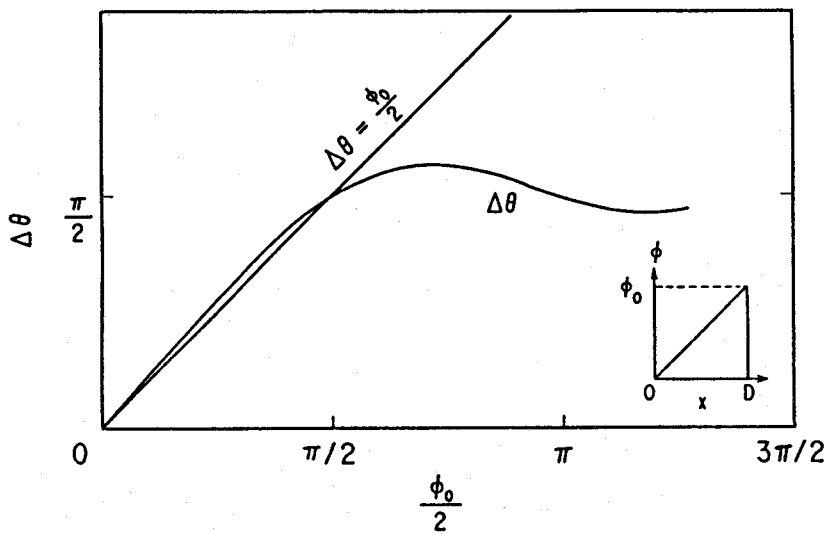


Fig. 3-4 The calculated value of the averaged phase shift over the beam diameter as a function of the maximum phase difference $\phi_0 = \phi(D/x)$.

in the followings for the three types of interferometers, assuming the parabolic density distribution: $n_e(r) = n_{eo}(1 - r^2/a^2)$.

For the Mach-Zehnder type(employed on the JET interferometer), the phase difference across the beam diameter is expressed as a product of the chord density gradient and the beam diameter:

$$[\frac{d}{dx} n_e(x)\, l]\cdot D = \{\frac{d}{dx}\, n_{eo} \int_{-\sqrt{a^2-x^2}}^{\sqrt{a^2-x^2}} [1 - (x/a)^2 - (y/a)^2]\, dy\}\cdot D \tag{3.2}$$

The following condition is then imposed on the beam diameter:

$$[\frac{d}{dx} n_e(x)\, l]\cdot D \le |\, n_{eo}\, l|_{\pi} . \tag{3.3}$$

Hence, the limitation on the beam diameter is expressed by

$$D \le D_{max}^{M.Z.} = [\frac{|n_{eo}\, l|_{\pi}}{4\, n_{eo} \frac{x}{a} \sqrt{1 - (x/a)^2}}], \tag{3.4}$$

where $|n_{eo}\cdot l|_{\pi}$ is the chord density which gives a phase shift of $\pi$.

For the Michelson with flat mirrors, the beam diameter can be a half of the Mach-Zehnder type. As to the Michelson configuration with CCR, the maximum diameter is limited mainly by the second spatial derivative of the chord density because of the phase compensation effect of CCR:

$$[\frac{d^2}{dx^2} n_e(x)\, l]\cdot D^2 = -\, 4\, n_{eo} \frac{1}{a} \frac{1-2(x/a)^2}{\sqrt{1-(x/a)^2}} D^2 , \tag{3.5}$$

$$D \leq D_{max}^{CCR} = \left[ \frac{|n_{eo}|_{\pi}}{4\, n_{eo} \frac{1}{a} \frac{1-2(x/a)^2}{\sqrt{1-(x/a)^2}}} \right]^{-1/2} \qquad (3.6)$$

Note that the maximum beam diameter varies as $n_{eo}^{-1/2}$ for the Michelson configuration with CCR case, while it varies as $n_{eo}^{-1}$ for the other cases. The values of $D_{max}^{M.Z.}$ (solid curve) and $D_{max}^{CCR}$ (dashed curve) are shown in Fig. 3-5 for the case of $n_{eo} = 10^{20}\ m^{-3}$, $\lambda$ = 118.8 $\mu$m, and a = 0.93 m. Fig. 3-5

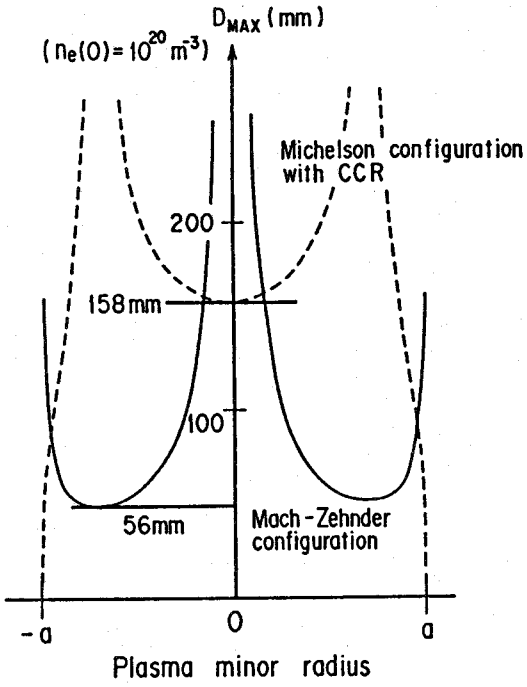


Fig. 3-5 Effective beam diameters calculated for the different types of interferometer configurations as a function of the radial position(r), assuming the parabolic electron density profile with the central electron density of 1 x $10^{20}\ m^{-3}$. (Solid lines are for the Mach-Zehnder configuration, and the dotted lines are for the Michelson configuration with a corner-cube

indicates that $D \leq 158$ mm for the Michelson configuration with CCR and $D \leq 56$ mm for the Mach-Zehnder configuration, provided that x is not close to $a$. These calculations show that the CCR configuration has following advantages over other two cases. Firstly, it allows the largest diameter, and secondly, the dependency of beam limitation on $n_{eo}$ is weaker than other two cases.

Although the designed beam diameter $d_{1/e^2}$ in the plasma is 56 mm, which is well below $D_{max}^{CCR}$, the interferometer signal occasionally diminished during the actual plasma discharge. It is due to the outward shift of the small minor radius plasma. According to the calculations above, the condition that the effective beam diameter equals the probing beam diameter is satisfied for the $R = 2.51$ m chord, when the minor radius and the amount of the outward shift of the plasma are 0.76 and 0.24 m respectively. The interferometer signal loss under this condition was confirmed employing the FBI code[5-8] which identifies the outermost magnetic flux surface with the magnetic probe data and poloidal coil current by the filament current method. The result of analysis is shown in Fig. 3-6. The evaluated minor radius and the horizontal displacement of the outermost magnetic flux surface are 0.77 and 0.20 m, which are in good agreement with calculated values. One of the primary reason that JET interferometer suffers frequent fringe loss can be attributed to this effect. Not only this effect induces the apparent errors seen as the interferometer signal loss, but also it reduces the fringe resolution by averaging the amount of phase shift along the beam diameter. Therefore the diameter of the aperture should be as small as possible so far as the reasonable signal to noise ratio is sustained even for the case when the probing beam is refracted because of the density gradient inside the propagating volume. In order to achieve 1/100 fringe resolution for the $R = 2.55$ m, 3.04 m and 3.55 m chords, the aperture diameter of 29 mm, 22 mm and 29 mm are required respectively with the S/N

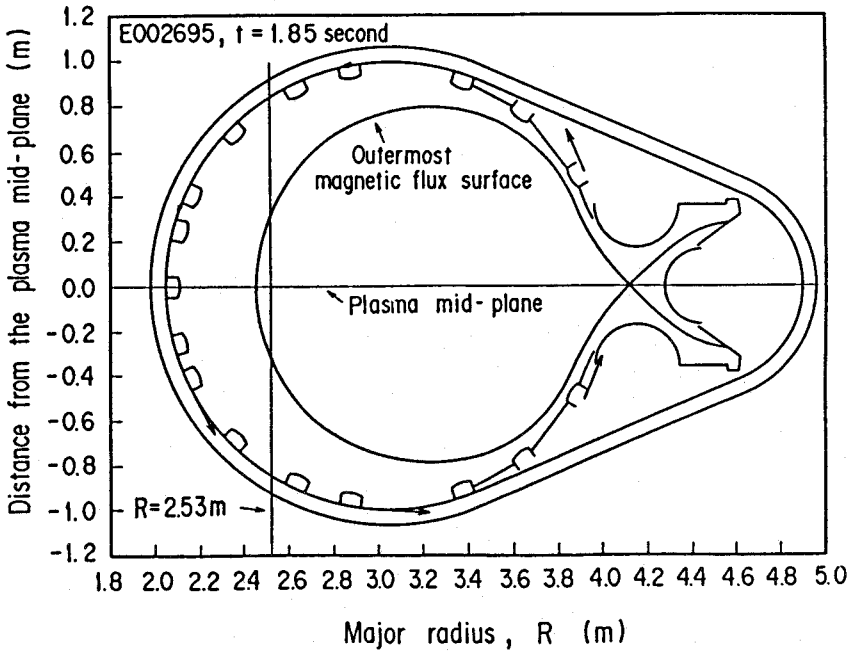


Fig. 3-6 The example of the position and the size of a plasma which satisfies the condition for the interferometer signal loss at R = 2.53 m chord due to the distortion of the wave-front.

ratio over 15.2 dB, supposing the stationary plasma of parabolic electron density profile.

The effectiveness of CCR configuration for large fusion devices was demonstrated in terms of not only the compensation of the bending of the ray trajectory and the diffusion of the beam power, but also the enlargement of the effective beam diameter by the phase compensation effect.

## 3. 3. 2. THE STABLE AND LOW-LOSS LONG DISTANCE PROPAGATION TECHNIQUE

The mutual displacement between the FIR lasers, interferometer optics, and CCRs induces severe deflection of the propagating beam axis, since these components are placed far apart. In order to minimize the deflection against

external vibrations, two types of approaches have been employed: (i) CCR configuration also in the reference beam optics for the beam mixing as shown in Fig. 3-7 and (ii) a flexible light-guide for the optical connection between the honeycomb bench and 40 m-long floor buried pipes. Owing to the CCR configuration in the reference branch, the probing and reference laser beam axes shift parallel into the same direction in the same plane to suppress the deterioration of visibility and the fluctuation of beam intensity at detectors. The flexible light-guide is consisted of two bend optics, two rotating tubes and a slide tube to provide six degrees of freedom as shown in Fig. 3-8(a). The structure of the bend optics assembly is depicted in Fig. 3-8(b), which exhibits that a flat mirror rotates according to the angle made by a rotating tube and a slide tube to hold the beam in the designed direction. The main material, except for the part where the ball bearings contact, was chosen to be aluminum, because the whole structure has to be light-weighted for the wide-band frequency response. The performance of the developed flexibile light guide has been investigated by

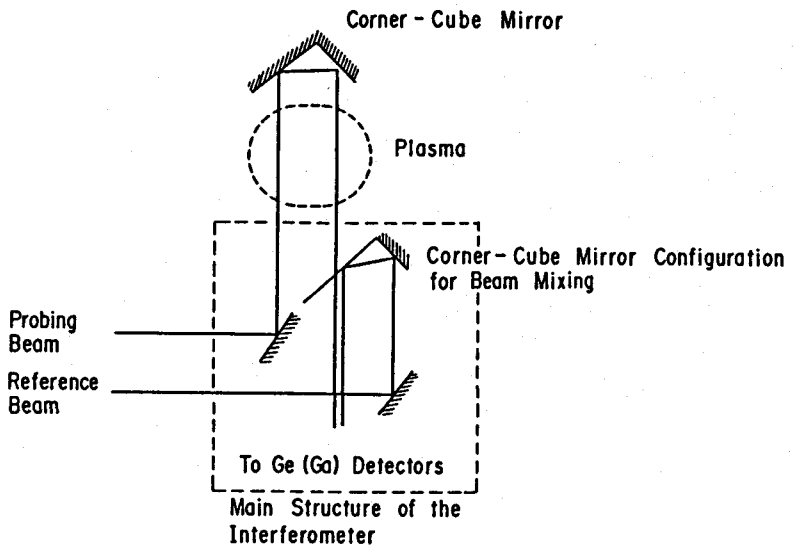


Fig. 3-7 Corner-cube configuration optics on both the probing and the reference branches for the stability of the interferometer signal.

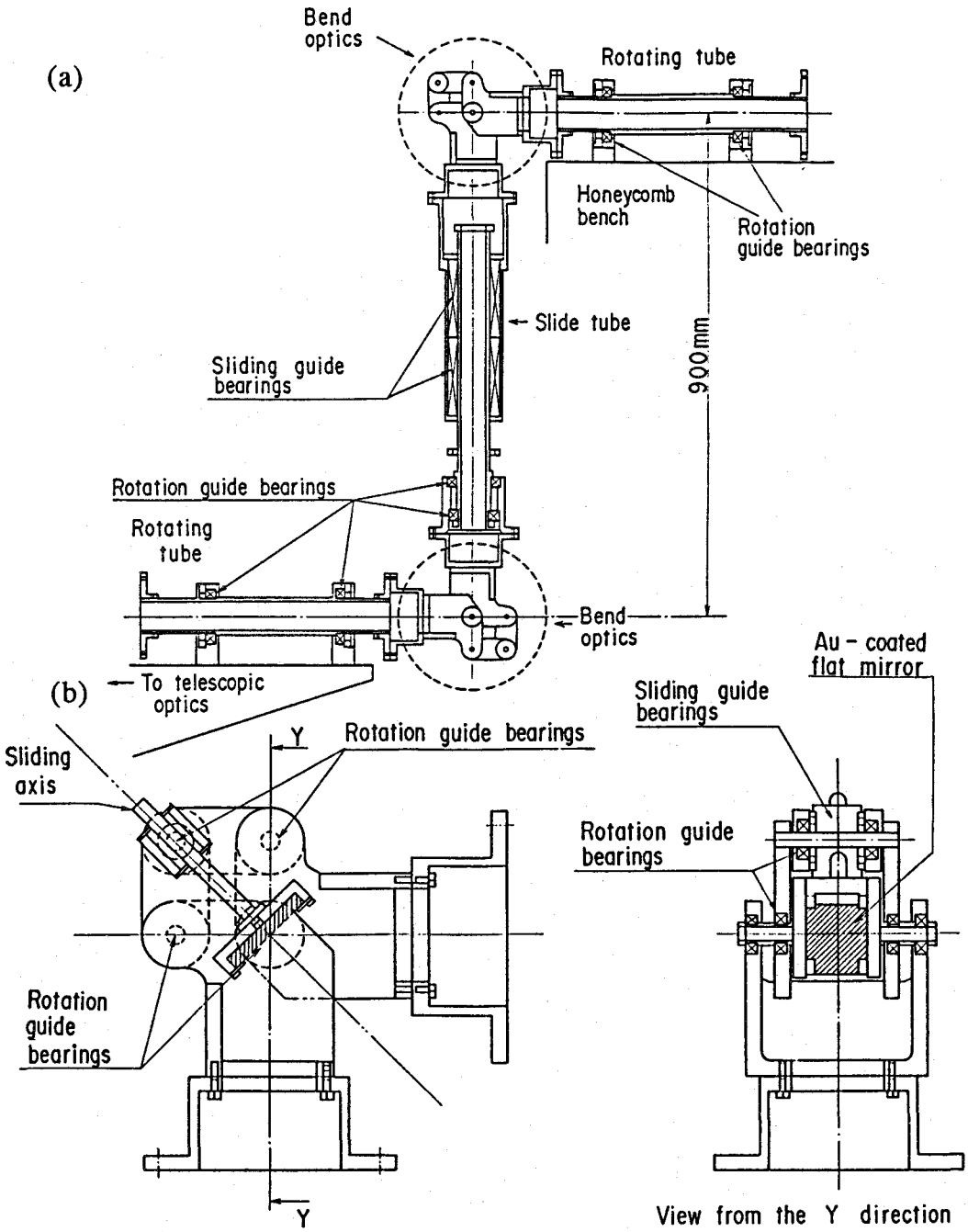


Fig. 3-8 (a) The structure of the flexible light-guide and (b) the description of the bend optics.

installing the upper rolling tube onto the vibration test stand. The visible He-Ne laser light was injected from the open end of the lower rotating tube through a beam splitter. The angle of deviation was measured by observing the laser light reflected by a flat mirror placed on the open end of the upper rotating tube. When a pitching motion along the propagation axis is induced with a 6 mm stroke and a frequency of 2 Hz, the ejected beam was deflected by 2.8 x $10^{-3}$ degree. As for a rowing motion with the same vibration condition, the deflection angle was 1.4 x $10^{-3}$ degree. These results are consistent with the values calculated by assuming the source of compensation errors to be manufacturing accuracy of ball bearings. From a survey of the deflection angle as a function of the induced acceleration, linear relationship was observed below 0.5 G, both for the pitching and rolling motion. The vibration

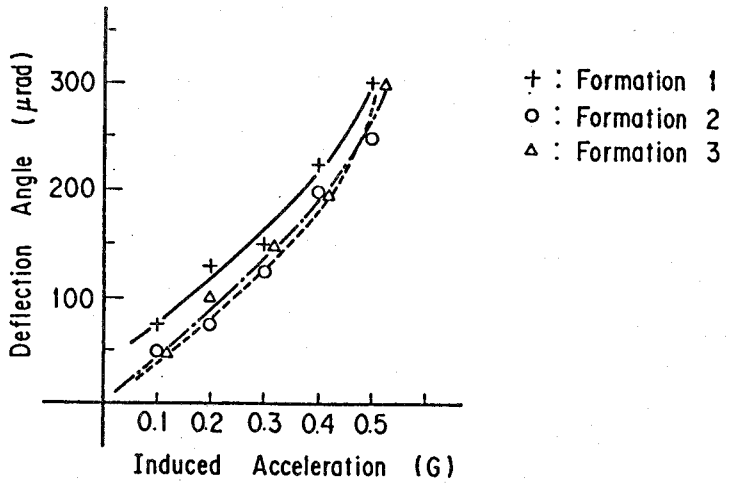


Fig. 3-9 Deflection angle of the ejecting beam axis from the flexible light-guide as a function of the induced acceleration. Formation 1 is a layout which propagating beam axes intersect perpendicularly in the same plane. Formation 2 is a layout which upper and lower rotating tubes are pulled apart 210 mm in the vertical plane, and the formation 3 is the case when the deformation like the formation 2 is done in the horizontal plane.

frequency was held at 5 Hz in this case. When larger acceleration over 0.5 G was induced in a pitching direction, the deflection angle increased non-linearly as shown in Fig. 3-9. The non-linear response indicates the elastic bending of the aluminum tube. Several formations of the flexible light guide have also been examined concerning the compensation efficiency, and it has been found that a formation which has no right angle bend is more stable against the external force.

The frequency response has been investigated with acceleration pickups. The measured resonant frequency of the developed flexible light guide was 70 Hz. When the vibration frequency was raised to 50 Hz with the induced acceleration of 0.5 G, the deflection angle exceeded $6.7 \times 10^{-2}$ degree. This value is close to the required maladjustment limit calculated from the ray tracing code and detector size. In the frequency domain over 200 Hz, on the other hand, the deflection angle was suppressed below $1.7 \times 10^{-2}$ degree. The vibration transfer characteristics have also been analyzed by Fourier-transforming the signals of acceleration pickups. The high-frequency component over 200 Hz is suppressed by 4 dB, while the decrease of the low frequency component was not clearly observed unless the lower rotating tube was rigidly fixed.

The rotation of the linear polarization is 0.076° for the rowing motion with a 1 mm stroke, and the elliptization of the polarization due to the reflection at the gold-coated flat mirror is also negligible for the Faraday rotation measusurement. The rowing stroke of the air-cushioned honeycomb bench has been actually measured to be much smaller than 1 mm during the plasma pulse even with a severe major disruption. The long term stability of the developed flexible light guide can possibly be degraded by the abrasion of ball bearings and their contact plane due to the repetitive forced friction. However, any rattling motion has not been observed so far in two years application on the JT-60 experiment.

The existence of vapor in the propagation volume disturbs the low-loss long distance transmission, and it literally limits the S/N ratio.[2-12] In order to evaluate the actual attenuation constant accurately as a function of the specific gravity of the humid air, the intensity of 118.8-μm CH3OH laser beam that passes through either dehydrated volume or humid air has been measured. For dehydration, the propagation volume inside a Pyrex tube has been filled with dry nitrogen gas, whose dew point is -60° C. The result has been compared with the case when the propagation volume was vacuum pumped below 71.4 Pa. The experimental setup is shown in Fig. 3-10. The attenuated beam intensity I, after the propagation of distance $L$ [m], can be written in the empirical formula:

$$I = I_0 \exp ( -12.3 \rho_s L ). \qquad (3.7)$$

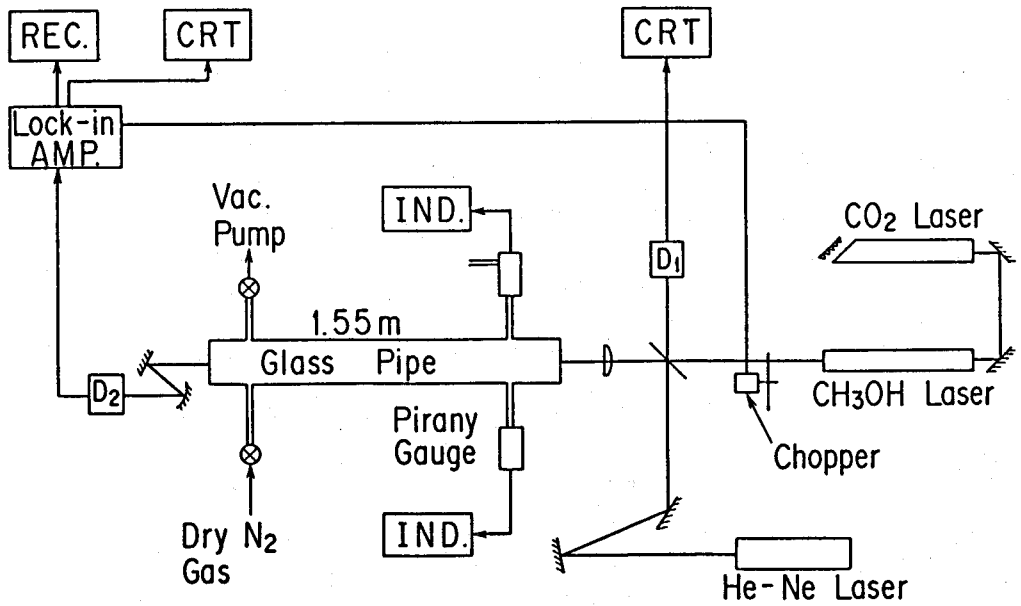


Fig. 3-10 The experimental setups for the evaluation of the attenuation index of the 118.8 μm laser beam power in accordance with the specific gravity of the humid air.

Here, $I_0$ is the initial intensity at the entrance of the Pyrex tube and $\rho_S$ is the specific gravity of the humid air expressed in $kg/m^3$ unit. The difference between the cases when the propagation volume was dehydrated or pumped was not observed. The obtained attenuation index was less than half of the value reported by Gallagher.[3-15] Gallagher has employed spectroscopically separated light as a source. Therefore the value claimed in this work can be assumed to be the first data obtained using a single mode coherent source. Based on the obtained value, the whole propagation volume was supplied with 0.12 $m^3$ dry air per minute, of which dew point is -62° C, and it was sealed with silicon made rubber putty. For the effective dehumidifying, the propagation volume has been separated into two parts with a mylar film. 20 hours after the dehydrating compressor is switched on, the humidity decreases to -45° C dew point, and the intensity attenuation is suppressed below 1 dB for the total propagation distance of 130 m.

## 3. 3. 3. DEVELOPMENT OF OPTICAL COMPONENTS

X-cut crystalline quartz made polarizing beam splitters have been developed in order to analyze the probing beam. Mylar films and free-standing wire grids are no more reliable for the118.8-μm radiation with a large beam diameter (typically $d_{1/e^2}$ = 75 mm), because vibrations caused by the micro-phonic effect and induced currents can introduce spurious signals, and wire grids inevitably suffers from the diffraction effect. Crystalline quartz is free from these obstacles, and it enables to control the splitting ratio at our disposal by the resonant effect,[3-16] even discriminating the polarization at the same time. The incident angle and thickness of the crystalline quartz can be easily calculated according to the Naylor's formula[2-7] and the Fresnel's formula. The splitting ratios have been determined so that the same portion of the beam intensities

are delivered to each diagnostic chords. As to the polarization beam splitter, calculated results are shown in Fig. 3-11(a) and (b). Fig. 3-11(a) shows the transmissivity and reflectivity of the s-polarized extraordinary wave and the p-polarized ordinary wave as a function of the thickness, while Fig. 3-11(b) is depicted as a function of the incident

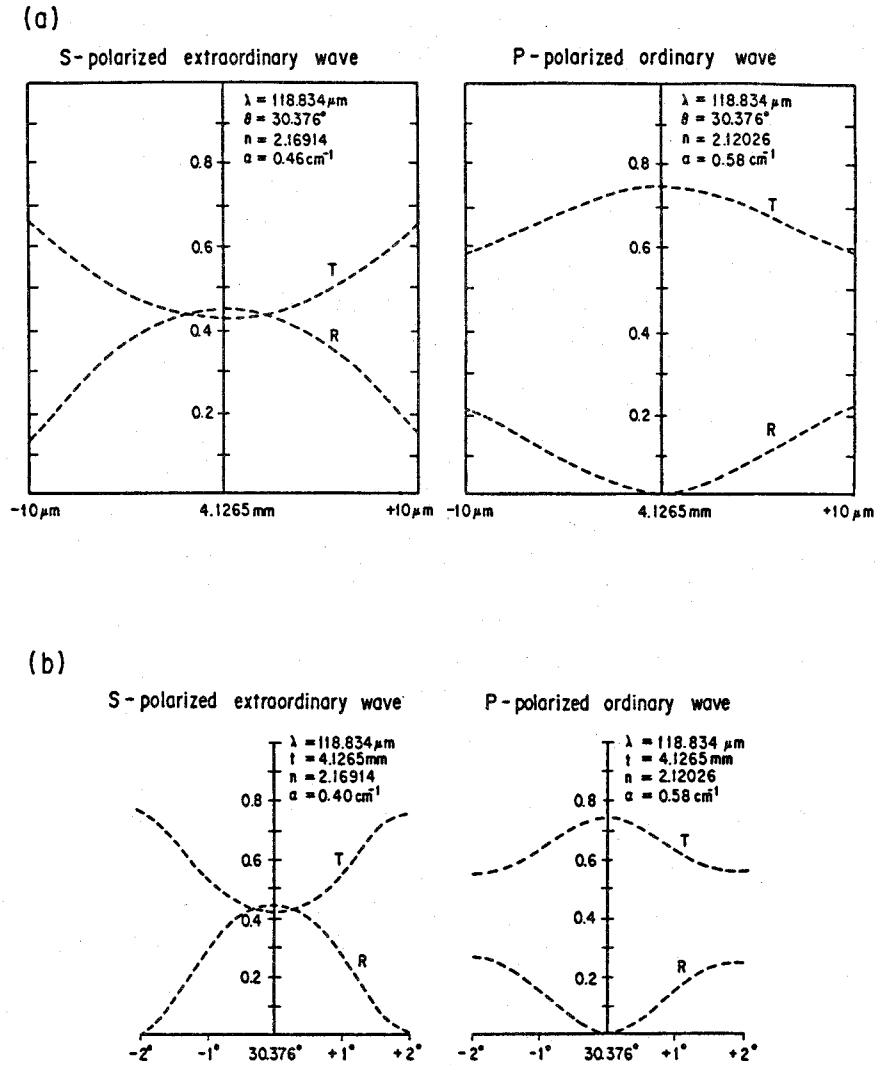


Fig. 3-11 The calculated transmissivity and the reflectivity of the polarizing beam splitter as a function of (a) the thickness of the plate and (b) the incident angle.

angle. The experimental evaluation of optical constants of the crystalline quartz has also been pursued to determine the thickness of etalon and the incident angle accurately. The obtained refractive index and the absorption coefficient for the ordinary wave were 2.12026 ± 0.00008 and (0.58 ± 0.02) $cm^{-1}$, and as for the extraordinary wave, they were 2.16914 ± 0.00010 and (0.46 ± 0.01) $cm^{-1}$ respectively. This result agrees well with the extrapolated value of the data reported by Russel and Bell.[3-17] Choosing the p-polarized ordinary wave as a transmission beam for the electron density measurement and s-polarized extraordinary wave as a reflecting beam for the Faraday rotation measurement, the optimum thickness and the incident angle have been calculated to be 4.1265 mm and 30.376° respectively.

Vacuum windows are also made of X-cut crystalline quartz, since there is no large size (155 mm in diameter) Z-cut crystal available. In order to simplify the results of Faraday rotation measurements, the thickness of windows have also been calculated to provide the equal transmissivity between the s-polarized extraordinary wave and p-polarized ordinary wave. Also, to reduce the stray reflections all windows were installed with a tilt of 3°.

The vacuum sealing technique of large diameter crystalline quartz windows is another item of development. The window seals are required to resist the repetitive high temperature baking. Rigid bonding method[3-18] is not reliable enough, since the difference of thermal expansion coefficient can introduce the cracking or exfoliation of the bonding materials. Furthermore, windows must be periodically removed to take off the graphite (the first wall material of JT-60) deposit. Therefore, we have developed a compound structure vacuum seal of which inner and outer shell are made of 304 stainless steel and silver, respectively. Silver has a good material compatibility with crystalline quartz. A coil spring was installed inside the inner shell to respond to the pressure variation. The developed window

seals have performed well under the vacuum tests with tens of repetitive heating cycles up to 250° C.

## 3. 3. 4. IMPROVEMENT OF ACCESSIBILITY BY THE MILLIMETER WAVE CIRCUIT INSIDE THE VACUUM VESSEL

The limitations of accessibility to plasmas is rigorous for the large fusion devices because of the complexed poloidal field coil configuration for the MHD equilibrium control and the radiation shielding, sacrificing the adequate spatial resolution of diagnostic equipments. Taking the advantages of the millimeter wave circuitry, we have installed a couple of 304-stainless steel made oversized waveguides and reflectors inside the JT-60 vacuum vessel. This method literally provides as many diagnostic chords as required. The viewing chord was situated on the edge plasma region, where there is no diagnostic port prepared. The structure of the oversized waveguide is shown in Fig. 3-12. The millimeter wave circuit inside the vacuum vessel is depicted in Fig. 3-13. The 2 mm wave is launched from a 65-mm-diameter horn-antenna into the 3.75-m-long Inconel-625 made diagnostic port, of which inner diameter were designed to be 70 mm, for the waveguide transmission. The injected wave is received by a 20-mm-diameter transducer attached to the oversized waveguide. The propagating beam, after being mode-filtered and circular-rectangular converted inside the oversized waveguide, reaches the rectangular (20 mm x 16 mm) horn-antenna equipped with a reflector. The reflector angle was determined so that the refracted wave is directed to the receiving horn-antenna, considering the density gradient produced by a full size plasma with the central electron density of $1 \times 10^{20}\ m^{-3}$ and a parabolic distribution. Therefore, from the radiation pattern of the rectangular horn-antenna depicted in Fig. 3-14, the detection level

increases by 5 dB with a production of such a plasma. All the components inside the JT-60 vacuum vessel were installed behind the graphite limiter tiles. The reflected wave at the lower reflector is transmitted to the upper reflector through a narrow gap of limiter tiles. Thus, this diagnostic configuration preserves the boundary condition for the edge plasma property measurement.

The insertion loss of the oversized waveguide excluding the rectangular horn-antenna and the transducer was 3.9 dB. The antenna gain of the rectangular horn-antenna including the reflector was 27.1 dB. The 120-mm-diameter reflection plate attached to the oversized waveguide and the 25-mm-diameter iris installed at the connection part of the diagnostic port with the vacuum

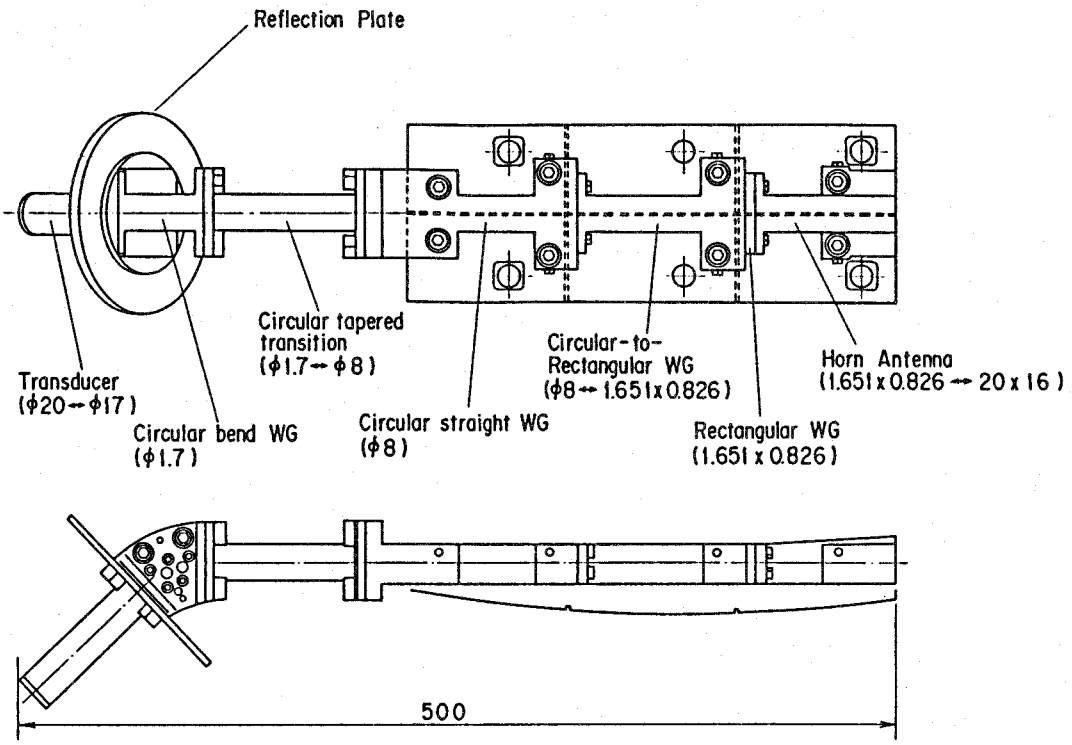


Fig. 3-12 The structure of the oversized waveguide installed inside the JT-60 vacuum vessel.

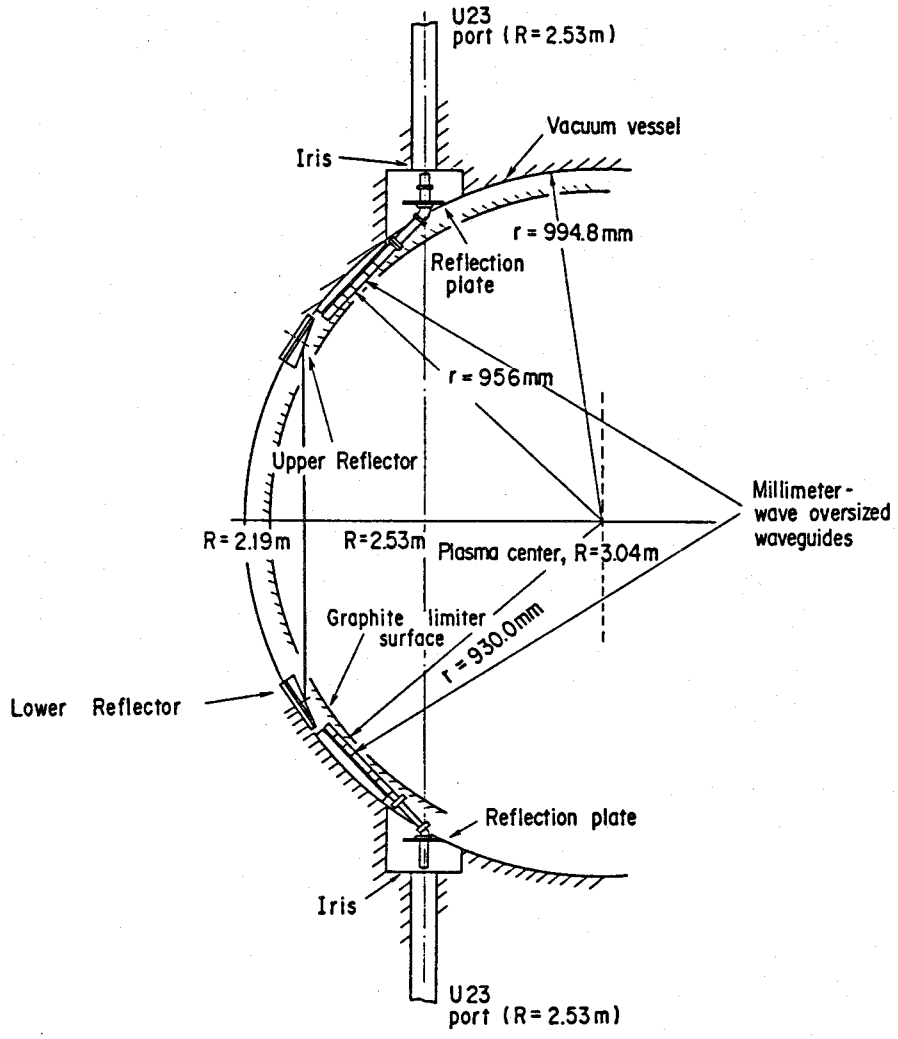


Fig. 3-13 The millimeter wave circuitry inside the JT-60 vacuum vessel.

vessel works to suppress the port-to-port millimeter wave leakage to 45.2 dB below the signal detection level. The adjustment of the launching horn-antennae were very sensitive to their relative position with the diagnostic ports which work as waveguides. The insertion loss of the diagnostic port was 13.5 dB and the detection level was – 64 dBm without a plasma to yield the S/N ratio of 7 dB. The noise level is actually determined by the fringe counting

circuit. Although the ohmic loss is not small because of the lengthy and complicated circuit inside the vacuum vessel, no large amplitude ripple was observed at the frequencies from 135 GHz to 137 GHz, which indicates the absence of the impedance mismatch and the low mode conversion.

## 3. 4. EXPERIMENT AND DATA EVALUATION

The major and minor radius of the JT-60 tokamak are 3.04 m and 0.93 m respectively, and the maximum plasma current and the toroidal magnetic field so far achieved were 3.2 MA and 4.8 T. The temporal evolution of the electron density in the main plasma region with the real-time feedback control is shown in Fig. 3-15. The S/N ratios,

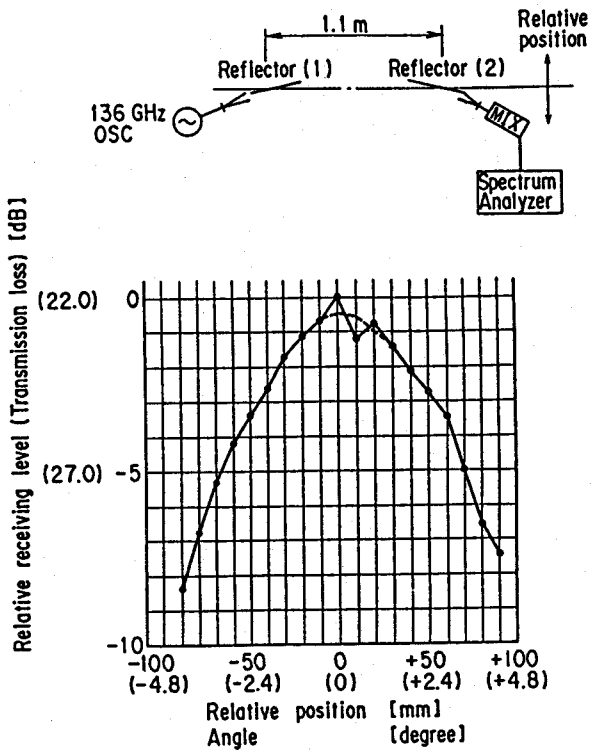


Fig. 3-14 The radiation pattern of the 20 mm x 16 mm horn antenna with a reflector.

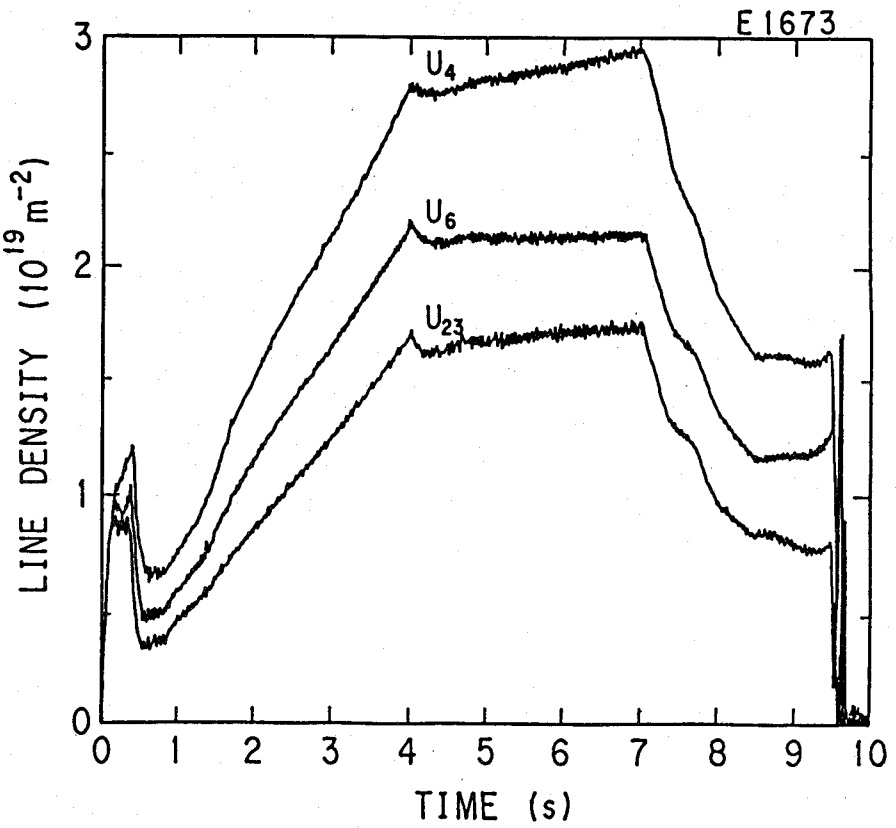


Fig. 3-15 Temporal evolution of the real-time feed back controlled electron density in the JT-60 tokamak. ( Major radius, R = 3.04 m and the minor radius, a = 0.93 m. $U_{23}$, $U_4$ and $U_6$ are the interferometer chords at R = 2.53 m, 3.04 m and 3.55 m respectively. The real-time electron density feed back control is applied from 4 to 7 seconds. )

visibilities and the degrees of linear polarization at the injection side of the vacuum window were 22~25 dB, 22~35 % and more than 99% respectively for the submillimeter interferometer, and the fringe resolution was confirmed to be 1/100. The resolution of the Faraday rotation angle was 0.25° against the maximum expected rotation angle of 19°. As for the 2 millimeter interferometer the S/N ratio at the R = 3.25 m chord and the fringe resolution were 38 dB and 1/30. The degradation of the fringe resolution is due to the

vibration of the diagnostic platform of 70 μm, where the receiving horn antenna is installed. Time resolution of 200 kHz throughout the plasma pulse duration period of 10 seconds has enabled the precise analysis of the MHD activities.

Absolutely no evidence of the intrusion of the radio-frequency noise from the plasma heating Klystrons and the stray magnetic field was observed even for the plasma discharge with the lower-hybrid wave heating power of over 10 MW combined with the neutral beam heating power of over 20 MW. The electron density profile was evaluated by an equilibrium calculation combined with the results of the Faraday rotation angle measurement and the magnetic probe measurement data. Detailed description of the analysis procedure is given in chapter 5. The obtained electron density profile and the profile measured by Thomson scattering agree within the accuracy of 10% as depicted in Fig. 3-16.

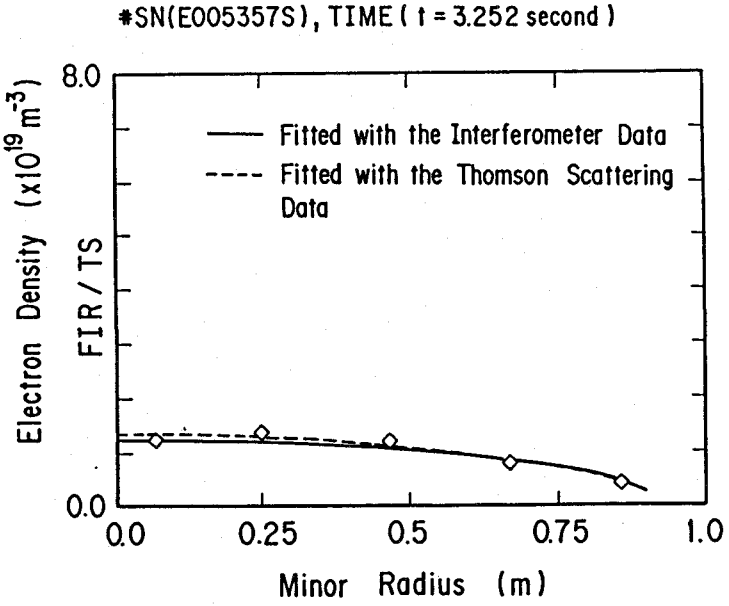


Fig. 3-16 Electron density profile fitted with the interferometric measurement data combined with the equilibrium calculation in comparison with the profile fitted by the result of the Thomson scattering measurement.

The edge plasma density measurement with the boundary condition preserving millimeter waveguides inside the vacuum vessel has brought precious informations on the edge plasma properties. Edge plasma density data when the lower-hybrid electron heating was applied is shown in Fig. 3-17. The sharp increase of the line electron density at the onset of the RF-pulse is due to the injection of light impurities from the graphite limiter. Spectroscopic measurement of the carbon and oxygen lines shows the intensity spikes at the same incidence. The propagation of the density pulse towards the plasma center was observed. The inclusion of the edge plasma density data in the electron density profile evaluation procedure substantially improves the accuracy of determining the profile parameter M in (5.4), but it has little effect on the evaluated results of the total stored energy. The profile parameter M is 1.1 for the limiter plasma configuration, and it is 0.2 for the divertor

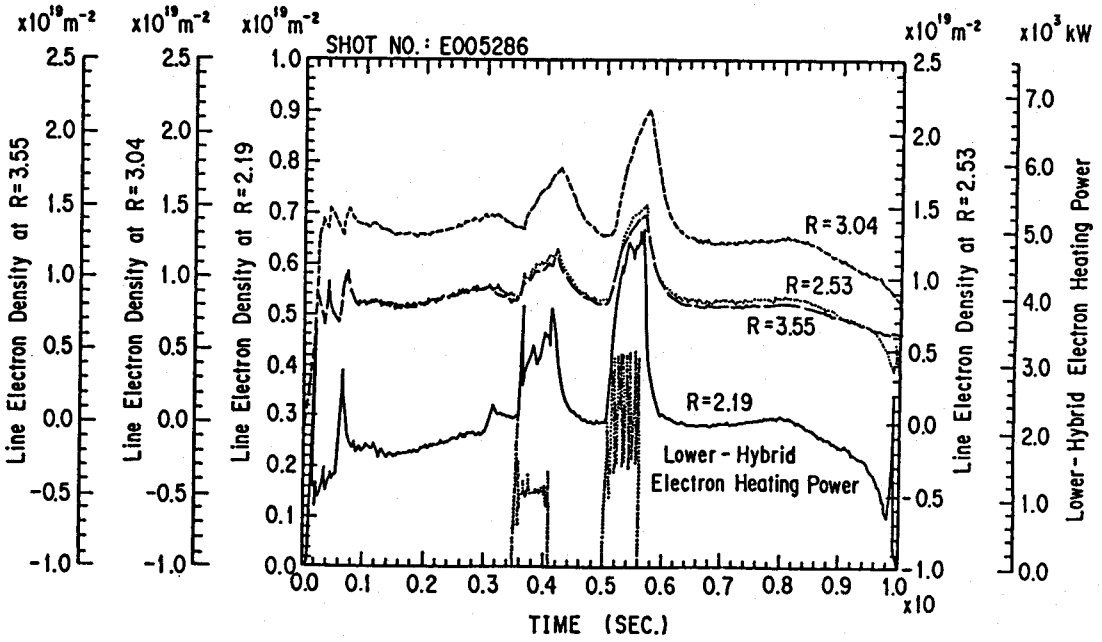


Fig. 3-17 Edge plasma density evolution for a lower-hybrid electron heating applied plasma, shown with the submillimeter interferometer data at R = 2.53, 3.04, and 3.55 m chords.

plasma configuration. Therefore the density gradient at the edge plasma region is steeper for the divertor plasma configuration to result in the deterioration of the signal detection level by the refraction effect.

As for the electron density measurement in the divertor region, it has been found that the divertor plasma density varies sensitively as a function of the width of the divertor throat gap $\delta_t$. The successful interferometric measurement owes to the stabilization of the propagating laser beam axis by the employment of CCR configurations on both of the probing and the reference optics as well as the enlargement of the He-Ne laser beam diameter(30 mm$^{\phi}$) and the APD detector size (5 mm$^{\phi}$). The amount of phase shift caused by the external vibration is more than twenty times larger than the phase shift experienced by the plasma. The detailed result of the divertor plasma density measurement is described in chapter 4.

## 3.5 CONCLUSION

Development of the JT-60 interferometer system was reviewed in this chapter to demonstrate their feasibility. Firstly, required items to develop polari-interferometer system feasible enough for the large tokamak applications were addressed.

In order to cope with the distortion of the wave-front due to the electron density gradient inside the propagating beam volume, the most appropriate interferometer configuration and the effective beam diameter have been evaluated. Michelson configuration with corner-cube reflectors combined with the aperture of 22 mm$^{\phi}$ diameter revealed its effectiveness for the 1/100 fringe resolution.

Owing to the stabilization of the propagating beam axis by the newly developed flexible light-guide and preservation of visibility with the adaption of the corner-cube configuration also on the reference branch, diminution of the signal detection level due to the mechanical vibration

was not observed even for the severe plasma disruptions. The experimental evaluation of the attenuation index of the 118.8-μm coherent radiation yielded appropriate dehydrating design for the retention of the desirable S/N ratio.

Furthermore, the development of the optical components for the polarimetric measurement and the optimum laser power distribution were found to be indispensable for the large tokamak interferometry. The developed components including the repetitively bakable modified Helico-flex vacuum sealing proved their effectiveness and reliability under the huge stray magnetic field and mechanical vibrations.

The method employed for the edge plasma density measurement fundamentally preserves the boundary conditions of the interacting edge plasma with the first wall, and it is encouraging for the future fusion experiment devices of which diagnostic accessibility is severely limited. The installation of a millimeter wave circuit inside the vacuum vessel literally enables as many diagnostic chords as required. The edge plasma density measurement yielded precious informations as to the plasma surface interactions and edge plasma localized phenomena.

The first interferometric measurement of the divertor plasma was realized by the application of the corner-cube reflector configuration with the quadruplicated laser beam path for the stabilization of the propagating laser beam axis. Stability of the vibration compensating He-Ne laser beam is essential when a reflector is installed inside the vacuum vessel. The enlargement of the He-Ne laser beam diameter and the choice of large APD detector contributed much for the stability of the detection level against the huge amplitude external vibrations. A molybdenum metallic reflector has been chosen to retain the reflectivity against the erosion and sputtering by the heat flux and particle bombardment from the plasma.

The whole interferometer system has been routinely in operation reliably for two years without any

readjustment or attendant complications. The operation status is remotely controlled and monitored. Timing signal and the programmed communication network with the JT-60 central control system supervise the whole interferometer system. Therefore no operator for the interferometer system is required.

In the course of 2 years tentative operation, the developed polari-interferometer system has pronounced the establishment of the fundamental methodology related to the large tokamak interferometry. So far as the instrumentation of the future fusion devices is concerned, however, interferometric measurent presumably should undergo another stage of development. The development of the JT-60 polari-interferometer system was essentially an integration or an expansion of the existing methods. One of the requirements imposed on the application to the engineering fusion test devices is further research on the vibration compensation technique. Degradation of optical properties of molybdenum metallic mirrors inside the vacuum vessel and the deposition of the graphite granule on the vacuum windows have actually lead to the gradual reduction of the 0.63-μm-He-Ne laser interferometer signal intensity. In order to retain the long-term reliabiliity, the use of FIR sources both for the plasma phase-shift measurement and the vibration compensation is necessary. Several preliminary studies on the two-color FIR laser interferometry are being pursued in advance for JET[3-7] and CIT.[3-19,20] Another item of requirements is the development of solid-state FIR sources. The FIR laser system is still large and complicated, and damaged components due to the secular degradation have to be found and replaced in the years of operation. A solid-state FIR laser source can be installed close to the tokamak, according to the specific viewing chord, and it yields convenient replacement. FIR lasing based on hot hole transitions in Ge(Ga) has been successfully achieved by Andoronov in 1984,[3-21] and its lasing characteristics are intensively studied. The Ge(Ga) hot

carrier laser can potetially lase continuously in a wavelength range of 60 – 500 μm. The whole interferometer system could possibly be build in a disposable unit on the engineering fusion test devices, although it depends on the stability and gain performance of the Ge(Ga) hot carrier laser.

## REFERENCES TO CHAPTER 3


3-1 T. Fukuda and A. Nagashima, Rev. Sci. Instrum. **60-6**(1989).

3-2 S. M. Wolfe, K. J. Button, J. Waldman, and D. R. Cohn, Appl. Opt. **15**, 2645(1976).

3-3 T. Fukuda, H. Yoshida, A. Nagashima, S. Ishida, M. Kikuchi, and H. Yokomizo, J. Nucl. Mater. **162-164**, 258(1989).

3-4 D. Véron, Infrared and Millimeter Waves, edited by K. J. Button(Academic Press, New York, 1979), Vol.2.

3-5 D. R. Baker, Rev. Sci. Instrum. **10**, 51(1980).

3-6 D. K. Mansfield, H. K. Park, L. C. Johnson, H. M. Anderson, R. Chouinard, V. S. Foote, C. H. Ma, and B. J. Clifton, Appl. Opt. **26**, 4469(1987).

3-7 G. Magyar and J. O'Rourke, Proc. Varenna Workshop, EUR-10797-EN, Vol. II, 409(1986).

3-8 F. De Marco and S. E. Segre, Plasma Physics **14**, 245(1972).

3-9 A. D. Craig, Plasma Physics **18**, 777(1976).

3-10 H. Soltwisch, Nucl. Fusion **23**, 1681(1983).

3-11 A. Nagashima, Proc. 9 th International Conference on Infrared and Millimeter Waves, Takarazuka, 264(1984).

3-12 B. Lipschultz, J. Nucl. Mater. **145**, 15(1987).

3-13 P. Brossier and R. A. Blanken, IEEE Trans. Microwave Theory and Tech. **MTT-22**, 1053(1974).

3-14 J. Shmoys, J. Appl. Phys. **32**, 689(1961).

3-15 J. J. Gallagher, M. D. Blue, B. Bean, and S. Perkowitz, Infrared Physics **17**, 43(1977).

3-16 A. Nishizawa, Proc. 6th International Conference on Infrared and Millimeter Waves, Miami, M-3-9(1981).

3-17 E. E. Russel and E. E. Bell, J. Opt. Soc. Am. **57**, 341(1967).

3-18 P. Millward, A. Ainsworth, C. J. Caldwell-Nichols, R. Lobel, and C. J. Hancock, Fusion Tech. **11**, 242(1982).

3-19 C. H. Ma, D. P. Hutchinson, and K. L. Vander Sluis, Rev. Sci. Instrum. **59**, 1629(1988).

3-20 T. Lehecka, W. A. Peebles, N. C. Luhmann, Jr., and T. N. Carlstrom, Rev. Sci. Instrum. **59**, 1580(1988).

3-21 A. A. Andronov, I. V. Zverev, V. A. Kozlov, S. A. Pavlov, and V. N. Shastin, ZhETE **40**, 69(1984).

# CHAPTER 4. INTERFEROMETRIC DENSITY MEASUREMENTS IN THE DIVERTOR AND EDGE PLASMA REGIONS FOR THE ADDITIONALLY HEATED JT-60 PLASMAS

The first divertor plasma density measurement and the interferometric edge plasma density measurement with boundary condition preserving millimeter waveguides were demonstrated to elucidate the mutual correlation among the divertor plasma, scrape-off layer plasma and the bulk plasma properties in the additionally heated JT-60 plasmas. The electron density in the divertor region exhibited a non-linear dependence on the bulk plasma density for the ohmically heated plasmas. When neutral beam heating is applied on the plasmas with the electron density above 2 x $10^{19}$ $m^{-3}$, however, the bulk plasma density is scraped off from the outer region to lead to density clamping, and the electron density in the divertor region rapidly increases over 1 x $10^{20}$ $m^{-3}$, which infers that the particle flow along the magnetic field is dominant, resulting in the apparent degradation of the particle confinement time. As for the case when neutral beam injection is applied to low-density plasmas, the bulk plasma electron density profile becomes flattened to yield a smaller density increase in the divertor region and no density clamping of the bulk plasma was observed. Simulation analysis which correlates the transport of the divertor plasma and the scrape-off layer plasma was also carried out to find the consistency with the experimental results.

## 4. 1. INTRODUCTION

Although the effectiveness of the divertor configuration is persuasively recognized for the improvement of the energy confinement and the suppression of the plasma-wall interactions,[4-1,2,3] divertor

and edge plasma parameters have been scarcely diagnosed. The particle transport mechanism has been evaluated by means of interferometric measurements on JT-60 plasmas which have a single null closed divertor horizontally outside the midplane. A phase-modulated 118.8-μm alcohol laser interferometer[4-4] and a 2 mm super-heterodyne interferometer equipped with a pair of over-sized waveguides installed on the inner surface of the JT-60 vacuum vessel[4-5] were prepared. Simulation analysis has been carried out with a tokamak transport code combined with a divertor fluid model[4-6] which correlates the particle flux and the heat flux of the scrape-off layer plasma and the divertor plasma at the divertor throat entrance.

## 4. 2. EXPERIMENT

The diagnostic layout is shown in Fig. 3-3. The alcohol laser beams together with the He-Ne laser beams for the vibration compensation are injected from the upper and the lower inclined diagnostic ports to be reflected by molybdenum-bulk mirrors placed in the shadow of the divertor plates, which have a 45 mm width gap for the beam transmission. Reflected beams are directed to corner-cube mirrors at the far ends of the diagnostic ports for the compensation of the beam axis displacement due to the mechanical vibration that can be caused by the plasma discharge. Scene beams, after another reflection at the molybdenum-bulk mirrors, return to the interferometer optics to yield the bundle-beam size of ±30 mm from the intersection point of the magnetic field lines and the divertor plates. As for the 2 mm wave interferometer circuit ($R$ = 2.19 m) a pair of over-sized waveguides and reflectors are installed between the 200 mm gap of the graphite tiles on the inner surface of JT-60 so that the boundary condition for the plasma-wall interaction can be preserved. The reflection angle of the transmitting-side lower reflector is decreased to direct the millimeter-wave

away from the torus center. The reflection angle was determined so as to let the full size plasma of the central electron density of 1 x $10^{20}$ $m^{-3}$ with the parabolic density profile refract the beam into the appropriate position. The electron density profile was evaluated by identifying the outermost and the inner magnetic flux surfaces with the result of the Faraday rotation angle measurement and the magnetic probe data combined with an equilibrium calculation. The line electron density data is expanded on the magnetic flux surfaces, supposing that the equi-density surfaces coincide with the magnetic flux surfaces.

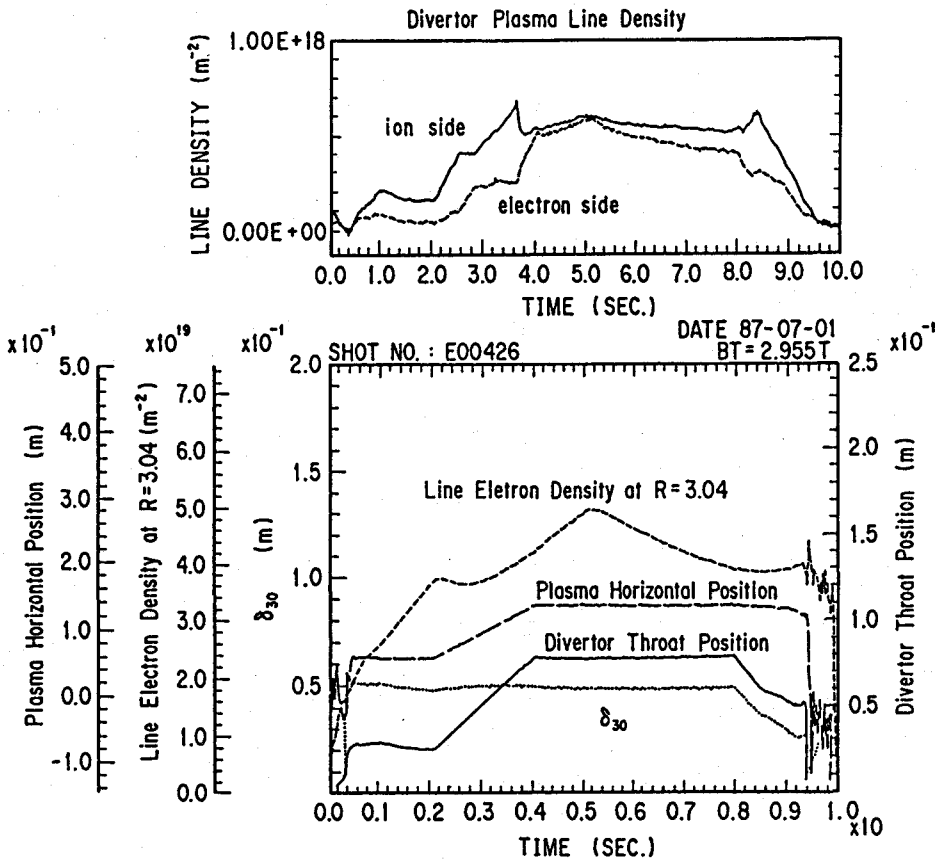


Fig. 4-1 Temporal behavior of the divertor plasma density for the ohmically heated plasmas.

As for the ohmically heated plasmas the divertor plasma density varies sensitively as a function of the width of the divertor throat gap $\delta_t$ as shown in Fig. 4-1. Here, $\delta_{30}$ is the distance between the toroidal limiter and the plasma surface at the 30° limiter position. The larger $\delta t$ means a reduced particle flow back into the scrape-off layer from the divertor region, and it results in a higher electron density in the divertor region. The nonlinear dependence of the divertor plasma density on the bulk plasma density was exhibited as depicted in Fig. 4-2, which is consistent with the result of the simulation analysis shown by the dotted line[4-7] on the assumption that $\chi e$ =5 x $10^{19}$/ne [$m^2$/s], $D$

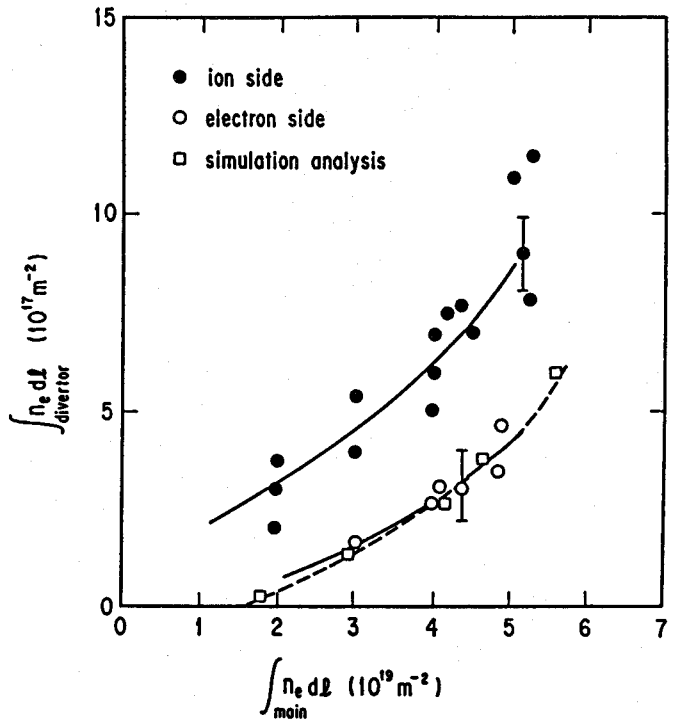


Fig. 4-2 Dependence of the divertor plasma density on the ohmically heated bulk-plasma density. (Open and closed circles are for the electron and the ion side respectively and the open squares are the results of the simulation analysis.)

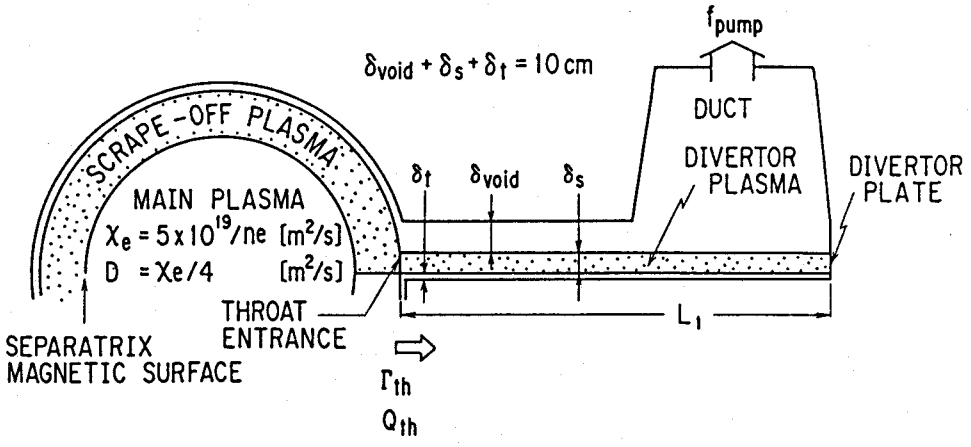


Fig. 4-3 The model geometry for the simulation analysis.
Parameters used in the simulation : distance between the divertor throat and plate $L_1$ = 60 cm, width of divertor scrape-off layer plasma $\delta_s$=3 cm, width of vacuum area $\delta_{void}$ = 2.5 cm and the effective pumping rate $f_{pump}$ = 0.2.

$=\chi e$ /4.0 [m²/s] in the bulk plasma and the pumping efficiency of 0.2.

The simulation model employed here is consisted of the tokamak transport code combined with a divertor fluid model, which solves the transport of the scrape-off layer plasma and the divertor plasma consistently. The model geometry for the simulation analysis is illustrated in Fig. 4-3 together with the divertor plasma model of width $\delta s$ and length $L_1$, which is projected onto the poloidal plane. The effective pumping rate of particles $f_{pump}$ includes the bypass component to the main chamber through the duct, wall absorption and the exhaust from the divertor chamber. The modelling is based on: (1) one-dimensional fluid equations for particle, momentum and energy transport of the divertor plasma along the magnetic field lines, and (2) a two-dimensional Monte Carlo method for the particle, momentum and energy sources due to ionization and charge exchange reactions of neutral particles. In this model, only

hydrogen atoms are treated in the Monte Carlo calculation, and only hydrogen line radiation estimated by a collisional-radiative model is assumed as a source of radiation loss from the divertor plasma. Two boundary conditions are assumed in this simulation model: one is the particle flux $\Gamma_{th}$ and the heat flux $Q_{th}$ given at the divertor throat entrance. These parameters are obtained by the application of the tokamak transport code for the bulk plasma supposing the appropriate diffusion coefficient and the thermal conductivity. The other is the assumtion on the divertor plasma parameters. The sheath condition has been employed for the estimate of heat flux, and the Bohm condition in front of the divertor plate are assumed for the evaluation of flow velocity, utilizing the established fluid model.[4-8]

In the ion side more than twice as great an electron density was observed in comparison with the electron side, which shows better agreement with the result of the simulation analysis. Electrons from the impurity atoms produced when hydrogen ions strike the divertor plate can possibly cause the discrepancy with the simulation result which does not distinguish between electron side and the ion side.

When neutral beam heating is applied on plasmas of density above 2 x $10^{19}$ $m^{-3}$, the bulk plasma density profile becomes peaked in the transient phase as it is scraped off from the outer region as shown in Fig. 4-4, and the divertor plasma density soars up to around 1 x $10^{20}$ $m^{-3}$ (Fig. 4-5). The width of the divertor plasma layer $\delta s$ was estimated to be about 30 mm following the DIVA scaling.[4-9] The peaking of the electron density profile can also be observed in the temporal evolution of the line electron density as depicted in Fig. 4-6. The amount of increase for the central ($R$ = 3.04 m) line electron density becomes larger compared with that

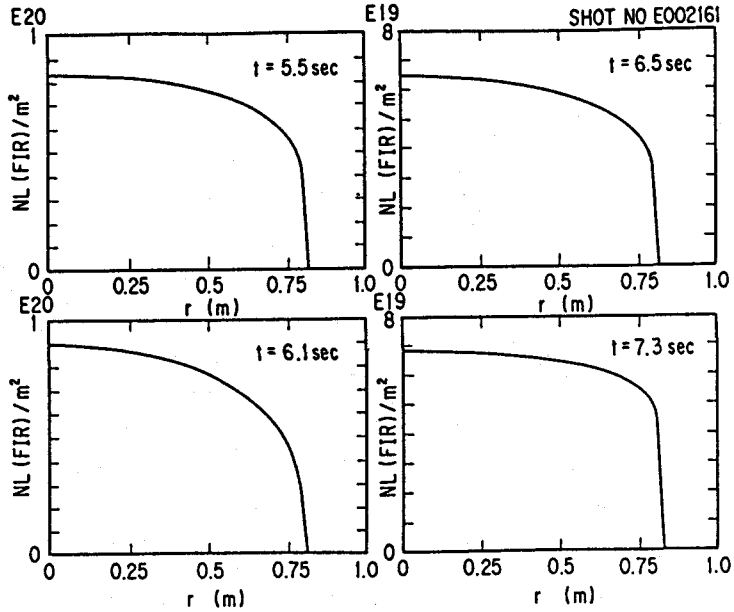


Fig. 4-4 Temporal evolution of the bulk plasma density profile (Neutral beam was injected from 6 to 7 seconds).

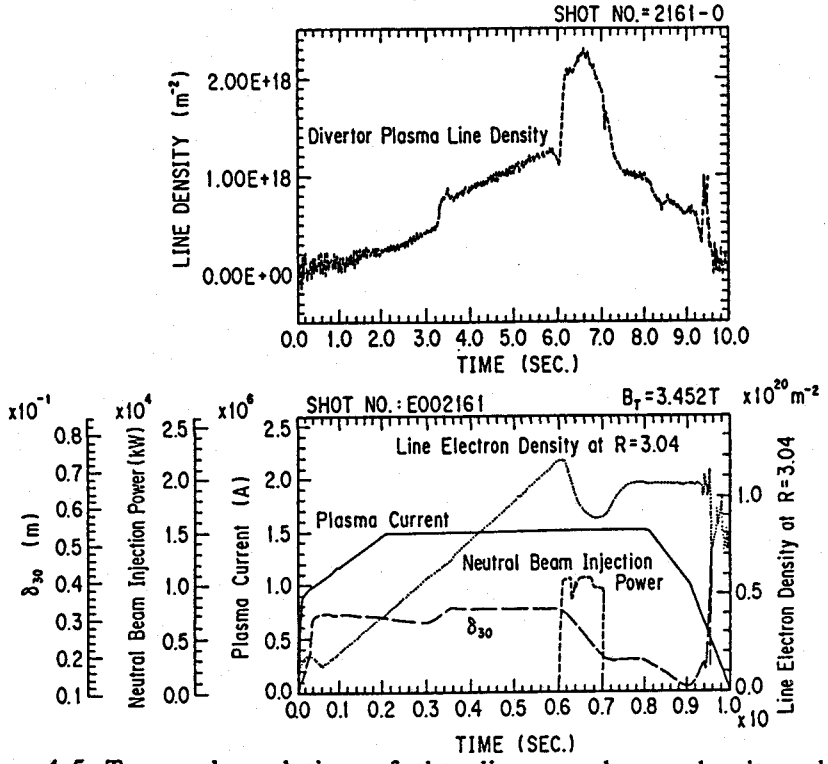


Fig. 4-5 Temporal evolution of the divertor plasma density when the neutral beam was injected into the high density plasma.

of the edge plasma ($R$ = 2.19 m) during the neutral beam injection. It was shown from the spectroscopic measurement that during the neutral beam heating a large number of light atoms are injected into the plasma from the graphite wall. Together with the number of electrons removed from the scrape-off layer, a great number of electrons are assumed to be carried into the divertor region. Apparent degradation of the particle confinement was observed in this case from the $H_\alpha$ emission measurement. This infers that the particle flow along the field lines in the scrape-off layer has increased. As seen in Fig. 4-4, after the transient phase, the electron density profile recovers to be flattened, and the particle confinement time increases, although it is one third of that during the ohmic heating. For the particular operation when the intersection point of the magnetic field line and the divertor plates was swung during the neutral beam injection, the larger degradation of

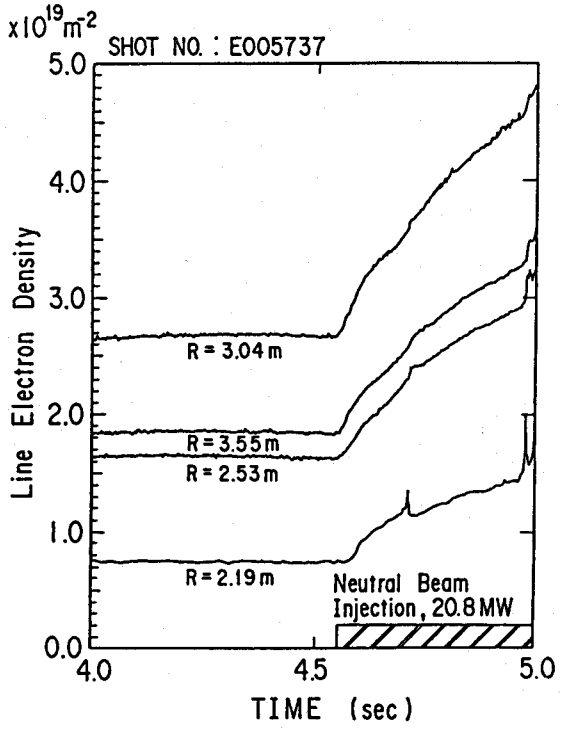


Fig. 4-6 Temporal evolution of the line electron density for the neutral beam heated plasmas.

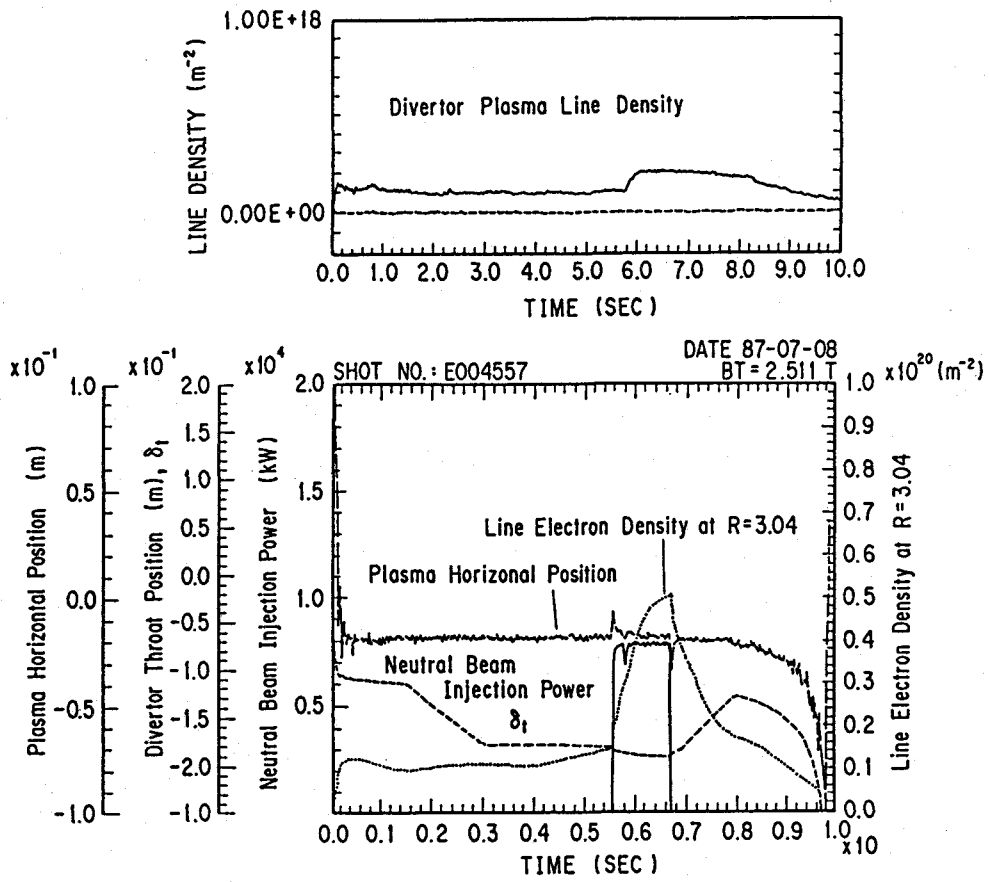


Fig. 4-7 Temporal evolution of the divertor plasma density when the neutral beam was injected into the low density plasma.

the particle confinement time and the smaller recycling rate were observed from the $H_\alpha$ measurement, although it is one third of that during the ohmic heating. In the case when the neutral beam was injected into low-density (below 2 x $10^{19}$ $m^{-3}$) plasmas, no density clamping and less increase of the divertor plasma density was observed as shown in Fig. 4-7. In this case, degradation of the particle confinement time measured by the $H_\alpha$ measurement was not observed. It has been found that in the density range below 2 x $10^{19}$ $m^{-3}$, the

electron density profile is peaked compared with the high-density plasmas, and the electron density in the scrape-off layer is scarce, which brings fewer electrons along the magnetic field into the divertor region. Contrary to the high-density case, the electron density profile becomes to some extent flattened during the increasing phase of the electron density by the additional heating. The particle source is supposed to be the influx of light atoms from the graphite wall.

## 4. 3. CONCLUSION

The temporal evolution of the electron density in the divertor and the inner edge plasma region was directly diagnosed for the first time with an alcohol laser interferometer and a 2 mm interferometer equipped with boundary condition preserving waveguides inside the JT-60 vacuum vessel. The simulation analysis which characterizes the divertor plasma parameters by correlating the transport of the divertor plasma and the scrape-off layer plasma has also been carried out. Although the result of the simulation analysis depends on several free parameters such as the effective pumping rate, distance between the divertor throat and plate, $\chi e$ and $D$ , the reasonable parameters which can yield consistency with the obtained experimental results have been found.

For the ohmically heated plasmas, the electron density in the divertor region showed a nonlinear dependence on the bulk plasma density. When the neutral beam was injected into the medium- to high-density plasmas which have a flattened electron density profile, the electron density was scraped off from the outer region, and the electrons were carried into the divertor region along the magnetic field to result in the apparent degradation of the particle confinement time. The increase of the particle flow along the magnetic field lines can therefore be reduced to be one of the dominant term which induces the density clamping of the bulk plasma in JT-60. When the neutral beam is

injected into the low-density plasmas which has a rather peaked density profile, on the contrary, fewer electrons are carried into the divertor region, since fewer electrons exist in the outer region of the plasmas. In this case no density clamping and degradation of the particle confinement time was observed.

## REFERENCES TO CHAPTER 4


4-1 F. Wagner, G. Becker, K. Behringer, D. Campbell, A. Eberhagen et al., Phys. Rev. Lett. **49**, 1408(1982).

4-2 M. Keilhacker, G. Becker, K. Behringer, D. Campbell, A. Eberhagen et al., Proc. of 9 th Int. Conf. on Plasma Phys. and Cont. Nucl. Fusion Research, Baltimore, 1982, Vol. 3, IAEA, Vienna, 183(1983).

4-3 M. Shimada, M. Nagami, K. Ioki, S. Izumi, M. Maeno et al., Phys. Rev. Lett. **47**, 796(1981).

4-4 T. Fukuda and A. Nagashima, Proc. of 9 th Int. Conf. on IR & MM Waves, Takarazuka, 258, 1984.

4-5 A. Nagashima, T. Fukuda, S. Kajiura, A. Inoue et al., Proc. of 9 th Int. Conf. on IR & MM Waves, Takarazuka, 264, 1984.

4-6 H. Yoshida, S. Niikura, K. Shimizu, T. Ando, H. Nakamura, K. Nishitani et al., Nucl. Fusion, **28**, 318(1988).

4-7 H. Yoshida, K. Shimizu, and M. Azumi, JAERI-M 86-008 (1986).

4-8 S. Saito, M. Sugihara, and N. Fujisawa, J. Nucl. Mater. **121**, 199(1984).

4-9 Y. Shimomura, H. Maeda, H. Kimura, M. Azumi, K. Odajima et al., JAERI-M 7457 (1977).

# CHAPTER 5. FARADAY ROTATION ANGLE MEASUREMENT FOR THE EVALUATION OF CURRENT DENSITY PROFILES AND CONFINEMENT PROPERTIES ON JT-60

Faraday rotation angle was measured by twin cw 118.8-μm methyl-alcohol laser polari-interferometer as an intensity ratio of lock-in amplified 2 MHz heterodyne beat signals. They are produced by mixing each orthogonal polarization components of the rotated linear polarization of the probing laser beam with the reference wave. From the measured rotation angle, combined with line electron density obtained concomitantly and magnetic probe data, current density profile and thereby the values of $l_i$ and $\beta_p$ were evaluated by applying equilibrium calculations for the analysis of confinement properties. The current density profile of ohmically heated plasmas peaks gradually after the initiation of plasma current with a time constant of around 3 s which is consistent with the resistive skin time evaluated assuming Spitzer conductivity and electron temperature obtained by ECE (Electron Cyclotron Emission) diagnostics. Application of non-inductive lower hybrid current drive substantially flattens the current density profile to suppress sawtooth activities, and the value of $\beta_p$ enlarges for the compound heating with lower hybrid current drive (LHCD) and neutral beam (NB) heating, which implies the improvement of incremental energy confinement time. For NB heated plasmas, current density profile shows minimal flattening, which corresponds to the electron temperature profile. Ion cyclotron radio frequency (ICRF) heated plasmas, on the other hand, have demonstrated the peaked current density distribution.

## 5. 1 INTRODUCTION

The current density profile *j(r)* within a tokamak plasma is a quantity of basic and primary interest as it is

recognized to be a key to the understanding of confinement properties, energy deposition profiles, and gross MHD stability. The recent results on the TEXTOR tokamak have demonstrated the effectiveness of clarifying the current density profile to elucidate ubiquitous MHD activities for ohmic discharges,[5-1] and the possibility of actively modifying the current density distribution with lower hybrid waves has been proclaimed.[5-2,3] However, in spite of its potential importance, the current density profile (or equivalently the poloidal magnetic field distribution) in additionally heated plasmas has not been adequately diagnosed. By extending the interferometer system developed on JT-60 to the Faraday rotation angle measurement, temporal evolution of the current density profile and confinement properties of plasmas heated in various methods have been evaluated.

The diagnostic layout for the concomitant measurement of the Faraday rotation angle with line electron density is shown in Fig. 3-2. The diagnostic chord is situated at half the minor radius outside ($R$ = 3.55 m) of the plasma center ($R$ = 3.04 m) so that the measured Faraday rotation signal is insensitive to the change of the current density profile close to the plasma periphery such as the initial shrink of the surface current right after the initiation of the plasma current. The 118.8-μm radiation was chosen as an interferometer light source in order to minimize the elliptization of linear polarization of the probing laser beam (Cotton-Mouton effect)[5-4,5] as well as to sustain the rotation angle at desirable values. The elliptization is generally significant for large tokamaks due to the high electron density and large toroidal induction along the long penetration distance inside the plasma. Faraday rotation angle has been measured as an intensity ratio of lock-in amplified 2 MHz heterodyne beat signals produced by mixing each orthogonal polarization components of the Faraday rotated linear polarization of the probing laser beam with reference waves.[5-6] The lock-in detected signal

is low-pass filtered to yield the frequency response of 5 kHz. The adoption of a crystal quartz etalon, as a beam splitting materials, contributes to the elimination of the intrusion of the spurious signal due to the large magnetic field penetrating through all the optical components as well as the effect of the mechanical vibrations induced by the plasma discharge. All the signal processing unit has been designed so as to maintain linear responses in the range of interest to yield numeric calibrations of the Faraday rotation angle with a programmed matrix transfer function. Calibration of the rotation angle with a half-wave etalon plate is carried out for every plasma pulse with a motor-drive unit actuated by the timing signal sent from the JT-60 central control system.[2-12] The resolution of the Faraday rotation angle has been calibrated to give less than 0.25°.[5-7]

One of the difficulties which previous Faraday rotation angle measurement has envisaged is to establish a proper physical interpretation method. In this work, modification of the current density profile is evaluated quantitatively in terms of the plasma internal inductance $l_i$. The value of $l_i$ is defined on the basis of stored magnetic energy per unit length of a plasma colomn $W_{mag}$ , which is given by

$$W_{mag} = \frac{1}{2} \left( \frac{\mu_o l_i}{4\pi} \right) I_p^{\,2} = \int_o^a \frac{B_p^2(\rho)}{2\mu_o} 2\pi\rho \, d\rho , \qquad (5.1)$$

where

$$B_p(\rho) = \frac{\mu_o I_p}{2\pi\rho} . \qquad (5.2)$$

Therefore, $l_i$ is written in a form:

$$l_i = \frac{2\int_o^a B_p^2(\rho)\,\rho\, d\rho}{a^2 \{B_p(a)\}^2} . \qquad (5.3)$$

Here, $B_p$, a, and $\rho$ are the poloidal magnetic field, minor radius, and the distance between the magnetic axis and magnetic flux surfaces respectively. As seen in (5.1), the value of $l_i$ is directly related to the poloidal magnetic field distribution. It is readily shown by an application of the electromagnetic theory that the value of $l_i$ decreases, if *j(r)* is flattened. From the measured rotation angle, the value of $\beta_p$ was evaluated by separating from Shafranov lambda $\Lambda$ for the confinement analysis.

## 5. 2. ANALYSIS PROCEDURE

From the measured Faraday rotation angle, combined with the line electron density data obtained concomitantly and the magnetic data, current density profile and thereby the values of $l_i$ and $\beta_p$ were evaluated by applying a MHD equilibrium calculation. The analysis procedure is depicted in Fig. 5-1. The outermost magnetic flux surface is first of all identified with the FBI code which employs the filament current method,[5-8] and the inner magnetic flux surfaces are determined by solving the Grad-Shafranov equation:

$$\frac{\partial^2 \psi}{\partial R^2} - \frac{1}{R}\frac{\partial \psi}{\partial R} + \frac{\partial^2 \psi}{\partial Z^2} = -\mu_o R j_\phi , \qquad (5.4)$$

supposing the current density profile in the simple parametric form:[5-9]

$$j_\phi = j_0 \{ \beta_p \frac{R}{r} + (1-\beta_p)\frac{r}{R} \} \left(1 - \frac{\psi_{ax} - \psi}{\psi_{ax} - \psi_s}\right)^m . \qquad (5.5)$$

Here, $\psi_{ax}$ and $\psi_s$ stand for the magnetic flux function at the magnetic axis and the plasma surface, and a symmetric plasma configuration with respect to the toroidal midplane is supposed. The determined outermost magnetic flux surface is used as the boundary conditions to solve the equilibrium equation. Another output from the FBI code is Shafranov lambda ($\Lambda = \beta_p + l_i/2 - 1$). The value of poloidal beta $\beta_p$ in (5.5), which characterizes the confinement

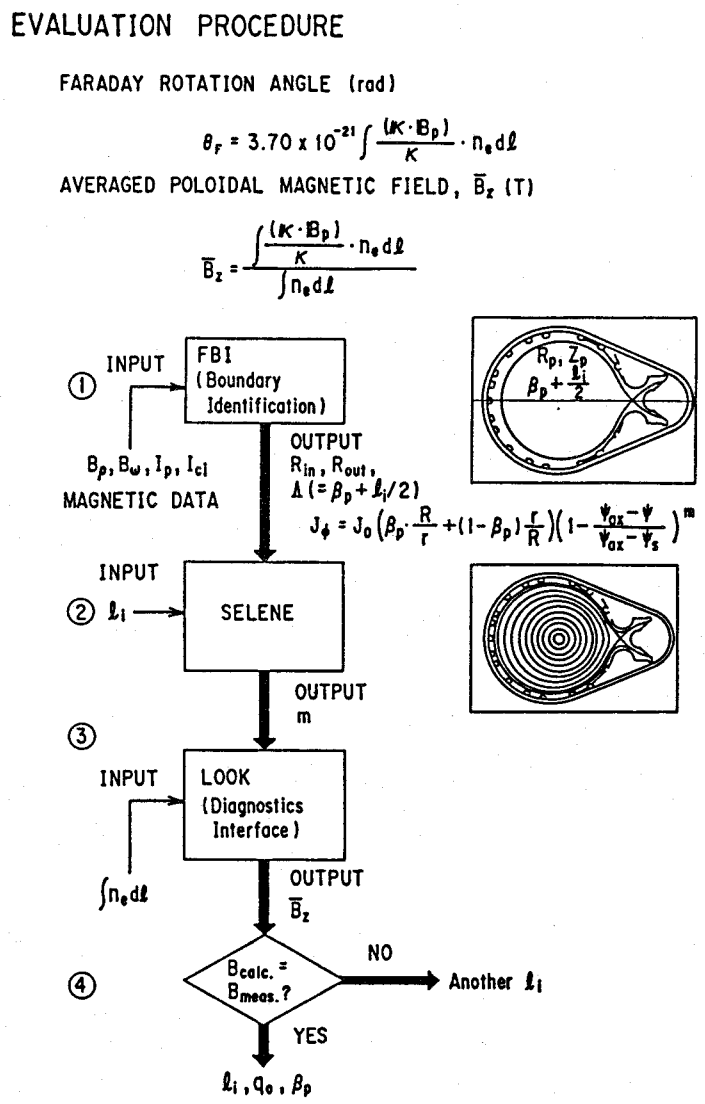


Fig. 5-1 The evaluation procedure of the current density profile, electron density profile, plasma internal inductance($l_i$), and $\beta_p$ from the Faraday rotation angle measurement.

property and the position of the magnetic axis, is determined by subtracting the value of plasma internal inductance $l_i$ from Shafranov lambda. The measured line electron density is inverted into a electron density profile, supposing that the electron density is constant along a certain magnetic flux surface, and the electron density profile is in a form (LOOK code)[5-10] :

$$ne(r) = neo\,(\,1 - \rho^2 / a^2\,)^M . \qquad (5.6)$$

Here, M is the profile parameter which is determined by the least-square fitting with the measured 4-channel line electron density data. The profile parameter m in (5.5) is evaluated by the iterative calculation, with $l_i$ as a convergence parameter, so that the calculated Faraday rotation angle along the actual diagnostic chord coincides with the measured value $\theta_F$, which is given by

$$\theta_F = 3.71 \times 10^{-21} \int \frac{(\mathbf{k}\cdot\mathbf{B}_p)}{k} n_e \, dl . \qquad (5.7)$$

(5.7) is derived assuming a cold plasma dispersion relation on a Lorenz plasma with a homogeneous static magnetic field and WKB approximation and neglecting the collision frequency $\nu$ (= $4.3 \times 10^3$ for $n_e = n_i$, $n_e = 1.0 \times 10^{20}$, and $T_e = 1 \times 10^4$ eV). The obtained electron density profile M from (5.6) and the profile measured by Thomson scattering agree within the accuracy of 10%. The assumption that equi-density surface coincides the magnetic flux surface is applicable only for low beta plasmas. Therefore the agreement of electron density profiles obtained by two methods have been examined case by cases for *j(r)* evaluation. Therefore, in the evaluation procedure, the effect of density profile and position of the magnetic axis are taken into consideration, but the validity of the parametric form of *j(r)* and $n_e(r)$ written in (5.5) and (5.6) is still left to be an assumtion. Substituting the error bars for the rotation angle measurements in the evaluation code,

the error bars of $l_i$ have been estimated. They are found to be large for the low-density experiment; typically 0.08 at $\bar{n}_e = 5.0 \times 10^{18} m^{-3}$, and they are less than 0.04 for medium- to high-density experiments. The effect of alternation of the density profile parameter M in the code has also been surveyed. Substitution of the caluculated value of M ± 0.5 modified the obtained value of $l_i$ no more than 0.01.

The developed analysis method experimentally separates the value of $l_i$ from Shafranov lambda to yield the value of $\beta_p$ concomitantly even for plasmas with circular cross section.[5-11] The energy confinement time $\tau_E$ (= internal stored energy $W$/ input energy $P_{in}$) can be evaluated by the formula:

$$\tau_E = \frac{1.43\{ I_p (MA) \}^2}{P_{in} (MJ/s)} \beta_p, \tag{5.8}$$

Since

$$W = \frac{3}{2} \int [ n_e(r) T_e(r) + n_i(r) T_i(r) ] dV = \frac{3}{2} <nT> V,$$

$$\beta_p = \frac{<nT>}{B_p^2 / 2\mu_o}, \quad V = 2\pi^2 a^2 R. \tag{5.9}$$

Therfore, $W$ is rewritten as

$$W = \frac{3}{2} \frac{B_p^2}{2\mu_o} \beta_p 2\pi^2 a^2 R = 3\pi^2 a^2 R \frac{\beta_p}{2\mu_o} \left( \frac{\mu_o I_p}{2\pi a} \right)^2. \tag{5.10}$$

In comparison with other evaluation methods of energy confinement time, this scheme requires neither full electron and ion temperature nor density profile, and it is effective for the analysis during the plasma pulse interval. Furthermore, the obtained value of $\beta_p$ includes both the components perpendicular and parallel to the magnetic field. The diamagnetic measurement considers only the perpendicular component of $\beta_p$. In order to confirm the accuracy of this evaluation method, the value of incremental energy confinement time obtained between two methods have been compared: one by the Faraday rotation angle

measurement combined with the equilibrium calculations and the other by the diamagnetic measurement. They agreed within the accuracy of 10% when except for the case when lower hybrid (LH) wave was injected. This infers the production of the high energy component in the electron pressure parallel to the magnetic field in the LH wave injection case. Although the evaluation of *j(r)* with only one diagnostic chord suffers intrinsic difficulty on the $q_{axis}$ resolution, developed method yields adequate resolution on the confinement analysis. By combining the value of poloidal beta $\beta_p^{eq.}$ evaluated from the Faraday rotation angle measurement and the perpendicular component of the poloidal beta $\beta_p^{\perp}$ from the diamagnetic measurement, an amount of the parallel component of poloidal beta $\beta_p^{//}$ can be evaluated by subtracting $\beta_p^{\perp}$ from $\beta_p^{eq.}$. The degree to which a contribution of non-thermal electrons is instrumental in effecting the Faraday rotation of the electric field vector of the probing laser beam, however, must be further investigated introducing a dispersion relation of hot plasmas.

## 5. 3 EXPERIMENT

The result of Faraday rotation angle measurement for an ohmic discharge is shown in Fig. 5-2. In the figure, rotation angle is converted into the averaged poloidal magnetic field $\overline{B_z}$ expressed by

$$\overline{B_z} = \frac{\int \frac{(\mathbf{k}\cdot\mathbf{B}_p)}{k} n_e dl}{\int n_e \, dl}, \qquad (5.11)$$

which is convenient for the simplified analysis of the current density profile during the plasma pulse interval. Although the value of $\overline{B_z}$ is dependent on the electron density profile and position of the magnetic axis, it is

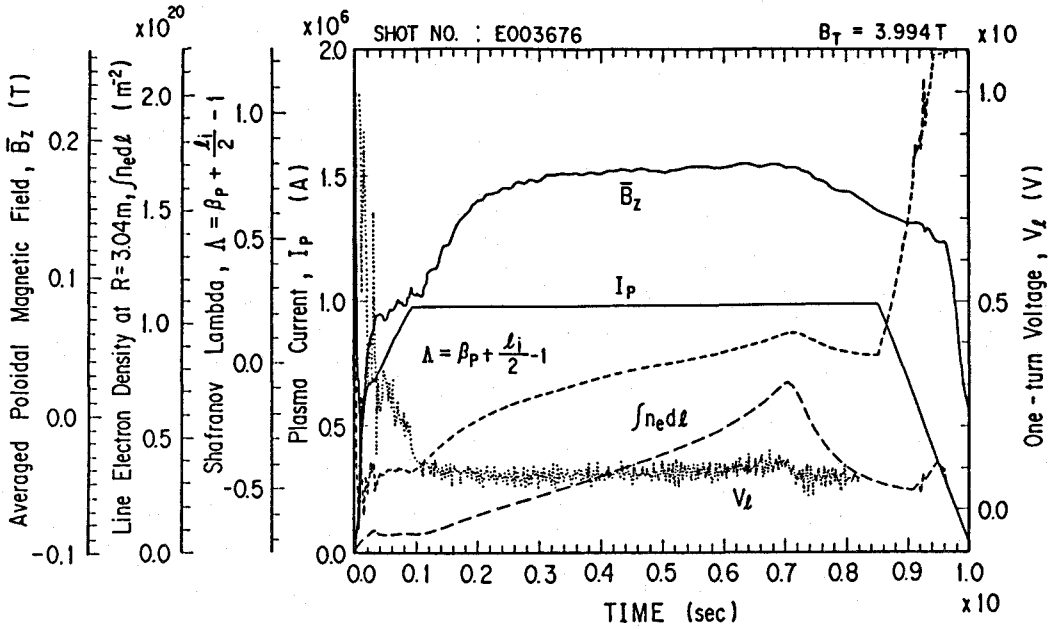


Fig. 5-2 Temporal evolution of the averaged poloidal magnetic field($\overline{B_z}$) for the ohmically heated plasma, shown with the plasma current, one-turn voltage, Shafranov lambda, and line electron density at R = 3.04 m chord.

effective to inform of the temporal evolution of the relative amount of the integrated current density in the area between the magnetic axis and diagnostic chord.

The current density profile of ohmic plasmas peaks gradually after the plasma current is initiated with a time constant of 3 s which is consistent with the resistive skin time calculated assuming Spitzer conductivity and the electron temperature of 1 keV measured by ECE diagnostics. The gradual increase of $\overline{B_z}$ during the flat-top of the plasma current is due to the plasma edge cooling by the continuous fuel gas puffing. When the plasma current $I_p$ was raised from 1.0 to 1.5 MA after the penetration of plasma current was completed, the value of $\overline{B_z}$ increased slowly according to

the larger resistive skin time due to higher electron temperature compared to the initial plasma current rise phase, and it attains the value 1.2 times larger than that for $I_p$ = 1.0 MA. Therefore, the value of $\overline{B_z}$ is not linearly correlated to $I_p$, and this result implies that quite a long time is required for the plasma current to finish penetrating for high plasma current experiment.

When the plasma current of 1 MA is modulated by 3% at 20 Hz, the value of $\overline{B_z}$ increased as documented in Fig. 5-3

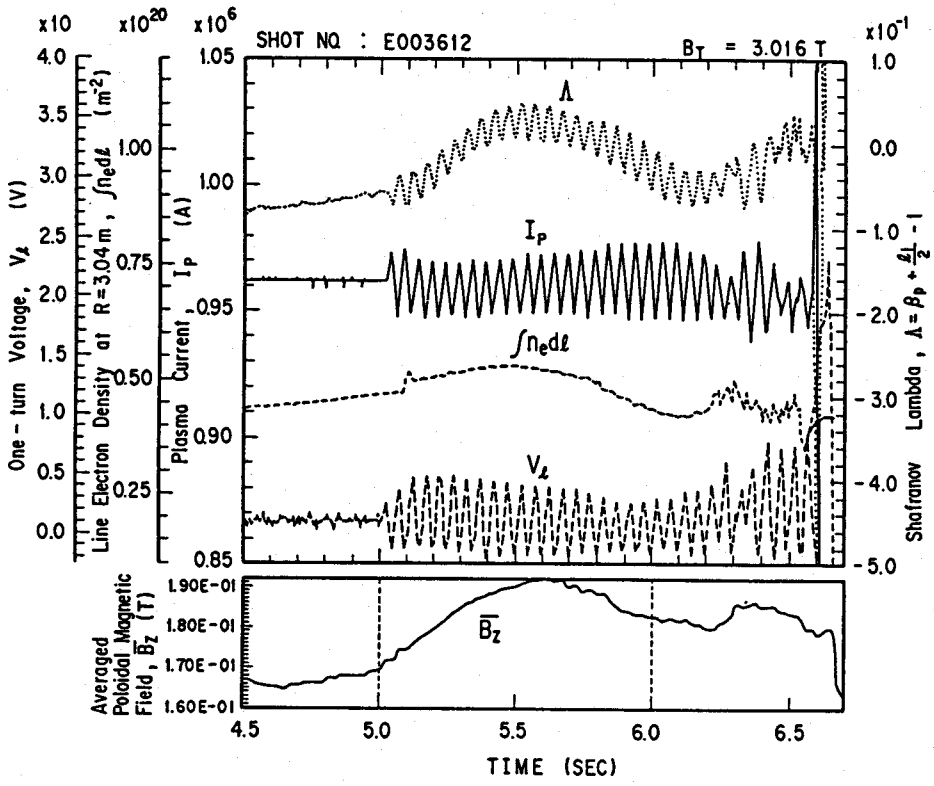


Fig. 5-3 Temporal evolution of the averaged poloidal magnetic field($\overline{B_z}$) (lower figure) for a plasma with its plasma current of 1 MA modulated by 3 % at 20 Hz, shown with the plasma current, one-turn voltage, Shafranov lambda, and line electron density at R = 3.04 m chord (upper figure).

(lower figure). The value of Shafranov lambda, plasma current, line electron density at $R$ = 3.04 m chord, and loop voltage are juxtaposed against the temporal evolution of $\overline{B_z}$ (upper figure). Application of an equilibrium analysis has yielded an increase of $l_i$ by 0.04 in this case. Therefore the increment of $\Lambda$ is reduced to the improvement of $\beta_p$ by 0.07 as a dominant term. Here, a reduction of $H_\alpha$ emission and the enhanced soft X-ray radiation from the edge plasma region were also observed. The modified amount of $l_i$, $\Lambda$, and $\beta_p$ are documented in Fig. 5-4, which correlates the modified amount of $\Lambda$ and $l_i$ to extract the increment of $\beta_p$. The horizontal axis in Fig. 5-4 is the *maximum* modified amount of $l_i$ attained in a discharge. Since it takes a few seconds for the *j(r)* modification to take effect to reach a steady state, the data points are plotted as differences of $l_i$ evaluated before the additional heating and steady state. The evaluated amount is divided by two in order to simplify the comparison with the value of Shafranov lambda on the vertical axis. A data plot in the left-hand side of the vertical axis indicates the flattening of *j(r)* , and if a plotted point is situated further left in this region, it means the substantial flattening of *j(r)* . The right-hand side of the vertical axis, on the other hand, is for the peaking cases of *j(r)*. The oblique line from the upper right to down left is where the increment of $\beta_p$ is null. If the plotted data is situated far upper left of this line, it indicates the large increment of $\beta_p$, while the lower right region is for the degraded cases.

Suppression of the skin effect by a moving limiter synchronized with the rising plasma current was suggested by Kadomtsev[5-12] for the first time. The application of a moving limiter can possibly prevent the dissipation of the plasma energy resulting in the loss of volt-seconds, however, the instabilities due to the low q configuration may induce MHD instabilities. When moving limiters are applied during the plasma current rise, faster rise of $\overline{B_z}$ has been observed during 0.05 to 0.3 s in comparison with a

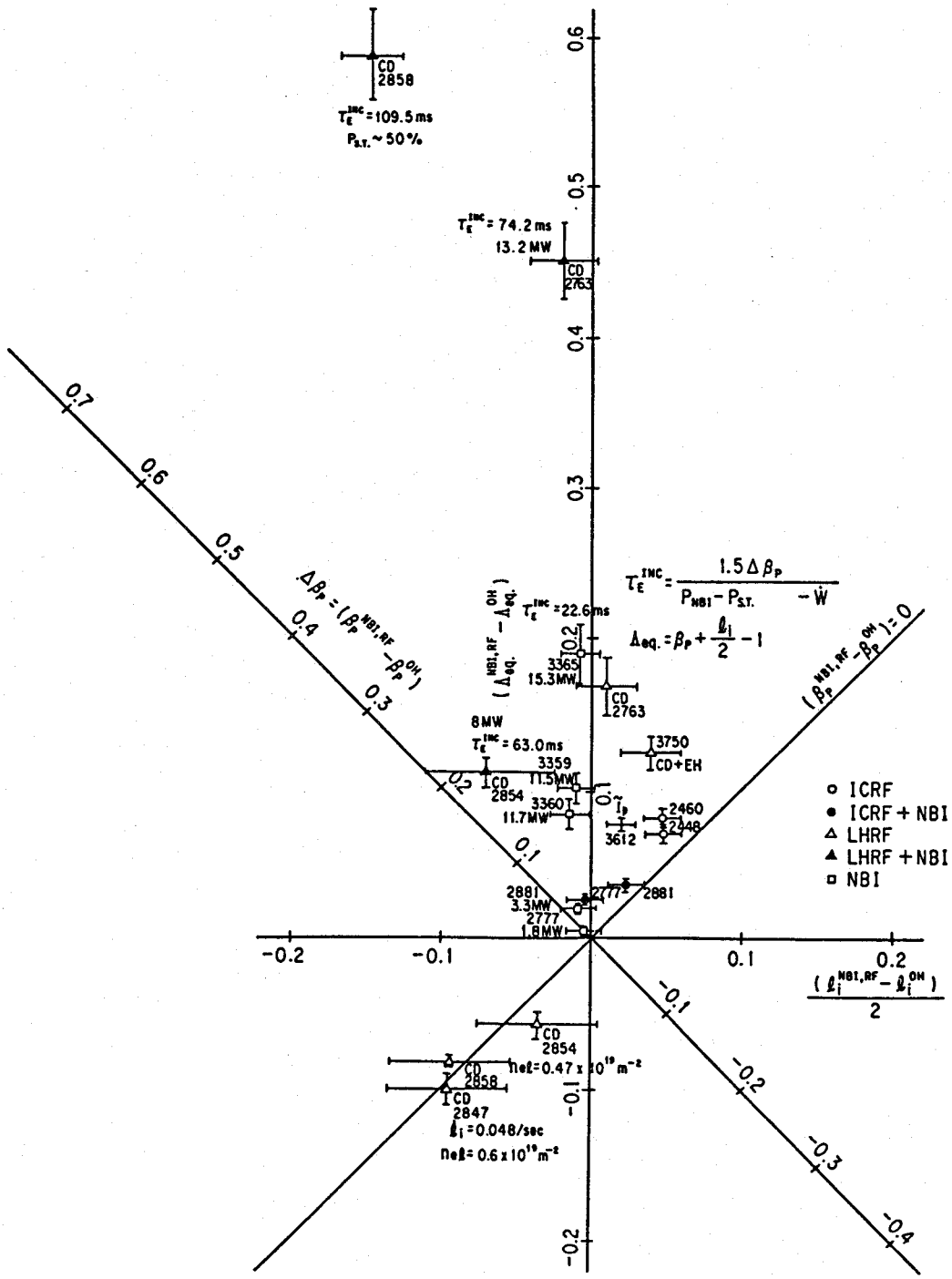


Fig. 5-4 The correlation between the maximum change of the plasma internal inductance and Shafranov lambda for the evaluation of the increment of the poloidal beta.

fixed-limiter discharge as shown in Fig. 5-5(a) and (b), which infers that moving limiters yield faster current penetration into the central region of a plasma. The plasma current rise-rate for the fixed-limiter discharge depicted in Fig. 5-5(b) was 2.2 times larger than that of the moving-limiter discharge. For the moving-limiter experiment, the minor radius was set to be 0.62 m at the beginning of the discharge, and it was linearly driven from 0.2 s to 0.75 s to produce the fixed limiter configuration ($a$ = 0.92 m). The loop voltage during the moving-limiter configuration are lower than that of the fixed-limiter configuration due to the decrease of plasma inductance caused by the enlargement of the minor radius, while the value of Shafranov lambda is larger with the moving limiter. This result is consistent with the larger value of $\overline{B_z}$ obtained by the Faraday rotation angle measurement. Electron temperature evaluated by the soft X-ray measurement also indicates a rather peaked profile, and the electron density profile is supposed to be flat from the interferometric measurement in a moving-limiter experiment. In addition, larger amplitude of $\widetilde{B_\theta}$ with the moving-limiter configuration has been observed, and sawtooth activities started at earlier times.

In order to evaluate the plasma conductivity, $\overline{B_z}$ profile has been calculated with a 1D-tokamak transport code, supposing the electron temperature profile measured by Thomson scattering, a flat $Z_{eff}$ profile with $Z_{eff}$ = 1.5, and either Spitzer or neoclassical conductivity. The result of calculation together with the measured value is shown in Fig. 5-6. The measured data point situates close to the curve calculated according to the Spitzer conductivity.

As for the case when NB heating is applied onto a full size plasma with a divertor configuration, the value of $\overline{B_z}$ holds the same value as shown in Fig. 5-7. The result of equilibrium analysis, however, claims the flattening of current density profile, which is consistent with the electron

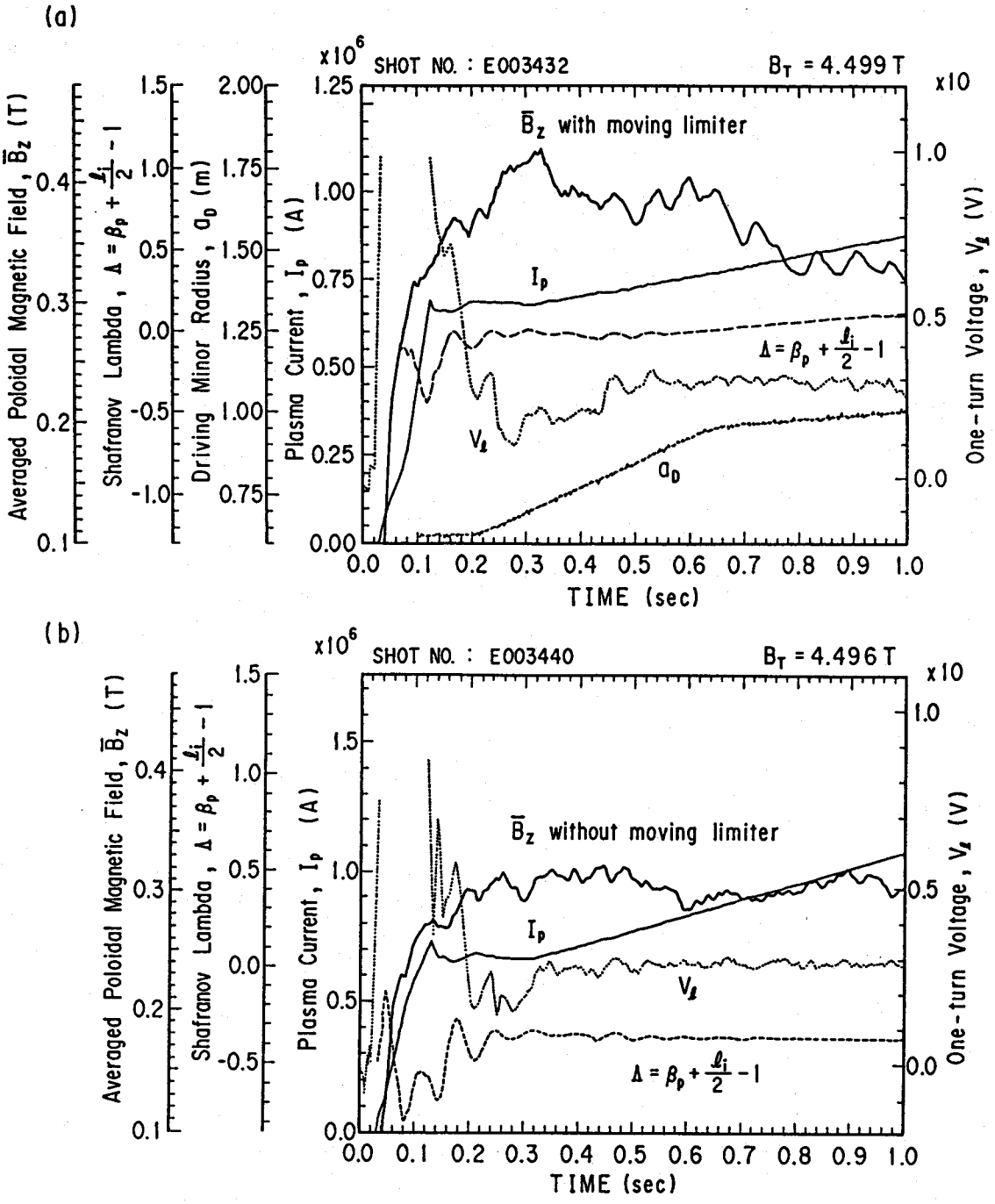


Fig. 5-5 Temporal evolution of the averaged poloidal magnetic field($\overline{B_z}$) for a plasma (a) with and (b) without the application of a moving limiter, shown with the plasma current, one-turn voltage, Shafranov lambda, and the driving minor radius.

temperature profile measure by ECE diagnostics. The reduced amount of $l_i$ evaluated by the application of the equilibrium analysis is less than 0.03 as can be seen in Fig. 5-4. Although the NB heating pulse length is only 1 s, the above discussion holds for a experiment with longer pulse NB heating. Alternation of $j(r)$ certainly depends on the energy deposition profile, and the peaking of $j(r)$ for a small-bore plasmas have been actually observed.

When a plasma is ICRF heated, the value of $\overline{B_z}$ increases as shown in Fig. 5-8. JT-60 is equipped with a phased 2 x 2 loop antenna for the 2 nd harmonic ion cyclotron resonance heating.[5-13] The frequency of the injected wave is 130 MHz. The phase difference between the toroidally neighboring loop antenna was set to be zero in

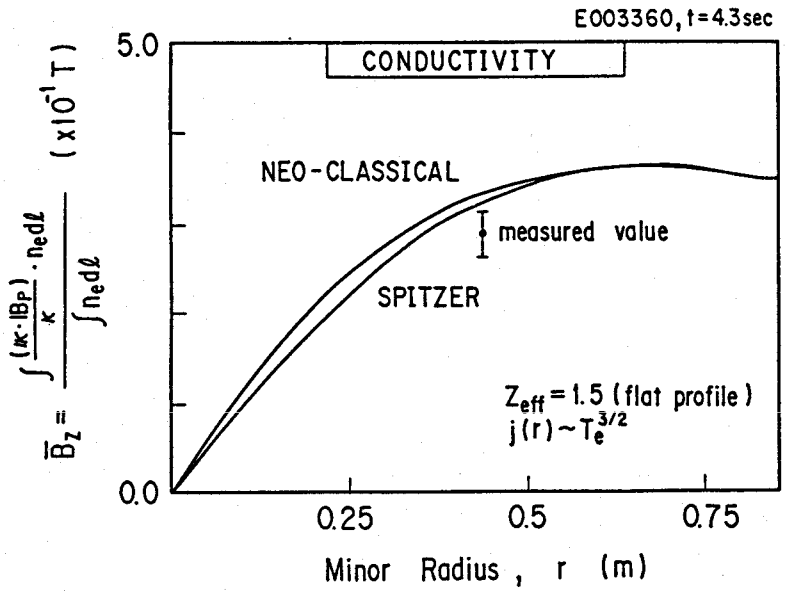


Fig. 5-6 The profile of the averaged poloidal magnetic field calculated from the electron temperature profile measured by the Thomson scattering, assuming either Spitzer or neoclassical conductivity for the comparison with a measured value.

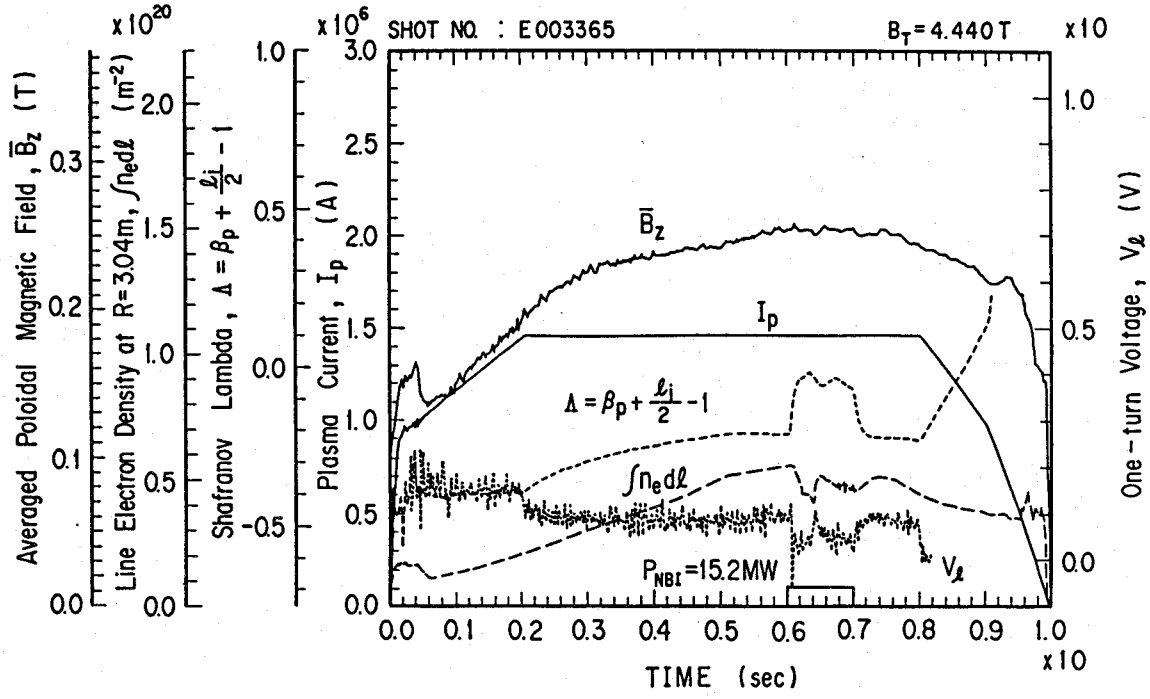


Fig. 5-7 Temporal evolution of the averaged poloidal magnetic field($\overline{B_z}$) for the NB heated plasma, shown with the plasma current, one-turn voltage, Shafranov lambda, and line electron density at R = 3.04 m chord.

this case. The evaluated increment of $l_i$ and $\beta_p$ are 0.092 and 0.025, respectively as shown in Fig. 5-4. Therefore, the increased amount of $\Lambda$ is mainly attributed to the increase of $l_i$. Although a slight increase of the central electron temperature has been observed, the increment of loop voltage and the increase of $Z_{eff}$ during the ICRF injection pronounced by the spectroscopic measurements claim that the radiation cooling at the edge plasma region is the dominant factor to contribute to the peaking of *j(r)*. The decrease of the electron temperature in the peripheral region of a plasma and the feedback control of the plasma current to sustain a constant value can cause the peaking of *j(r)*. When the phase difference between the toroidally neighboring loop antenna was set to be $\pi$ with other

parameters kept the same, less increase of $l_i$ and the improvement of $\beta_p$ has been observed. Application of NB heating on a ICRF heated plasma reduces the value of $l_i$ with larger amount of reduction ($\Delta l_i$ = -0.09) compared to the case when NB heating is solely applied. Therefore, the reduced amount of $l_i$ is by the application of NB heating depends on the initial value of $l_i$; in other words, the reduced amount of $l_i$ is large in a case when NB heating is applied on a plasma with a peaked current density profile. The JT-60 ohmic plasma in a divertor configuration is assumed to have a very flat current density profile, therefore the NB heating alone induces the insignificant modification of *j(r)*, compared to NB heating + ICRF case.

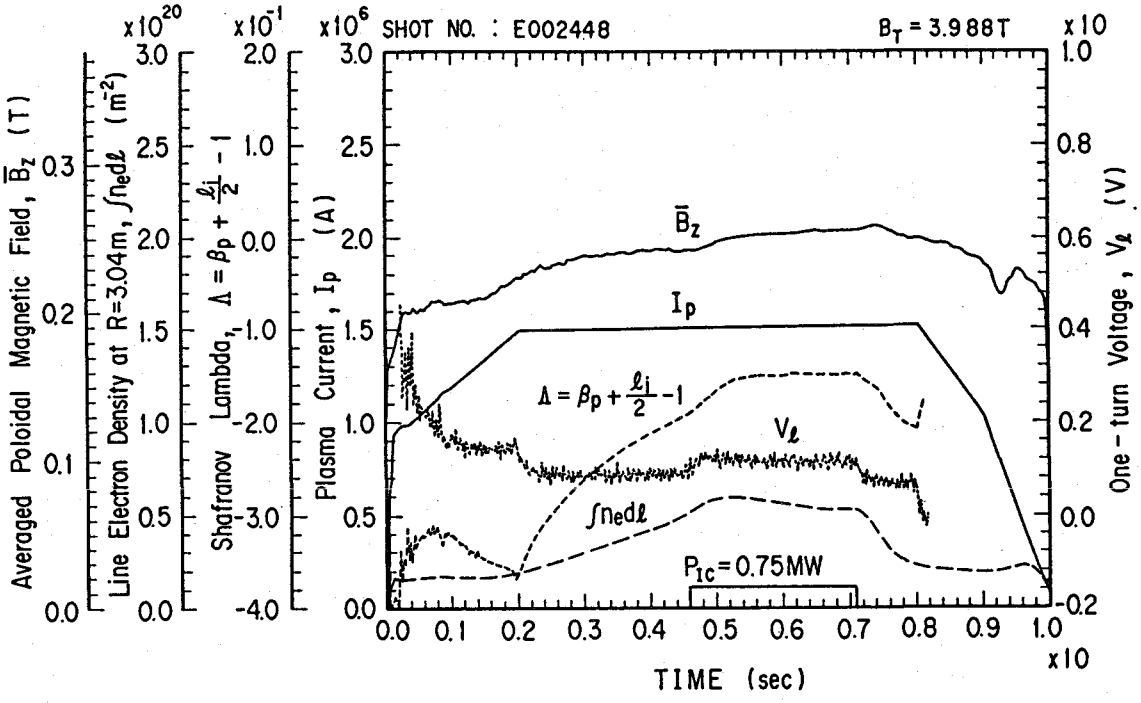


Fig. 5-8 Temporal evolution of the averaged poloidal magnetic field($\overline{B_z}$) for the ICRF heated plasma, shown with the plasma current, one-turn voltage, Shafranov lambda, and line electron density at R = 3.04 m chord.

As for the lower hybrid wave injection experiment, JT-60 has two types of launchers.[5-14] One is optimized in its dimension for the current drive (CD-unit), and the other for the plasma heating. (H-unit) When lower hybrid wave is injected with CD-unit, the value of $\overline{B_z}$ substantially decreases, which indicates the flattening of the current density profile as shown in Fig. 5-9. Here, the injected RF power is 1.1 MW, $\Delta\varphi$ (phase difference between the toroidally neighboring launchers) = 90° to yield the value of the refractive index along the magnetic field $\overline{N_{//}}$ and $\Delta N_{//}$ (FWHM of $N_{//}$) to be 1.7 and 1.0 respectively (calculated from the Brambilla theory[5-15]) , $\bar{n}_e$ = 0.3 x $10^{19}$ $m^{-3}$, $B_T$ = 4.0 T, and Ip = 1.0 MA. Experiments are mainly carried on

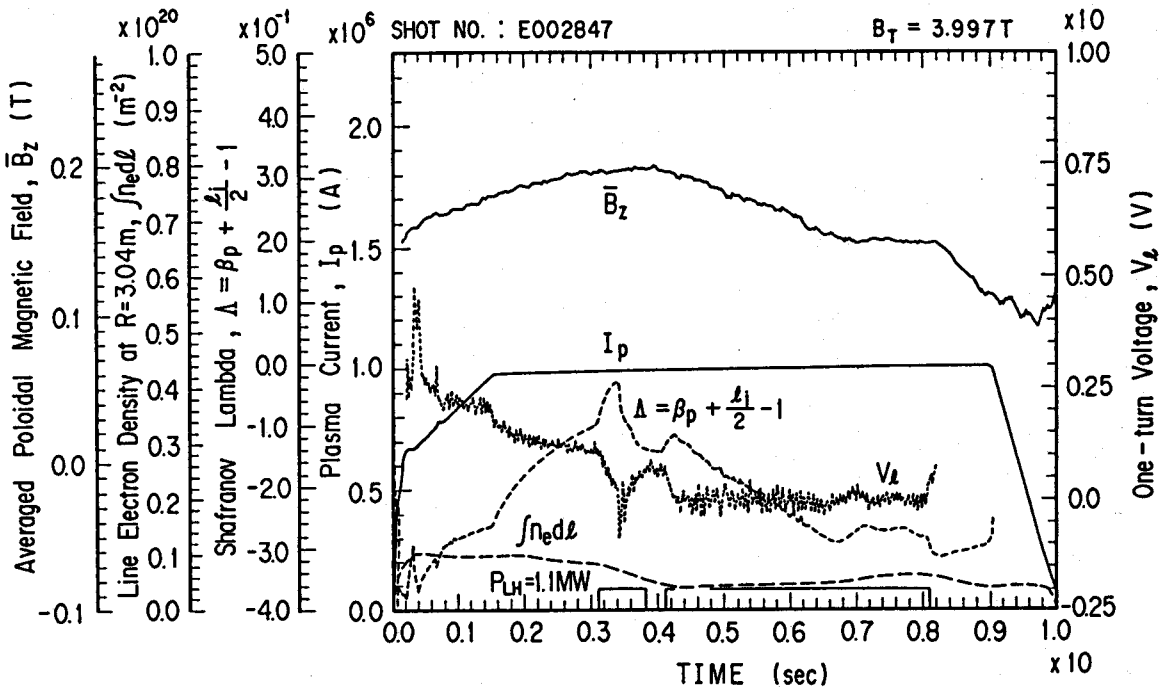


Fig. 5-9 Temporal evolution of the averaged poloidal magnetic field($\overline{B_z}$) for the LHCD applied plasma, shown with the plasma current, one-turn voltage, Shafranov lambda, and line electron density at R = 3.04 m chord.

helium plasmas with $q_a > 3$. The induced plasma current is replaced by a RF current during the LH pulse as seen by the negative value of the loop voltage $V_l$. Here, the plasma current is feedback controlled to hold the constant value. By the application of an equilibrium calculation, the gradual decrease of Shafranov lambda is identified as a decrease of $l_i$, and the reduced amount of $\Lambda$ for LHCD applied plasmas is approximately equal to that of $l_i/2$ (Fig. 5-4). The analysis of $\beta_p''$ from the Faraday rotation angle measurement combined with the diamagnetic measurement has implied that the value of $\beta_p''$ is approximately kept constant during the RF pulse excluding the case when a minor disruption has occurred, which is consistent with the results of ECE diagnostics.

Since the value of $l_i$ and $\Lambda$ reduces approximately by the same amount, the increase of $\beta_p$ stays within the error bars of the measurement. Although the suppression of sawtooth activities was observed during the RF pulse by the effective flattening of $j(r)$, the incremental energy confinement was less than 15 ms. Since NB pulse length is only 0.5 s, a correction of ohmic input power has been included for the evaluation of incremental energy confinement time. When the NB heating is applied on the plasma of which current density profile is effectively flattened, significant increase of the energy confinement time was observed. The temporal evolution of $\overline{B_z}$ is shown in Fig. 5-10. Sudden rise of $\overline{n_e}$ before the NB heating is, from the spectroscopic measurement, caused by the injection of titanium impurities from the first wall. The metal impurities reduce the central electron temperature, resulting in a sudden decrease in $\overline{B_z}$. The apparent increase of $\overline{B_z}$ right after the LH injection for Fig. 5-9 and 10 is due to the fact that j(r) has not finished penetrating; that is the resistive skin time for helium plasmas are longer than hydrogen plasmas. The incremental energy confinement time for this particular discharge was 110 ms, to yield the

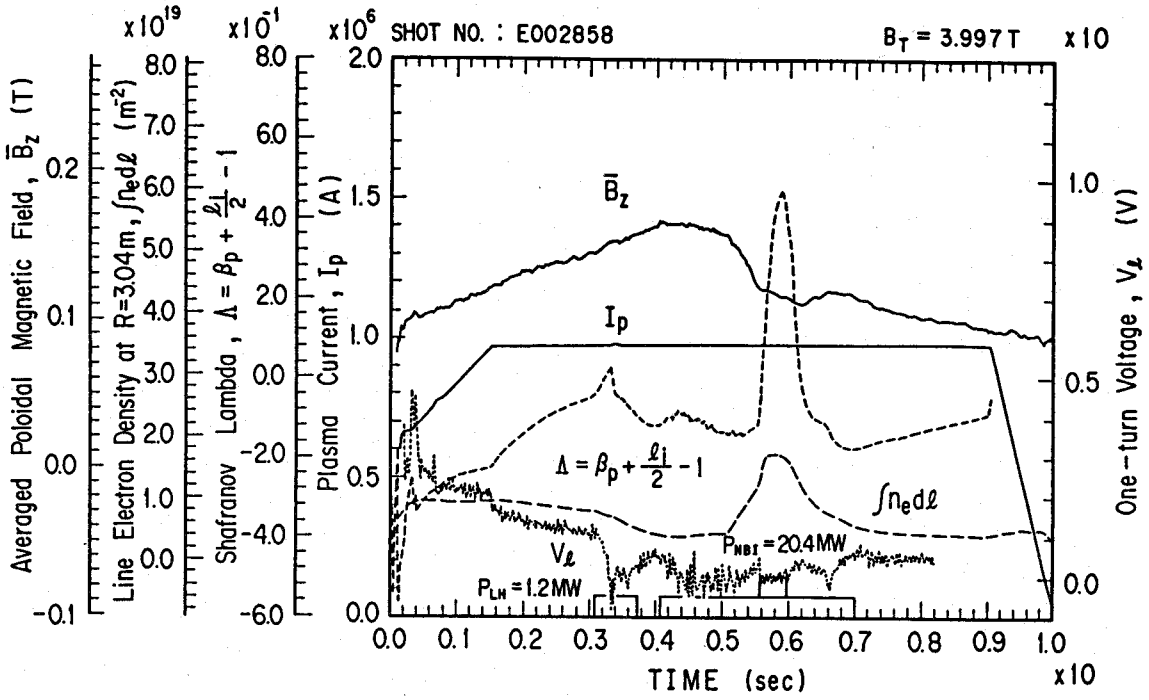


Fig. 5-10 Temporal evolution of the averaged poloidal magnetic field($\overline{B_z}$) for the LHCD applied plasma combined with NB heating plasma, shown with the plasma current, one-turn voltage, Shafranov lambda, and line electron density at R = 3.04 m chord.

global energy confinement time which is approximately equal to that of ohmic discharges in accordance with the plasma current, and it is 2.5 times larger than the value estimated from the Kaye-Goldston scaling.[5-16] The additional reduction of $l_i$ by the superposition of NB heating is 0.1 as shown in Fig. 5-4. This reduction was realized by the improvement of $\eta_{cd}$ (= $R\bar{n}_e I_{RF}/P_{LH}$ , scales well with 6 $<T_e>/(5 + Z_{eff})$[6-10]) due to the increase of electron temperature.

When the H-unit is applied on a plasma with its electron density gradually increased, the value of $\overline{B_z}$

increased in the low density region (until t = 4.5 s) as shown in Fig. 5-11. Here, the launcher phasing $\Delta\phi$ was 180° (to yield the value of $\overline{N_{//}}$ and $\Delta N_{//}$ to be 1.8 and 0.5 respectively) and $\eta_d$ = 0.5. The electron temperature measured by Thomson scattering also increases with a peaked profile. The launcher dimension and phasing does contribute to the modification characteristics of *j(r)* . As the electron density is gradually increased, the value of $\overline{B_z}$ soon saturates and starts to decrease. The reduction of $l_i$ in the medium- to high-density plasmas was often observed.

## 5. 4. CONCLUSION

The Faraday rotation angle measurement, which

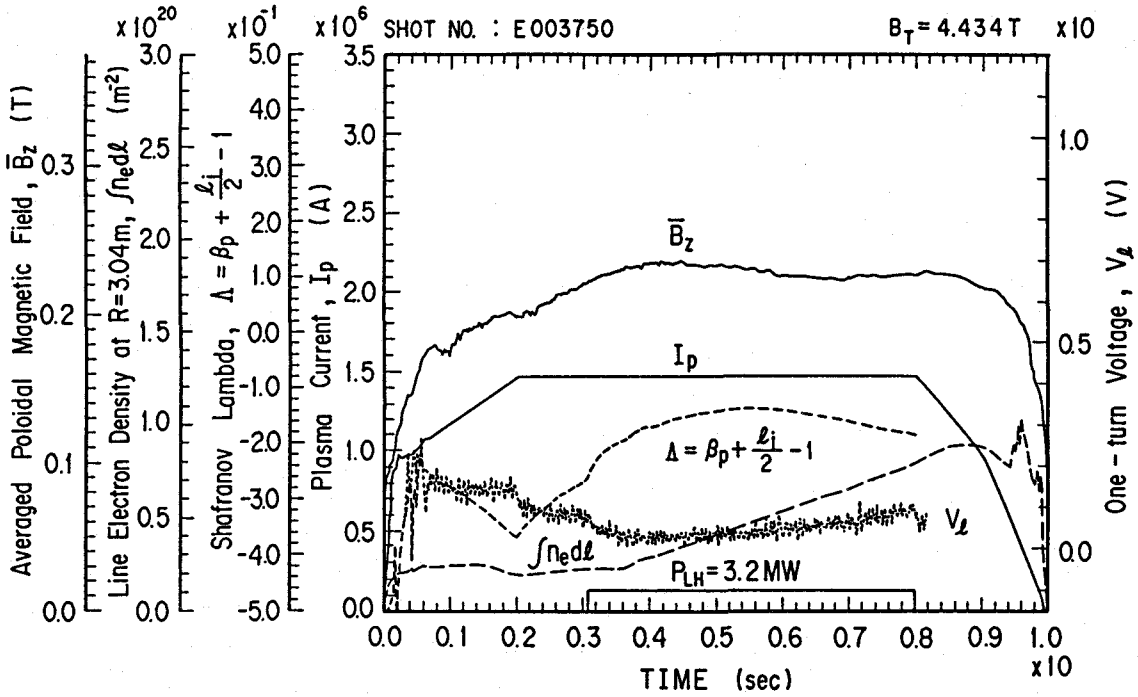


Fig. 5-11 Temporal evolution of the averaged poloidal magnetic field($\overline{B_z}$) for the LHEH applied plasma, shown with the plasma current, one-turn voltage, Shafranov lambda, and line electron density at R = 3.04 m chord.

provides continuous data throughout the entire plasma discharge, has been carried out for the ohmic and additionally heated plasmas. The obtained results are combined with a MHD equilibrium calculation for the current density profile and confinement analysis. Due to the intrinsic restrictions of having only one diagnostic chord, the resolution of q on the magnetic axis is severely limited, however, the evaluation of $l_i$ and $\beta_p$ has brought precious informations on the value of incremental energy confinement time. The newly developed method experimentally separates the value of $l_i$ from Shafranov lambda, and it is effective especially for the case when lower hybrid wave is launched into the plasma, where large anisotropy in the electron pressure profile exists. The developed evaluation method pronounces its effectiveness, introducing an alternative approach to the analysis of the Faraday rotation angle measurement.

## REFERENCES TO CHAPTER 5


5-1 H. Soltwisch, W. Stodiek, J. Manickam, J. Schlüter, Plasma Physics and Controlled Nuclear Fusion Research (Proc. 11 th IAEA Conf. Kyoto, 1986), Vol. 1, International Atomic Energy Agency, 263(1987).

5-2 F. X. Söldner, K. McCormick, D. Eckhartt et al., Phys. Rev. Lett. **57**, 1137(1986).

5-3 K. McCormick, F. X. Söldner, D. Eckhartt et al., Phys. Rev. Lett. **58**, 491(1987).

5-4 F. De Marco, S. E. Segre, Plasma Physics **14**, 245(1972).

5-5 A. D. Craig, Plasma Physics **18**, 777(1976).

5-6 H. Soltwisch, Rev. Sci. Instrum. **57**, 1939(1986).

5-7 T. Fukuda, A. Nagashima, H. Yoshida, M. Kikuchi, H. Yokomizo, submitted to Rev. Sci. Instrum.

5-8 D. W. Swain, G. H. Neilson, Nucl. Fusion **22**, 1015(1982).

5-9 M. Azumi, G. Kurita, T. Matsuura, T. Takeda, Y. Tanaka, T. Tsunematsu, Computing Methods in Applied Sciences and Engineering, North Holland Publishing Company, Amsterdam(1980).

5-10 T. Hirayama, K. Shimizu, K. Tani, H. Shirai, M. Kikuchi, Experimental Transport Analysis Code System in JT-60, Japan Atomic Energy Research Institute Rep. JAERI-M 88-043(1988).

5-11 J. L. Luxon, B. B. Brown, Nucl. Fusion **22**, 813(1982).

5-12 I. N. Golovin, Y. N. Dnestrovskii, D. P. Kostmarov, Nuclear Fusion Research Conference, (Proc. Conf. Culham)194; see page 210 for reference to B. B. Kadomtsev. (British Nuclear Energy Society, 1969).

5-13 T. Nagashima, K. Uehara, and H. Kimura et al., Fusion Engineering and design **5**,101(1987).

5-14 K. Sakamoto, T. Imai, Y. Ikeda. et al., Initial results of Lower Hybrid Current Drive Experiment on JT-60, Japan Atomic Energy Research Institute Rep. JAERI-M 87-061(1987).

5-15 M. Brambilla, Nucl. Fusion **16**, 47(1976).

[5-16] JT-60 Team, Plasma Physics and Controlled Nuclear Fusion Research (Proc. 11 th IAEA Conf. Kyoto, 1986), Vol. 1, International Atomic Energy Agency, 563(1987).

# CHAPTER 6. MODIFICATION OF THE PLASMA INTERNAL INDUCTANCE BY THE NON-INDUCTIVE LOWER HYBRID CURRENT DRIVE ON JT-60

The control of plasma internal inductance li was demonstrated to be possible by the lower hybrid wave in a large tokamak. The value of li is obtained from the Faraday rotation angle measurement combined with MHD equilibrium calculations. The reduction of li is significant for the lower hybrid waves with large refractive index and high directivity, and it is proportional to the injected power $P_{LH}$ divided by the averaged electron density $\overline{n}_e$. The optimization scheme of plasma confinement properties by the modification of current density profiles and its mechanism have also been investigated to understand the relationship between the current profile shape and confinement properties. Thereby substantial improvement in the incremental energy confinement time, by the synergetic effect of the lower hybrid current drive combined with neutral beam heating, has been achieved, demonstrating the increase of electron stored energy with a current density profile decoupled from the conductivity profile.

## 6.1 INTRODUCTION

Active modification of the current density profile *j(r)* , possibly independently from the electron temperature profile, in a tokamak plasma is now considered to be of significant importance for the gross MHD stability and improvement of confinement properties. Since *j(r)* in a tokamak plasma couples to the electron temperature profile through local conductivity for the ohmically driven current, large increase in the central electron temperature induces sawtooth activity which inevitably prevents further electron

heating. The recent results on the ASDEX experiment point out that sawteeth can be suppressed by the application of LHCD[6-1,2] by the flattening of $j(r)$ , decoupling from the conductivity profile to lead to the improvement of energy confinement time, and high RF power with a spectrum of low phase velocity yields the large reduction of $l_i$.[6-3] The RF power dependence on $l_i$ mentioned above is also deduced on the PLT experiment.[6-4] Lower hybrid current drive can therefore be the most promising method for the active control of $j(r)$ . In this chapter, temporal evolution of $l_i$ is investigated for the LH-wave injected plasmas in order to evaluate the parameter dependence of the modification efficiency of $j(r)$ , concerning the refractive index along the magnetic field $N_{//}$, $\Delta N_{//}$ (FWHM of $N_{//}$), directivity $\eta_d$, $P_{LH}$, effective ionic charge $Z_{eff}$, Te, and $n_e$ on the JT-60 tokamak for the optimization of confinement properties.

## 6.2 EXPERIMENT

Temporal evolution of $l_i$ was evaluated by the Faraday rotation angle measurement combined with MHD equilibrium calculations, which provides continuous data throughout the entire plasma discharge. Analysis procedure of the plasma internal inductance, poloidal beta, and the energy confinement time is described in chapter 5.

Active modification of the current density profile was investigated for divertor configuration plasmas with the parameters: $\bar{n}_e = 0.2 \sim 0.5 \times 10^{19}$ m$^{-3}$, minor radius $a \leq 0.92$ m, and major radius $R = 3.1$ m with CD- and H-unit.[5-14] The frequency of LH wave is 2.0 GHz. When the lower hybrid wave is injected with the CD-unit, the value of $l_i$ gradually decreases at the rate of -0.12 s$^{-1}$ to pronounce the significant flattening of the current density profile as indicated in Fig. 6-1. Here, $P_{LH} = 1.1$ MW, $\Delta\varphi$ (phase difference between the toroidally neighboring launchers) = 90° to yield the value of $\overline{N_{//}}$ and $\Delta N_{//}$ to be 1.7 and 1.0,

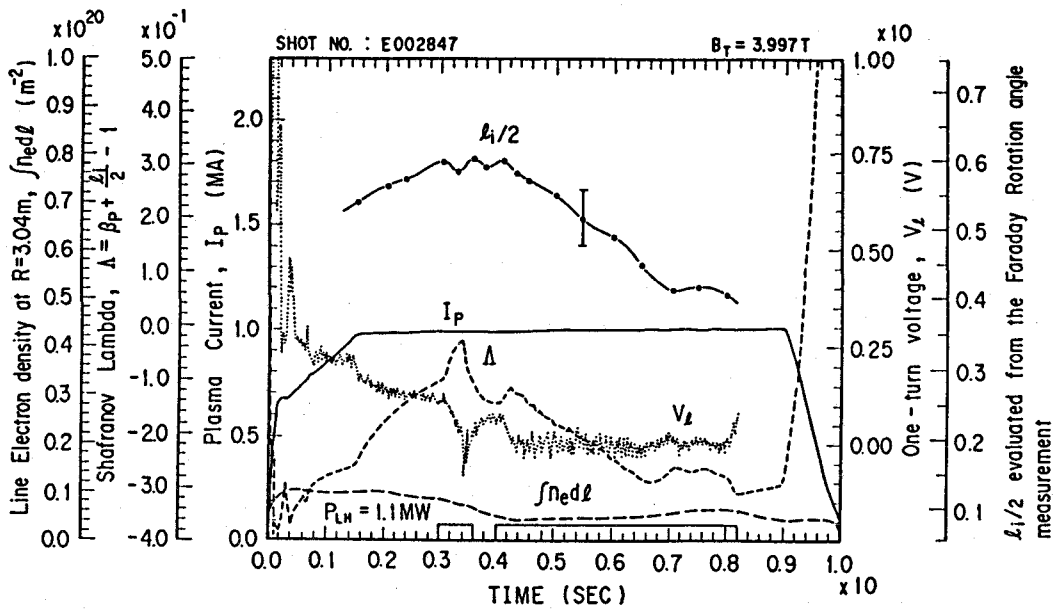


Fig. 6-1 The temporal evolution of plasma internal inductance $l_i$ for a lower hybrid current drive applied plasma, shown with the plasma current, one-turn voltage, Shafranov lambda, and line electron density at R = 3.04 m chord.

respectively, $\bar{n}_e$ = 0.3 x $10^{19}$ $m^{-3}$, $B_T$ = 4.0 T, and $I_p$ = 1.0 MA. The inductive plasma current is replaced by a RF current during the LH pulse as seen by the negative value of the loop voltage $V_l$. Here, the plasma current is feedback controlled to hold the constant value. The inductive correction to the loop voltage has been calculated by applying the reduction rate of $l_i$. From Poynting's theorem,

$$I_p V_l = I_p^2 R_p + \frac{d}{dt}\left(\frac{1}{2} L_i I_p^2\right), \tag{6.1}$$

where $R_p$ and is the plasma resistance, and $L_i = \mu_o R l_i/2$. Therefore, loop voltage is written as

$$V_l = I_p R_p + \frac{1}{I_p}\frac{d}{dt}\left(\frac{1}{2} L_i I_p^2\right)$$

$$= I_p R_p + \frac{1}{2} I_p \frac{dL_i}{dt} + L_i \frac{dI_p}{dt}. \tag{6.2}$$

During the flat top of the plasma current, the inductive correction to the loop voltage is given by

$$V_i = \frac{1}{2} I_p \frac{dL_i}{dt} = \frac{1}{2} I_p \mu_o \frac{R}{2} \frac{dl_i}{dt} .$$
$$= - 0.12 \text{ V.} \qquad (6.3)$$

The result of calculation shows that the ohmic plasma current is still carrried during the LH pulse to produce the resistive voltage of 0.1 V. The gradual decrease of Shafranov lambda is therefore identified as a decrease of $l_i$, and the decreased amount of $\Lambda$ for LHCD applied plasmas is approximately equal to that of $l_i/2$.

The initial augmentation of the Shafranov lambda at the beginning of the RF-pulse, which is not seen in the $l_i$ evolution trace, is deduced to be mainly caused by the build-up of a high energy parallel component of the electron pressure. When double RF pulses are injected, in particular as seen in Fig. 6-1, the initial short pulse produces a very large increase in Shafranov lambda. The result of the 3 rd harmonic measurement of the ECE, which estimates the amount of suprathermal electrons produced,[6-5] well explains the behavior of $\Lambda$ at the onset of the RF pulse qualitatively. The estimated ratio of suprathermal electron density to the thermal density was around 5 % to yield $\Delta\beta_p = 0.06$, which is nearly equal to the increased amount of $\Lambda$. Precise evaluation of the suprathermal electron density, however, calls for the direct measurement of electron velocity distribution function. On the other hand, the initial shrink of the peripheral plasma current, however, can possibly contribute to the increase of $l_i$, which is insensitive in the present diagnostic layout.[6-6] The analysis of $\beta_p{}^{//}$ from the Faraday rotation angle measurement combined with the diamagnetic measurement has implied that the value of $\beta_p{}^{//}$ is approximately kept constant during the RF pulse excluding the case when a minor disruption has occurred, which is consistent with the results of ECE diagnostics.

The modified amount of $l_i$ during LHCD is plotted in Fig. 6-2 as a function of the RF power divided by the electron density. Since it takes around 3 to 4 s for the modification of *j(r)* to reach a steady state, the data points are plotted as differences of $l_i$ evaluated before the RF pulse and the steady state. LH wave was excited by the CD-unit with $\Delta\varphi = 90°$. Here, the lowest RF power and the electron density of the plotted data points are 0.5 MW and 0.25 x $10^{19}$ $m^{-3}$, respectively. Therefore, the results in the region $P_{LH}/\overline{n_e} < 2 \times 10^{19}$ MW/$m^{-3}$ show only the electron density dependence. It can be seen from the figure that the high RF power and the low electron density realizes a broad current density profile. The reduced amount of $l_i$ is approximately proportional to $P_{LH}/\overline{n_e}$. In the relatively high density region ($\overline{n_e} > 1 \times 10^{19}$ $m^{-3}$), increase of $l_i$ is observed to result

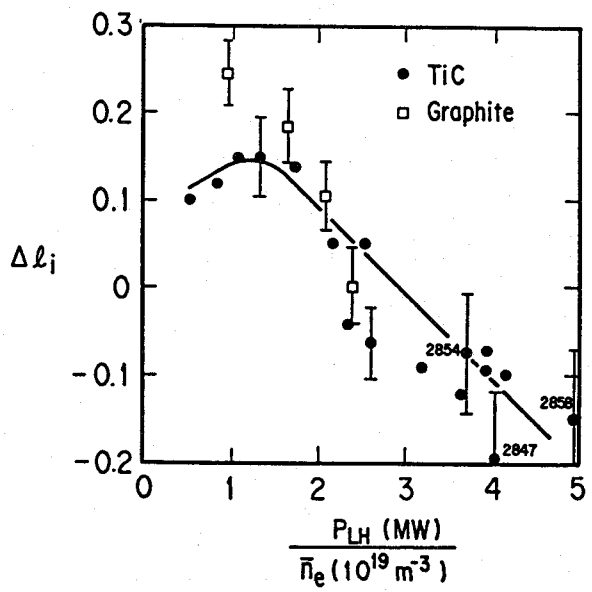


Fig. 6-2 Modified amount of plasma internal inductance $l_i$ during the lower hybrid current drive as a function of the injected RF power divided by electron density. Closed circles are the data points for the TiC-coated molybdenum first wall, and open circles are for the graphite first wall.

in the electron heating. Open squares and closed circles in the figure are the data points obtained for the first wall material of TiC-coated molybdenum and graphite, respectively of which Zeff range in 1.0 ~ 1.5 and 2.5 ~ 3.0 for the electron density above 1 x $10^{19}$ $m^{-3}$. In the range $P_{LH}/\bar{n}_e < 1.5 \times 10^{19}$ MW/$m^{-3}$, higher the value of $Z_{eff}$ is, more effectively the radiation cooling at the edge plasma region occurs to yield the peaked current density profile and thereby the higher value of $l_i$. On another matter, high $Z_{eff}$ values degrade the current drive efficiency $\eta_{cd}$ as pointed out by Fisch.[6-7] In the low density region, on the other hand, the value of $Z_{eff}$ becomes large, and the it can not be distinguished between the cases with TiC and graphite walls. Therefore the effect of $Z_{eff}$ on the modified amount of $l_i$ becomes no more observable.

The averaged modification rate of $l_i$ over the RF pulse for the CD- and H-unit is depicted in Fig. 6-3 as a function of the product of $N_{//}$ and $\eta_d$. Averaging is to neglect the effect of intermittent injection of impurity atoms, which has been observed to effect on the modification of *j(r)* . $N_{//}$ spectrum density $P(N_{//})$ of the CD- and H-unit calculated from the Brambilla theory[6-8] is shown in Fig. 6-4. Since $N_{//}$ and $\eta_d$ behave antagonistically in accordance with the $\Delta\varphi$ adjustment as documented in the figure, the product of $N_{//}$ and $\eta_d$ would be the appropriate measure of the modification efficiency. Here, directivity $\eta_d$ is defined as

$$\eta_d = \frac{\int_0^{+\infty} P(N_{//})\, dN_{//}}{\int_{-\infty}^{+\infty} P(N_{//})\, dN_{//}} . \qquad (6.4)$$

The injected RF power is 1 MW, and the electron density of the target plasma is around 0.3 x $10^{19}$ $m^{-3}$. As for the case when LH wave is excited by the CD-unit, which has higher value of $N_{//}$ and $\eta_d$, a large reduction of $l_i$ can be

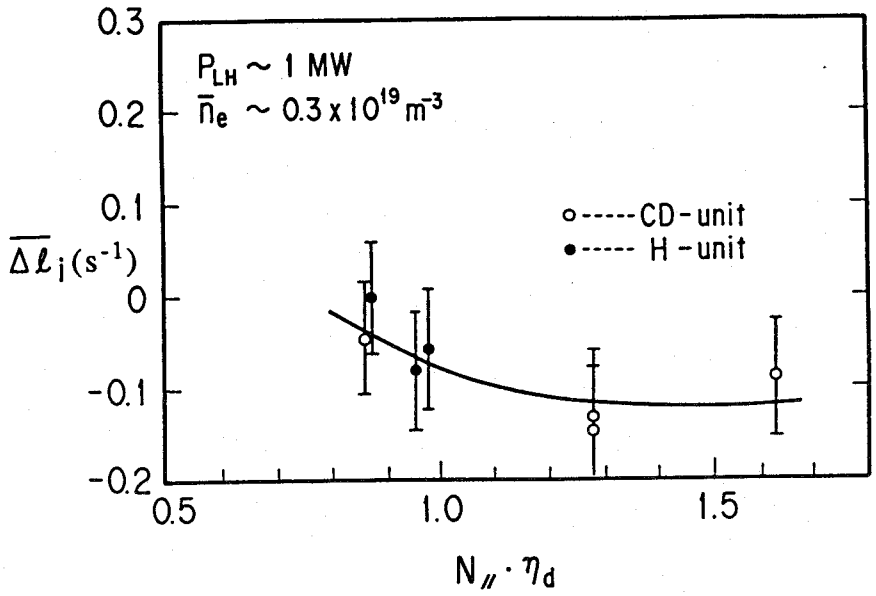


Fig. 6-3 Averaged reduction rate of plasma internal inductance $l_i$ shown as a function of the product of the refractive index along the magnetic field and the directivity. Open squares are the results obtained with a current drive launcher, and closed circles are for a heating launcher.

expected. The amount of reduction, however, soon saturates as documented in Fig. 6-3. The counter-current drive with the CD-unit against the inductive current, on the contrary, does not affect the value of $l_i$ for $P_{LH}$ and $\bar{n}_e$ in the range of 1 MA and around 0.3 x $10^{19}$ m$^{-3}$, respectively. The application of the H-unit, which has lower directivity and narrower $N_{//}$ spectrum width ($\Delta N_{//} = 0.5$) than CD-unit, can also realize the reduction of $l_i$. Although the experimental results are within the error bars, the amount of modification, however, is shown to be smaller than CD-unit. It is due to narrower $\Delta N_{//}$, even if the value of $\overline{N_{//}} \cdot \eta_d$ is set equal to the CD-unit. Therefore, larger RF power is required in order to improve the reduction efficiency of $l_i$ with the H-unit. It has also been found that the current drive efficiency $\eta_{cd}$ is inferior ccompared with the CD-unit. The

experimental result indicates that larger value of $\overline{N_{//}}$ and $\eta_d$ as well as the appropriate selection of $\Delta N_{//}$ concerning the accessibility condition effectively flattens the current density profile.

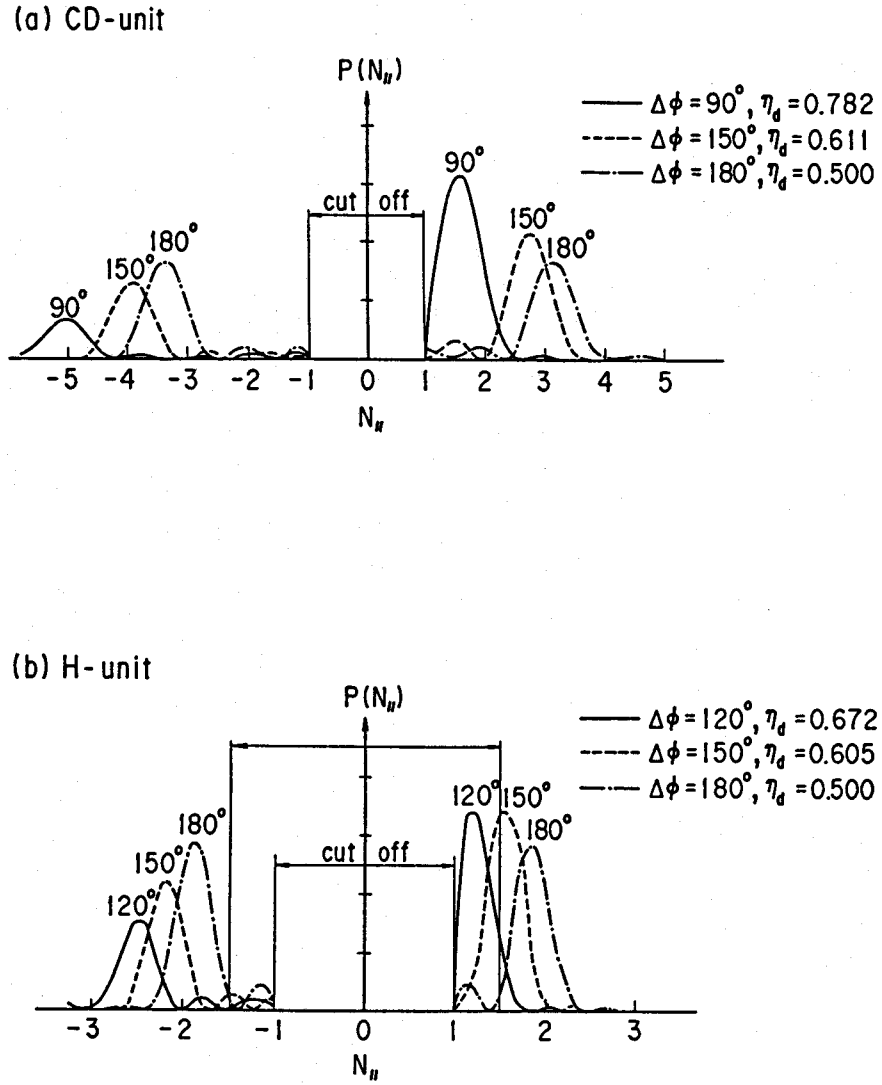


Fig. 6-4 Spectra of the refractive index parallel to the magnetic field for the CD- and H-unit calculated from the Brambilla theory.

The correlation between the change of the internal inductance $\Delta l_i/2$ evaluated from the Faraday rotation angle measurement and Shafranov lambda for the LHCD applied plasmas is shown in Fig. 5-4 together with the case when neutral beam heating is applied and neutral beam heating is superimposed with the LH wave. The data points are plotted for the maximum modified amount attained in a discharge. Even though the value of $l_i$ is effectively reduced, the value of $\Lambda$ decreases at the same amount. Therefore the improvement of $\beta_p$ stays within the error bars of the measurement, although the sawtooth activity has diminished. The flattening of the current density profile does improve the confinement properties, however, the increase of the energy confinement time is around 10% so far as the present experiment indicates.

When the NB heating is applied on the plasma of which current density profile is effectively flattened, significant increase of the energy confinement time was observed. The incremental energy confinement time is 110 ms, to yield the global energy confinement time which is approximately equal to that of ohmic discharges in accordance with the plasma current.[6-9] The additional reduction of $l_i$ by the superposition of the NB heating is 0.1. This reduction is realized by the improvement of $\eta_{cd}$ ( = $R\bar{n}_e I_{RF}/P_{LH}$, scales well with $6 <T_e>/(5 + Z_{eff})$[6-10]) due to the increase of the electron temperature, because the reduced amount of $l_i$ with NB heating alone is less than 0.03. Since the value of $l_i$ is already decreased by the amount of 0.2 before the superposision of NB heating, it is deduced that the additional decrease of 0.1 is not the sole reason to induce the measured tenfold improvement of the incremental energy confinement time compared to NB heating alone. In another word, flattening of *j(r)* alone does not contribute much to the improvement of energy confinement time. Unless the substantial non-linear relationship between the value of $l_i$ and the incremental

energy confinement time exists, another mechanism should interpose in this process.

One of the approaches to elucidate the mechanism for the improvement of confinement properties lies in the investigation of a roll of electron temperature. Electron temperature profile measured by the Thomson scattering system is shown in Fig. 6-5 for the ohmic, LHCD applied, and LHCD + NB heated plasmas. The peaked electron temperature profile during LHCD unequivocally demonstrates that $j(r)$ is decoupled from the temperature profile, that is, classical conductivity is no longer

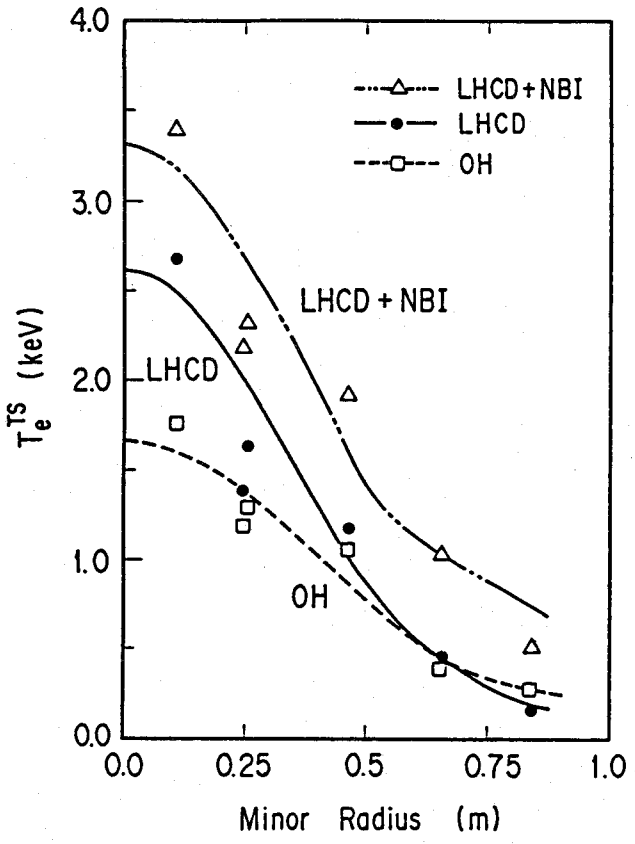


Fig. 6-5 Electron temperature profile measured by Thomson scattering for the ohmic, LHCD applied, and LHCD + NB heated plasmas.

instrumental in governing the current distribution. Therefore the electron temperature profile can behave independently from $j(r)$ , and it can occasionally take a synergetic role for the improvement of confinement. As for the case when NB heating is superimposed on the LHCD plasma, electron temperature profile exhibits a slight dilation at the edge plasma region, compared with the profile when LHCD is solely applied. The increase of electron stored energy in the plasma indicates the improvement of the energy confinement time.

## 6.3 DISCUSSION

The now-documented parameter dependence of LHCD for the effective modification of the current density profile has demonstrated the possibility of further improvement of the energy confinement time for large tokamaks. It was proclaimed that the flattening of the current density profile accompanied by the peaked electron temperature profile can realize the substantial improvement of the energy confinement time. Flattening of the current density profile alone seemingly does not contribute much to the improvement of the energy confinement time, since the electron temperature profile shapes for the LHCD plasma and LHCD + NB heated plasma are very similar except for the outer region of the plasma. The increase of the low density edge electron temperature in the LHCD + NB heating case may have possibly coupled to the LH-wave to result in the improvement of confinement properties. One of the possible mechanisms is the centrifugal drift of resonant electrons[6-11] induced by the electric field, which is produced by the momentum transfer from the traveling RF wave to electrons, and the poloidal magnetic field. The assumption that the ohmic plasma confinement mechanism originates in the pinch effect induced by the plasma current and the poloidal magnetic field makes this interpretation intelligible. The increase of electron temperature in the edge plasma region, where the accessibility condition is favorable for the penetration of LH wave, can enhance this effect.

## REFERENCES TO CHAPTER 6


6-1 F. X. Söldner et al., Phys. Rev. Lett. **57**, 1137(1986).

6-2 F. X. Söldner et al., Proceedings of the 7 th APS Topical Conference on Applications of Radio Frequency Power to plasmas, Kissimmee, 1987.

6-3 K. McCormick et al., Phys. Rev. Lett. **58**, 491(1987).

6-4 R. Motley (private communication).

6-5 D. Winske, T. H. Peter, and D. A. Boyd, Phys. Fluids **26**,3497(1983).

6-6 K. Ushigusa et al., JAERI-M 87-012(1987).

6-7 N. J. Fisch, Phys. Rev. Lett. 41, 873(1978).

6-8 M. Brambilla, Nucl. Fusion **16**,47(1976).

6-9 JT-60 Team, Proceedings of the 11 th International Conference on Plasma Physics and Controlled Nuclear Fusion Research, Kyoto,1988(International Atomic Energy Agency, Vienna, Austria, 1987), Vol. 1, p. 563.

6-10 K. Ushigusa et al., Proceedings of the 12 th International Conference on Plasma Physics and Controlled Nuclear Fusion Research, Nice, (International Atomic Energy Agency, Vienna, Austria, 1988), (to be published).

6-11 K. Uehara, JAERI-M 87-180(1988).

# CHAPTER 7. CONCLUSION

Development of the multi-wavelength JT-60 polari-interferometer system has been successfully undertaken, and its feasibility was addressed in this thesis work, pronouncing the establishment of a design basis of large tokamak interferometers. The developed system routinely provides high-resolution electron density and informations on the evolution of current density profiles. Evaluation schemes of the obtained data, for the interpretation to physics quantities, have also been devised to extend the developed system to a *complete plasma diagnostic device.* Further extension of polarimetric measurements to the evaluation of confinement properties, in terms of the incremental energy confinement time, has addressed its effectiveness, introducing an alternative approach to the Faraday rotation measurements. In addition, a concept of *"active diagnostics"* have been proposed, which enables the control of plasma parameters. Based on this concept, the first real-time feedback control of electron density and the active modification of current density profiles have been successfully carried out.

## 7. 1. DEVELOPMENT OF FAR-INFRARED POLARI-INTERFEROMETER ON JT-60

Required research items for the development of a polari-interferometer system feasible enough for JT-60 applications have been surveyed. Imposed requirements and the result of developments are as follows:

(1) High frequency stability and mode purity of a source laser are essential to obtain an adequate fringe resolution, since the difference of the optical path length between the probing and reference branch is 40 m and the total propagation distance exceeds 130 m for JT-60. The newly developed cw 118.8-μm $CH_3OH$ twin laser system,

which employs germanium etalon as a beam coupler for the homogeneous pumping of the laser media and optical layout to eliminate the back talk of pump $CO_2$ laser beam, has demonstrated its effectiveness to yield a single-mode oscillation. The germanium etalon has also improved the power conversion efficiency up to 0.088%. It was shown that *Absolute* frequency stabilization schemes, such as the application of Lamb dip profiles on a fluorescence line or an absorption cell, are not required so far as to achieve the frequency stability $\Delta f/f$ of $1 \times 10^{-8}$ which is equivalent to the fringe resolution of 1/400. The *relative* frequency stabilization by the simple and reliable mechanical cavity-length modulation technique combined with a sequential feedback control has proved its engineering feasibility on JT-60.

(2) Concave lens effect of density gradient causes a significant phase difference inside the propagating beam volume after penetrating through a plasma for large tokamak applications. In order to cope with the distortion of the wave front, the most appropriate interferometer configuration and the effective beam diameter were evaluated. It was shown that Michelson configuration with corner-cube reflectors combined with the aperture of 22 mm$\phi$ diameter is effective for the 1/100 fringe resolution.

(3) Owing to the stabilization of the propagating beam axis by the newly developed flexible light-guide and preservation of visibility with the adaption of the corner-cube configuration also on the reference branch, diminution of the signal detection level due to the mechanical vibration was not observed even for the severe plasma disruptions.

The experimental evaluation of the attenuation index of the 118.8-$\mu$m coherent radiation in the humid air yielded appropriate dehydrating parameters to suppress the transmission loss below 1 dB (excluding the absorption loss at vacuum windows) for the total propagating distance of 130 m. The obtained attenuation index was less than half of

the value previously reported, which has been measured employing spectroscopically separated light as a source. Therefore the value claimed in this work can be assumed to be the first reliable data obtained using a single-mode coherent source.

(4) Furthermore, development of optical components for the polarimetric measurement and the optimum laser power distribution were pronounced to be indispensable for large tokamak interferometry. Étalon technique have been newly applied on beam splitters, polarization separators, and vacuum windows. The developed components including the repetitively bakable modified Helico-flex vacuum sealing proved their effectiveness and reliability under the huge stray magnetic field and mechanical vibrations on JT-60.

(5) The introduced method for the edge plasma density measurement in principle preserves the boundary conditions of the interacting edge plasma with the first wall, and it is encouraging for the future fusion experiment devices, of which diagnostic accessibility is severely limited. The installation of a millimeter wave circuit inside the JT-60 vacuum vessel literally enables as many diagnostic chords as required, and it has proved its engineering feasibility, yielding precious informations as to the plasma surface interactions and edge plasma localized phenomena.

(6) The whole interferometer system has been routinely in operation reliably for two years without any readjustment or attendant complications. So far, the JT-60 interferometer system has experienced only secular damages of a signal processing IC and $CO_2$ gas feeding tubes, which were replaced promptly. The operation status is remotely controlled and monitored. Timing signal and the programmed communication network with the JT-60 central control system supervise the whole interferometer system. Therefore, the basis of unmanned operation has been established.

## 7. 2. APPLICATION OF THE DEVELOPED FAR-INFRARED POLARI-INTERFEROMETER ON JT-60 EXPERIMENTS : EVALUATION OF CURRENT DENSITY PROFILES AND CONFINEMENT PROPERTIES

The developed polari-interferometer system has been applied on various JT-60 plasmas with following physics interpretation and active diagnostic methods:

(i) The real-time feedback control of electron density on a tokamak plasma has been achieved for the first time. Successful application of this method supported the stable plasma current rise and enlarged the physics operation regime, especially for the additional heating.

(ii) The first interferometric measurement of the divertor plasma was successfully undertaken on JT-60. Informations on the bilateral relationship between plasmas in the main plasma region and in the divertor region is necessary to understand the divertor functions and particle transport mechanism. Measurements have been enabled by the application of the corner-cube reflector configuration with the quadruplicated laser beam path for the stabilization of the propagating laser beam axis. Stability of the vibration compensating He-Ne laser beam is essential, when a reflector is installed inside the vacuum vessel. Molybdenum metallic reflectors have been chosen to cope with the erosion and sputtering by the heat flux and the particle bombardment from the plasma. The enlargement of the He-Ne laser beam diameter and the choice of large APD detector contributed much for the stability of the detection level against the huge amplitude external vibrations. The amount of phase shift caused by the external vibration is more than twenty times larger than the phase shift experienced by the plasma.

From the result of divertor plasma density measurements, combined with the density profile in the main plasma region, it has been found that particle flow along the magnetic field in the edge plasma region takes the dominant role on the density clamping of neutral beam heated plasmas. A simulation code has been devised, which employs a tokamak transport code combined with a divertor fluid model, to deduce the transport parameters in the bulk plasma. Application of this simulation analysis has corroborated the result of experiment that the divertor plasma density has non-linear dependence on the bulk plasma density. Accordingly, a measure of physics operation scheme to realize a cold dense divertor plasma for the effective divertor performance has been established.

(iii) As to the derivation of electron density profiles, an inversion method, which is based on MHD equilibrium calculations, has been newly introduced. It expands the 5 ch line density data on magnetic flux surfaces determined via polarimetry. This scheme includes the Shafranov shift of the magnetic axis and a flexible boundary conditions. Although the profile shape is assumed to have a simple parametric form, agreement with the Thomson scattering measurement was confirmed to be within 10%.

(iv) Further extension of the interferometric technique to the evaluation of current density profiles $j(r)$ by the Faraday rotation angle measurement has been pursued. Averaged poloidal magnetic field $\overline{B_z}$ is useful to inform of a temporal evolution of the relative amount of integrated current density in the area between the magnetic axis and diagnostic chord prepared at half the minor radius outside of the plasma center. Although the value of $\overline{B_z}$ is dependent on the electron density profile and the position of the magnetic axis, it is effective for the simplified evaluation during the plasma pulse interval.

In order to invert the line averaged Faraday rotation angle to the local magnetic field and thereby the current

density profile, an MHD equilibrium calculation code has been developed. The value of the plasma internal inductance $l_i$ and the energy confinement time have been also evaluated by the application of this code. The newly developed method experimentally separates the value of $l_i$ from Shafranov lambda, and it requires neither the full electron and ion temperature nor density profile for the evaluation of the energy confinement time. Furthermore, it is more accurate, because the obtained value of poloidal beta includes both the parallel and the perpendicular components to the magnetic field line. The diamagnetic measurement persuasively used for the evaluation of energy confinement time, on the other hand, does not consider the parallel component, which introduces considerable error, when a high energy component of the electron pressure parallel to the magnetic field line was induced. Therefore, by combining the value of poloidal beta $\beta_p^{eq.}$ evaluated from the Faraday rotation angle measurement and the perpendicular component of the poloidal beta $\beta_p^{\perp}$ from the diamagnetic measurement, parallel component of the poloidal beta $\beta_p^{//}$ has been also estimated.

Due to the intrinsic restrictions of having only one diagnostic chord, the resolution of the safety factor q on the magnetic axis is severely limited, and it requires more localized informations of $j(r)$ to understand the relationship between $j(r)$ and MHD activities. In addition, a symmetric plasma configuration with respect to the toroidal midplane is supposed, and the assumption that equi-density surface coincides the magnetic flux surface has been made in the evaluation procedure, which is applicable only for low beta plasmas. Therefore, the agreement of electron density profile obtained by the application of the equilibrium calculation to that measured by the Thomson scattering measurement has been examined beforehand, which was usually the case. The developed physical interpretation method, however, pronounces its effectiveness, and it has brought precious informations on the value of the incremental energy confinement time for the additionally

heated plasmas, introducing an alternative approach to the analysis of the Faraday rotation angle measurement.

The possibility of active modification of the current density distribution and the bilateral relationship between the profile shape and the energy confinement time has been investigated with LH-wave on JT-60 for the optimization of confinement properties. Based on the intensive parameter survey, it has been found that the current density distribution can be modified as a function of $P_{LH}/\overline{n_e}$, $\overline{N_{//}} \cdot \eta_d$, $\Delta N_{//}$, $T_e$, and $Z_{eff}$. Appropriate adjustment of this parameter set can realize a substantial flattening of the current density profile, decoupling from the classical conductivity profile.

As to the optimization of confinement properties, the experimental result implies that flattened current density profile accompanied by the enhancement of edge electron temperature is necessary, which otherwise could not have been clarified without the diagnostics described in this work. Although the mechanism of the improvement of energy confinement calls for detailed investigation, the newly developed scheme promises further improvement of the confinement properties.

## ACKNOWLEDGMENTS

The author sincerely appreciates the supervision of the professor of Osaka university Dr. S. Goto who has implanted him the ideas of interferometric plasma diagnostics and physics application of Faraday rotation angle measurements. He also wishes to express his gratitude to professors Dr. S. Minami, Dr. Y. Ichioka and Dr. T. Ishimura for directing this thesis work.

The author wishes to acknowledge Drs. H. Soltwisch, E. Graffmann of IPP/KFA Jülich, Drs. K. McCormick, F. X. Söldner of IPP/MPI Garching, Drs. H. K. Park, J. Stevens, D. Mansfield of PPPL, Dr. Ma of ORNL, and Dr. A. Costley of JET Joint Undertaking, Culham for the precious discussions. The author appreciates Drs. H. Takeuchi, H. Yokomizo, S. Konoshima, and T. Matoba of the diagnostic division for their enlightening discussions. He also wishes to express his gratitude to professors of Nagoya university Dr. J. Fujita and Dr. S. Tsukishima. This work has been done as a part of the JT-60 project with the collaboration and support of the JT-60 Team. The co-operation and help of the staffs of the diagnostic division and all the members of JT-60 Team is acknowledged. The author is indebted to the JT-60 directors Dr. M. Funahashi, Dr. Y. Suzuki, Dr. S. Tamura, and Dr. M. Yoshikawa for their continuous support and encouragement.